Co-funded by the

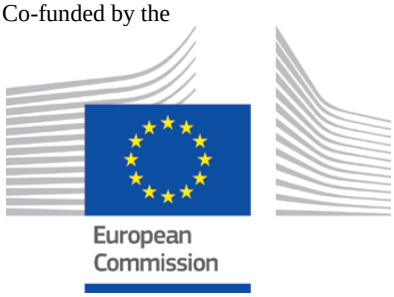

CEBAMA

➢ (Contract Number: 662147)

Deliverable n° D3.05

Preliminary results and interpretation of the modelling of WP1 & WP2 experiments.

Editors: Andrés Idiart (Amphos 21)

Date of issue of this report: 30.11.2017

Report number of pages: 70

Start date of project: 01/06/2015 Duration: 48 Months

Project co-funded by the European Commission under the Euratom Research and Training Programme on Nuclear Energy within the Horizon 2020 Framework Programme		
Dissemination Level		
PU	Public	X
PP	Restricted to other programme participants (including the Commission Services)	
RE	Restricted to a group specified by the partners of the CEBAMA project	
CO	Confidential, only for partners of the CEBAMA project	

ABSTRACT

The present deliverable D3.05 contains a description of modelling approaches and recent progress by WP3 partners on the simulation of WP1 and WP2 experiments. Each partner contribution below summarizes the modelling work so far and presents the most recent results obtained, with application to WP1/WP2 experiments.

1 KIT/ V. Montoya, N. Ait Mouheb, T. Schäfer

Abstract

WP 3 is partly devoted to the modelling and interpretation of experimental data generated within the CEBAMA project (WP1 and WP2). In particular, KIT-INE is mainly performing reactive transport simulations of a fully saturated isothermal (298 K) problem representing the laboratory through-diffusion experiment of the tracers HTO, $^{36}Cl^-$, $^{129}I^-$ and Be(II) in the interface low pH cement / MX-80 bentonite system (see Figure 1.1). Additionally, porosity changes due to dissolution/precipitation reactions with feedback on transport properties are also studied.

1.1 INTRODUCTION

A schematic representation of the diffusion experiments is presented in Fig. 1. Diffusion of the selected tracers occurs across the interface between bentonite porewater and the low-pH cement (50% CEM I 52.5N + 50 % silica fume) manufactured by KIT-INE in WP1 (Ait Mouheb et al., 2017). The cylindrical low pH cement has a diameter and thickness of 30 and 10 mm, respectively, and it is surrounded by 2 reservoirs of 30 ml: the upstream and downstream reservoirs, containing bentonite and low pH cement porewater, respectively.

The reactive transport simulations will be compared to the mentioned through diffusion experiments performed in WP1, but at this period of the project, the information is still not available. However, a big effort has been done in both, WP1 and WP2, to obtain the required input parameters for the reactive transport model. Among others the main input parameters that can be obtained from WP1 and WP2 are the pH cement mineralogy, porewater composition, porosity, diffusivity and the aqueous speciation of Be (see Figure 1.2). A big part of the chemical and physical characterization of the cement paste is already documented in Ait Mouheb et al., (2017) and Gaona et al. (2017) and will continue during next year.

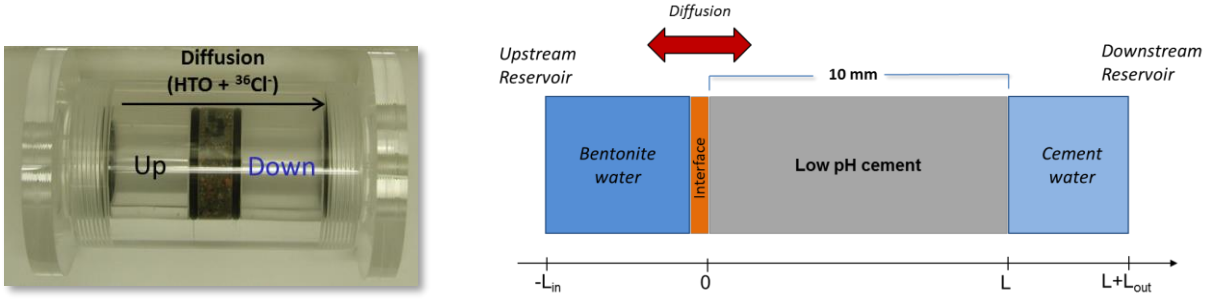

Figure 1.1. *Cell used in the laboratory through diffusion experiments (left) and the schematic representation of the experiments (right).*

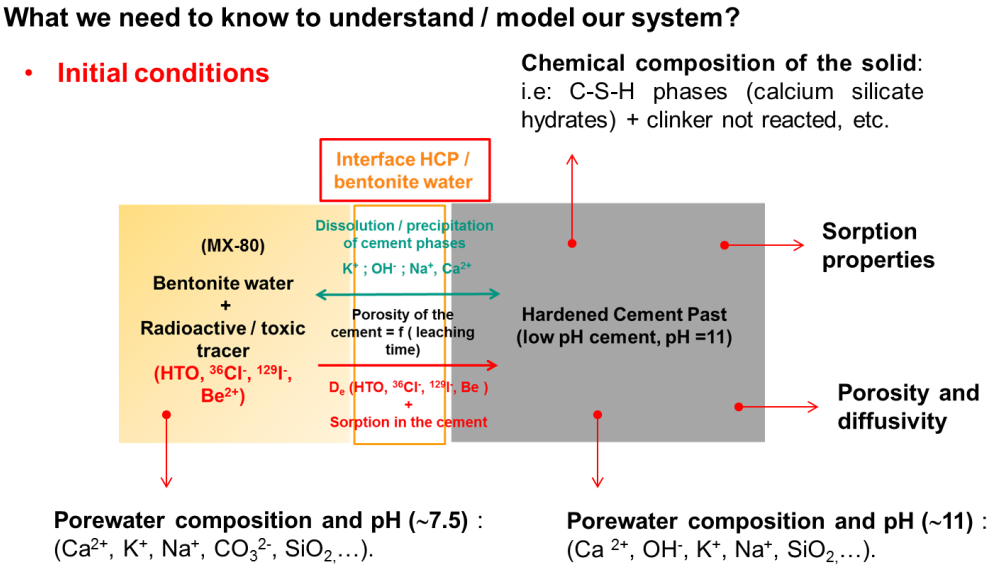

Figure 1.2. *Input parameters for modelling the studied system.*

1.2 IMPLEMENTATION OF THE MODEL

Geometry and time and space discretization

The system studied is implemented in the code PHREEQC v.3 (Parkhurst and Appelo, 2013) which can take into account geochemical and physical parameters variations due to mineralogical evolutions as a function of time. Geometrical and transport parameters including the discretization of the system (water and solid domains) have been initially implemented in 1D (see Figure 1.1). The studied periods correspond to 14 min, 5 and 30 days, although simulations will be extended to 6 months. The mesh size and the time steps have been selected to ensure a satisfactory compromise between computation time and sufficient spatial resolution of the expected geochemical and transport processes, especially at the interface between the bentonite porewater and the low pH cement hydrated phases. A constant concentration and closed boundary condition have been imposed on the extremities of the upstream and downstream reservoir, respectively in order to reproduce the boundary conditions imposed in the experiments.

1.3 CHEMICAL INPUT PARAMETERS

Mineralogy and porewater composition obtained from WP1:

The initial mineralogical composition of the hydrated cement phases considered is 93% wt. C-S-H phases with a Ca/Si ratio of 0.8 which is representative of a full hydrated low-pH cement (pH ~ 11.0) obtained after mixing 50% of sulphate resistant Portland cement (CEM I 52.5N SR) and 50 % of silica fume with de-ionised water using a water/binder ratio (w/b) = 0.6. The hydration model of the low pH cement is under progress at this moment and it will be compared with the pore water composition, total porosity and the mineralogy composition obtained experimentally in the future. The reactive transport model will then use the hydrated composition determined experimentally as initial input parameter.

Mineralogical composition of the hydrated phases (see Table 1.2) has been determined experimentally (Ait Mouheb et al. 2017) with a combination of different techniques (X-ray diffraction (XRD), thermogravimetric - differential thermal analysis (TG-DTA), ^{29}Si and ^{27}Al Magic angle spinning nuclear magnetic resonance (^{29}Si and ^{27}Al MAS NMR) and scanning electron Microscopy - energy dispersive X-ray spectroscopy (SEM-EDX). At this moment, it has not been

possible to experimentally identify the solid phase containing iron and for this reason in the model it is assumed that iron phases are in the form of Fe-ettringite. Additionally, no solid solutions, not Al uptake in C-S-H phases or Al-Fe bearing phases are considered but will be implemented in the future. Secondary minerals to be considered are also shown in Table 1.2.

The initial porewater composition of the low-pH cement is defined in equilibrium with the hydrated solid phases present in the system and compares well with the measured concentrations (see Table 1.1). The porewater composition of the clay is representative of the MX-80 bentonite described in the literature (Wersin et al. 2003) and has been synthetized and measured in the laboratory by Inductively coupled plasma mass spectrometry (ICP-MS) and inductively coupled plasma optical emission spectrometry (ICP-OES).

Table 1.1. *Initial pore water compositions. Narrows represent the gradient of concentration to the bentonite water (blue) or to the cement (red).*

	MX-80		Cement
pH	7.74	←	11.1
Ionic strength			
Solutes (mol/L)			
Na	0.31	→	5.70×10^{-3}
K	1.54×10^{-3}		7.50×10^{-3}
Ca	1.33×10^{-2}	←	6.70×10^{-3}
Cl	0.22	→	2.30×10^{-3}
SO_4	6.86×10^{-2}		1.12×10^{-2}
Si	1.80×10^{-4}	←	1.22×10^{-3}
Al	2.11×10^{-8}	←	1.10×10^{-7}
Fe	5.00×10^{-5}	→	7.70×10^{-8}
Mg	9.63×10^{-3}	→	2.70×10^{-6}
CO_3	9.20×10^{-4}	→	3.88×10^{-6}
$^{36}Cl^-$	**$4.55 \cdot 10^{-6}$**		-
$^{129}I^-$	$5.93 \cdot 10^{-5}$	→	-
HTO	$1.86 \cdot 10^{-9}$		-
Be	>1 $\cdot 10^{-8}$ **($Be(OH)_2(s)$)**		-

Thermodynamic database

Chemical reactions at equilibrium and kinetically controlled have been simulated using the thermodynamic database ThermoChimie (Giffaut et al. 2014) available in PHREEQC format (see Table 1.2). Debye-Hückel equation, valid for the ionic strength of the studied system (<0.3 M) is preferred to save computational time. ThermoChimie includes hydrates commonly encountered in Portland cement systems in the temperature range 0-100 °C. Rate equations of precipitation/dissolution of secondary/primary phases are provided directly in the input files of PHREEQC. Kinetic parameters for C-S-H phases and ettringite have been selected from Marty et al. (2015) and Baur et al. (2004).

Sorption properties

In the present status, sorption of the tracers in the cement matrix is not included in the model. Sorption reactions of $^{36}Cl^-$, $^{129}I^-$ and Be tracers into the low pH cement matrix will be considered as a thermodynamic mechanistic sorption model to be implemented in PHREEQC. Observations described in the recent review of Ochs et al. (2016) will be considered to select the most appropriate data, as well as data generated in the Cebama project, consisting of batch experiments of the studied radionuclides on the same solid materials (Ait Mouheb et al. 2017).

Table 1.2. *Initial mineralogical composition in the low-pH cement paste.*

Minerals	Mas fraction	Molar volume ($cm^3\ mol^{-1}$)	Formula	Volume fraction	Process
C-S-H (am)	0.93	59.29	$Ca_{0.8}SiO_{2.8}$ x1.54H_2O	0.65	Kinetics $k_n = f$ (pH)
Ettringite	0.07	710.32	$Ca_6Al_2(SO_4)_3(OH)_{12}$ x26H_2O	0.01	Kinetics
C-A-S-H	??	*(72.0 - 59.29)*	$Ca_{0.8}(Si,Al_{1-x})O_{2.8+z}$ x YH_2O	-	-
Calcite	-	36.93	$CaCO_3$	-	Equilibrium
$Fe(OH)_3$	-	-	$Fe(OH)_3$	-	-
Silica Fume	< 0.01	29.00	SiO_2	-	-
Portlandite	-	33.06	$Ca(OH)_2$	-	-
Porosity	-		-	0.34	-

1.4 PHYSICAL INPUT PARAMETERS

Porosity and diffusivity obtained from WP1:
Considering the very low permeability of cement (10^{-10}-10^{-14} m/s), mass transport will be considered diffusion-driven only, following Fick's law.

$$J = -D\frac{\partial C}{\partial x}$$

where J is the substance flux [kg/m^2·s]; $\frac{\partial C}{\partial x}$ is the concentration gradient [kg/m^4]; and D is the diffusion coefficient [m^2/s]. In the absence of any experimental data available, neither in the project nor in the literature, concerning the effective diffusion in low-pH cements, a value of 10^{-10} m^2/s was tentatively selected as an average pore diffusion coefficient for all the species. When this parameter will be available during 2018 by the through diffusion experiments of HTO performed by KIT-INE, the value will be updated in the model. The effective diffusion coefficient evolution is then related to the porosity change according to Archie's law assuming n = 1:

.

$$D = D_w(porosity)^n$$

Initial porosity of 35% has been determined experimentally by mercury intrusion porosimetry (MIP). Additionally, porosity changes due to mineral precipitation/dissolution and feedback on the effective diffusion coefficient are also taken into account in the model considering the molar volumes of the different solids formed or dissolved (see Table 1.2). Electrostatic surface interactions are not included, although they may influence the transport of the anionic tracers $^{36}Cl^-$, $^{129}I^-$ and $Be(OH)_3^-$ (Chagneau et al. 2015).

1.5 MODELLING RESULTS

The simulations were carried out for different time of interaction (14 min, 5 and 30 days) predicting that the low pH cement will be damaged in contact with the bentonite pore water, having a degraded area of ~ 2 mm after one month of alteration (see Figure 1.3). The alteration on the low pH cement is mainly due to the partial dissolution of C-S-H phases resulting in an increase of the porosity at few millimetres close to the interface bentonite/cement. (see Figure 1.4). The carbonation is linked to the precipitation of calcite and thus the decalcification of C-S-H phases (Jenni et al., 2014).

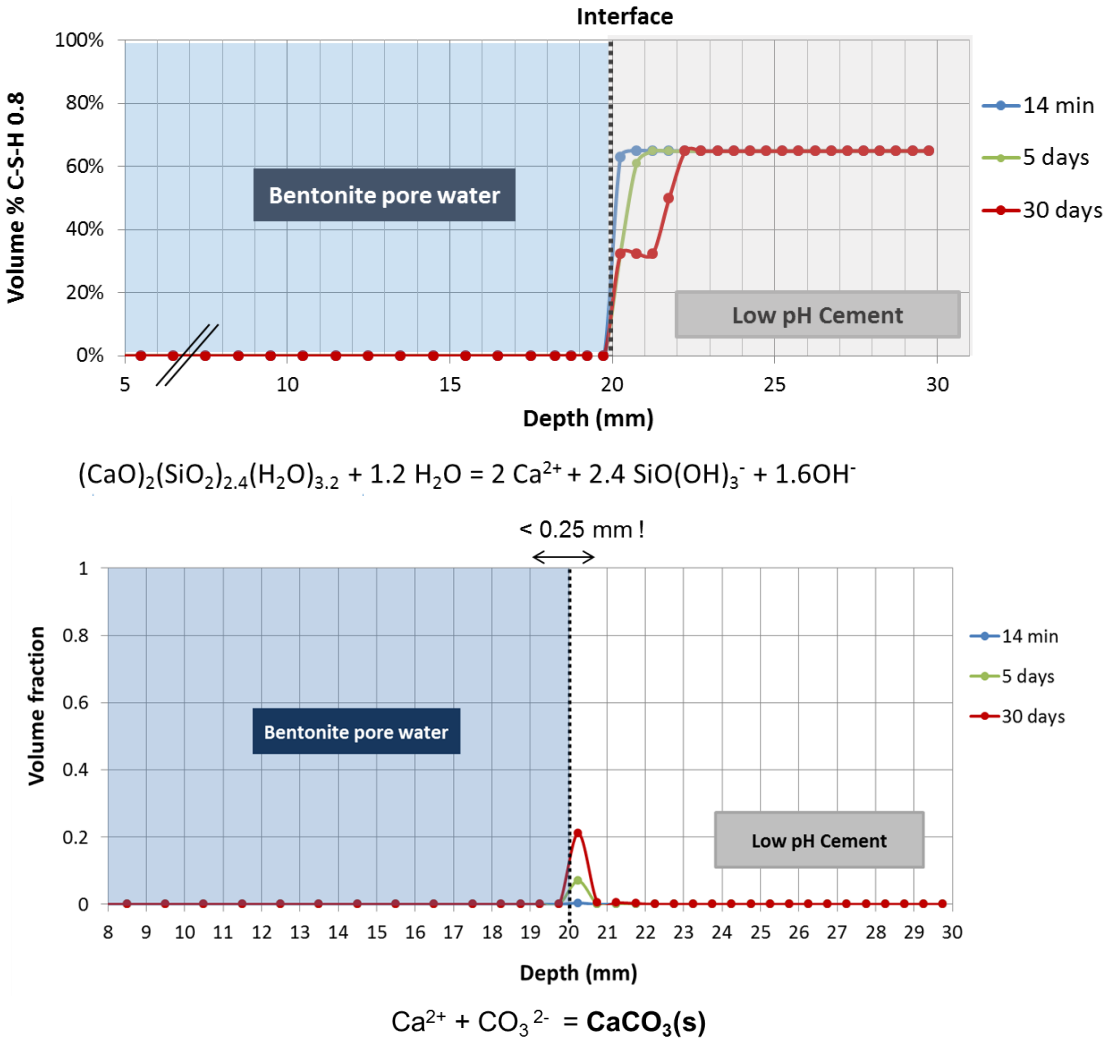

***Figure 1.3**. Simulation of the low pH cement alteration at different periods of time. The main process identified is the partial dissolution of C-S-H phases and carbonation.*

Magnesium enrichment in the decalcification area has been reported in the literature (Jenni et al., 2014; Dauzères et al. 2016). In our system, brucite is undersaturated and attempts to model the magnesium perturbation using available thermodynamic data suggested the formation of hydrotalcite. However, the recent determination of the solubility data for M-S-H phases will makes possible to account for the possible formation of M-S-H phases (Dauzères et al., 2016) and will be considered in the future. Finally, not attempts have been done to model the iron evolution, which will be done in the future when the iron speciation will be available from WP1.

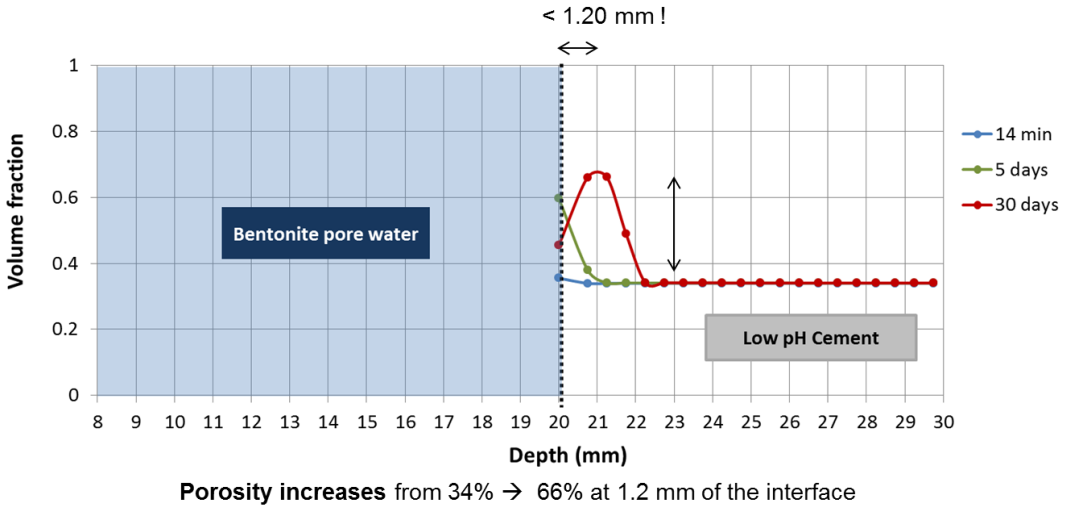

Figure 1.4*. Simulation of the low pH cement alteration at different periods of time. The main process identified is the partial dissolution of C-S-H phases resulting in an increase of the porosity at few millimetres close to the interface bentonite/cement.*

Finally, the diffusion of a not reactive and uncharged tracer (HTO) at initial concentration of 1.86 x10^{-9} M from the bentonite porewater to the low pH cement is presented in Figure 1.5. As can be seen the diffusion of HTO in the system will reach the steady state after 5 days of interaction.

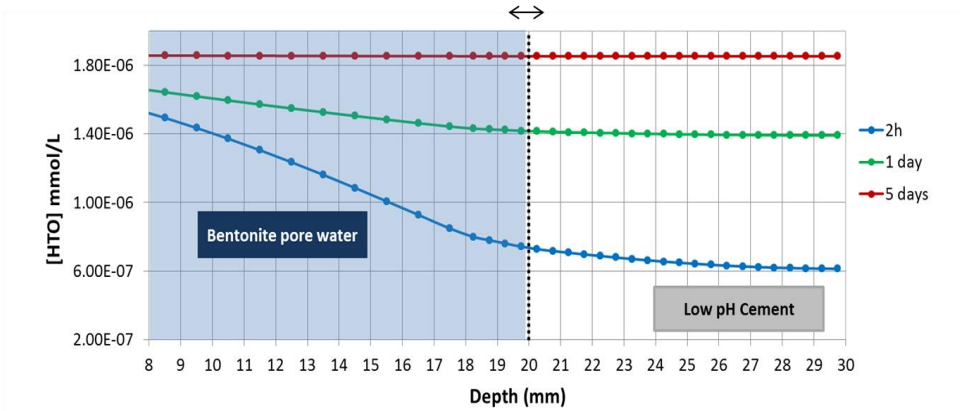

Figure 1.5*. Simulation of the HTO diffusion in the low pH cement / bentonite interface.*

1.6 CONCLUSIONS AND FUTURE WORK

We have developed and implemented a 1D model to simulate the interaction between a low pH cement and bentonite porewater in laboratory scale. The model considered a low-pH cement paste (pH ~ 11.0) synthesized in the CEBAMA project with a 93% wt. of the initial mineralogy being C-S-H phases with a Ca:Si ratio of 0.8. The simulations predict the formation of a degraded area in the cement phase of ~ 2 mm after one month of alteration. The alteration of the low-pH cement paste is mainly due to the partial kinetic dissolution of C-S-H phases resulting in an increase of the porosity. The carbonation of the cement is linked to the precipitation of calcite and thus the additional decalcification of the C-S-H phases.

The model will be improved including the iron and M-S-H solid phases in the system, the sorption properties of the cement to the selected radionuclides, aluminium and toxic elements and the diffusion coefficient in agreement with experimental data. The incorporation of Be diffusion in the model is link with the determination of an appropriate aqueous model for this element in WP2. Additionally, the model will be implemented in the iCp interface (Nardi et al. 2014) and compared with the results obtained with PHREQC.

1.7 REFERENCES

Ait Mouheb, N., Montoya, V., Schild, D., Soballa, E., Adam, C., Geyer, F. Schäfer, T. (2017). Characterization and sorption properties of low pH cements. 2nd Annual proceedings of CEBAMA project (in press).

Baur, I., Keller, P., Mavrocordatos, D., Wehrli, B., Johnson Ca.A. (2004). Dissolution-precipitation behaviour of ettringite, monosulfate, and calcium silicate hydrate. Cement and Concrete Research, 34, 341–348.

Chagneau, A., Tournassat, C., Steefel, C.I., Bour, I.C., Gaboreau, S., Esteve, I., Kupcik, T., Claret, F., Schäfer, T. (2015). Complete Restriction of 36Cl- Diffusion by Celestite Precipitation in Densely Compacted Illite. Env. Sci. & Tech. Letters, 2, 139–143.

Dauzeres, G. Achiedo, D. Nied, E. Bernard, S. Alahrache, B. Lothenbach (2016). Magnesium perturbation in low-pH concretes placed in clayey environment—solid characterizations and modelling. Cem. Concr. Res., 79 137–150.

Gaona, X., Böttle M., Rabung T., Altmaier M (2017). Solubility, hydrolysis and sorption of beryllium in cementitious systems. 1st Annual proceedings of the Cebama project KIT scientific report 7734.

Giffaut, E., Grivé, M., Blanc, P., Vieillard, P., Colàs, E., Gailhanou, H., Gaboreauc, S., Marty, N., Madé, B., Duro, L. (2014). Andra thermodynamic database for performance assessment: ThermoChimie. Applied Geochemistry, 49, 225–236.

Jenni, A., Mäder, U., Lerouge, C., Gaboreau, S., Schwyn, B (2014). In situ interaction between different concretes and Opalinus Clay, Phys. Chem. Earth A/B/C 70–71, 71–83.

Marty, N., Claret, F., Lassin, A., Tremosa, J. Blanc, P., Madé, B., Giffaut, E., Cochepin, B., Tournassat, C. (2015). A database of dissolution and precipitation rates for clay-rocks minerals. Applied Geochemistry, 55, 108-118.

Nardi, A., Idiart, A., Trinchero, P., de Vries, L.M., Molinero, J. (2014). Interface COMSOL-PHREEQC (iCP), an efficient numerical framework for the solution of coupled multiphysics and geochemistry. Computers & Geosciences, 69, 10-21.

Ochs, M., Mallants, D., Wang, L. (2016). Radionuclide and Metal Sorption on Cement and Concrete. Springer International Publishing Switzerland.

Parkhurst, D.L. and Appelo, C.A.J. (2013). Description of input and examples for PHREEQC Version 3 — A computer program for speciation, batch-reaction, one-dimensional transport, and inverse geochemical calculations. U.S. Geological Survey Techniques and Methods, book 6, chapter A43, 6-43A.

Wersin, P. (2003). Geochemical modelling of bentonite porewater in high-level waste repositories. Journal of Contaminant Hydrology, 61, 405-422.

2 AMPHOS 21/ A. Idiart

Abstract

This contribution deals with the modelling of the hydration of low-pH cement paste samples used in leaching experiments conducted by University of Sheffield (USFD). The modelling approach and preliminary results are presented and their implications for interpretation of the experiments are discussed. Hydration is modelled using a set of kinetic reactions for dissolution of the unhydrated minerals coupled to thermodynamic equilibrium calculations. The results of the evolution of hydration are presented and the implications for the leaching experiments are discussed.

2.1 INTRODUCTION AND OBJECTIVES

In WP1 of CEBAMA, an experimental benchmark low-pH cementitious material has been proposed, referred to as CEBAMA reference mix (e.g. Vehmas et al., 2016). Cement paste and concrete specimens were cast and distributed to interested partners. In addition, the mix components have also been distributed to other partners so that samples can be mixed and casted directly at their own respective laboratories. As a result, it is expected that a relatively large dataset of the characterization of the reference mixes is obtained both for the fresh and degraded states. Several experiments performed with this mix in WP1 will in turn be modelled and interpreted within WP3.

In this contribution, the focus is on the cement paste samples casted at USFD. The goal of these experiments is to study the degradation of small samples when in contact with different synthetic groundwater compositions (Vasconcelos et al., 2017). Modelling of these experiments using reactive transport simulations requires the knowledge of the composition of the hydrated system at the beginning of the leaching tests, i.e. after the curing period. In this work, the hydrated composition of the cement paste is obtained by means of hydration modelling. This approach, based on the work by Lothenbach and Winnefeld (2006), is based on coupling a set of kinetic reactions of dissolution of the mix components with thermodynamic calculations. Given the low water-to-solid ratio of the mixes, it is expected that a significant hydration time is needed to reach a high degree of hydration. The results of the hydration model are presented in this contribution and its implications for the experimental leaching tests are discussed.

2.2 USFD EXPERIMENTS ON CEMENT PASTE

USFD is performing characterization and leaching experiments using two different cementitious systems: the NRVB high-pH cement (Vasconcelos et al., 2017) and a low-pH cement paste mix based on the CEBAMA reference cement (e.g. Vehmas et al., 2016). In this contribution, focus is on the low-pH cement paste. The composition of the mix used by USFD to cast cylindrical specimens of 15 mm height and 15 mm diameter is given in Table 2.1. It is identical to the CEBAMA reference mix, with the exception that quartz filler has not been added in USFD samples. The water-to-solid ratio is 0.25. Moreover, the curing conditions also differ. Samples were stored for 28 days in an oven at a temperature of 40ºC and under a relative humidity of 95%.

The models consider as input 1 kg of water, while the rest of mix components are scaled accordingly following the data in Table 2.1. The oxide composition of the CEM I 42.5 MH/SR/LA produced by CEMENTA AB (Anläggningscement) considered in the calculations is from SKB (2014). VTT and University of Surrey also measured the oxide composition, showing the variability of especially the C/S ratio. The oxide composition of silica fume (from Finnsementti Oy, originating from Elkem) was measured by Univ. Surrey, while the oxide composition of the blast furnace slag was measured by both VTT and Univ. Surrey. Given that the experimental method

used by Univ. Surrey is not very accurate and does not characterize for e.g. the NaO content, it is not used here to determine the oxide composition of CEM I and BFS. However, for silica fume it is the only available measure and is therefore used as input to the model.

Table 2.1. *Composition of low-pH cement paste mix used in experiments by USFD.*

Component	Amount ($g/100g_{solid}$)	Density (kg/m^3)	Volume fraction (-)	Surface area (m^2/g)
CEM I 42.5	37.5	3100	0.18	310
Silica fume	39.3	2300	0.25	26.09
Blast furnace slag	23.2	2900	0.12	0.40
Quartz filler	0	2650	0	-
Superplasticizer	6.0	1200	0.07	-
Water	25	1000	0.37	-
Total	131.0		1.00	1.00

Table 2.2. *Oxide composition of the components of the CEBAMA reference mix measured by different partners.*

		CEM I 42.5 MH/SR/LA (wt. %)			Silica Fume (wt. %)	Blast furnace slag (wt. %)	
Oxide	**M_w (g/mol)**	**SKB***	**Univ. Surrey**	**VTT**	**Univ. Surrey**	**VTT**	**Univ. Surrey**
CaO	56.08	64	67.72	64.7	1.46	41.5	43.13
SiO_2	60.08	21	17.6	18.1	93.1	32.8	32.3
Al_2O_3	101.96	3.5	3.42	3.61	1.44	10.6	9.85
SO_3	80.06	2.2	3.81	4.02	0.47	1.4	3.68
MgO	40.30	0.7	0.6	0.76	0.88	8.29	7.4
Fe_2O_3	159.69	4.6	5.17	5.17	0.91	0.81	0.74
K_2O	94.20	0.62	1.3	0.64	1.73	0.62	1.2
Na_2O	61.98	0.07	-	0.08	-	0.62	-
CO_2	44.01	2.2	-	1.32	-	-	-
MnO	70.94	-	0.21	0.28	-	0.42	0.34
TiO_2	79.87	-	0.17	0.29	-	2.04	1.36
SrO	103.62	-	-	0.03	-	0.05	-
V_2O_5	181.88	-	-		-	0.09	-
ZrO_2	123.22	-	-	0.01	-	0.03	-
	Total	*98.89*	*100*	*97.69*	*99.99*	*99.27*	*100*

** SKB (2014)*

Table 2.3. *Groundwater compositions used in leaching experiments: granitic and saline compositions from Gascoyne et al. (2002); clay composition from Vinsot et al. (2008).*

Concentrations	Granitic	Saline	Clay
Na (mmol/L)	2.8	140	55
K (mmol/L)	0.1	2.1	1.1
Ca (mmol/L)	0.5	19.9	7.5
Mg (mmol/L)	0.2	0.4	5.7
Cl (mmol/L)	2.1	172.7	52.5
HCO_3 (mmol/L)	2.0	2.0	-
SO_4 (mmol/L)	0.1	4.0	15
pH	8.2	7.7	7

The leaching experiments, also performed at 40ºC, were started immediately after the curing period. The ends of the cylinders were sealed with epoxy resin to allow only radial diffusion. Three different synthetic groundwaters are considered in the experiments: a granitic, a saline, and a clay composition (Table 2.3). Static dissolution experiments consider 60 mL vessels with 50 mL of each groundwater. The experimental setup is placed in an oven at 40ºC. Duplicates of the samples are also tested. Replacement of groundwater and sampling will take place every 2 months over a period of 1 to 1.5 years. Monitorization of pH and major ions will be performed.

Experimental data available from these tests correspond to the 1st Data Freezing (September 2017) and will be updated during 2018 (preliminary experimental results in March 2018 and 2nd Data Freezing in September 2018). The mineralogical composition of the hydrated cement paste after 28 days has been characterized by XRD, TGA-MS, and SEM. The phases identified are the following: alite, belite, hydrotalcite, portlandite, monosulfoaluminate, and monocarboaluminate. The porosity has been characterized by MIP and the value of total porosity obtained is 19 %, with a threshold pore entry radii below 0.2 µm. Micro-CT images of the hydrated cement paste have also been obtained on smaller samples. However, these smaller samples (2mm diameter) present a significant fraction of air bubbles and a poorly dispersion of silica fume. Therefore, these measurements may not be fully representative of the samples used in the leaching experiments.

2.3 MODELLING THE HYDRATION OF LOW-pH CEMENT PASTE

In order to characterize and determine the composition of the hardened cement paste after curing for 28 days, the hydration of the mix needs to be modelled. Reactive transport models then use the hydrated composition as initial condition. The result of the hydration modelling includes the phase assemblage of the cement hydrates, the total porosity and its distribution (gel and capillary porosity), and most importantly the porewater composition. To model hydration, the methodology developed by Lothenbach and Winnefeld (2006), now widely used for different cementitious systems, is used. It is based on coupling a set of kinetic reactions of dissolution of the mix components with thermodynamic calculations. A closed system is considered, mixing the exact amounts of Table 2.1 in a batch. Therefore, the effect of moisture transfer occurring during the curing period is disregarded. This is an important simplification, especially in the studied system. This is due to the very low water/solid ratio (0.25) and the small size of the samples (radius of 7.5 mm). In this case, water consumption (self-desiccation) will be partly compensated by moisture transfer from the curing chamber. The implications are discussed in the results section.

In previous work, in collaboration with Georg Kosakowski from PSI and Barbara Lothenbach from EMPA, the hydration of the CEBAMA reference mix concrete has been modelled using PHREEQC (Idiart et al., 2017) and GEMS (Kosakowski, 2017). That concrete mix is very similar to the mix used by USFD and has been adapted to the specificities of the current experiments. To this end, data of the composition of the raw materials form the 1st Data Freezing has been used.

The dissolution rates of the clinker phases (alite, belite, aluminate and ferrite) are taken from the empirical expressions proposed by Parrot and Killoh (1984). The dissolution rate of the blast furnace slag is taken from Schöler et al. (2017). The dissolution rate of the silica fume considered here corresponds to that of quartz from Palandri and Kharaka (2004), which is a pH-dependent transition state theory (TST) formulation. The specific surface areas of the cement, BFS, and silica fume are either specified directly by the providers or derived from particle size distribution from the providers (Table 2.1). These values were arbitrarily reduced to account for the effect of limited water content during the hydration of this type of mix and of the expected lack of full dispersion of silica fume particles. Apart from these kinetically-controlled reactions, all other chemical reactions are considered under thermodynamic equilibrium. The hydration simulation is performed at 40ºC,

correcting the kinetic rates of the clinker with activation energies from Lothenbach et al. (2008). The superplasticizer fraction is considered as chemically inert. The alkali uptake in C-S-H phases (Na and K) is considered using a cation exchange model based on Missana et al. (2017), with a CEC that depends on the C-S-H concentration and its C/S ratio (Hong and Glasser, 1999). Aluminium uptake in C-S-H is however not considered in the simulations. The thermodynamic database Thermochimie version 9b0 (Giffaut et al., 2014) is used.

2.4 RESULTS

As stated above, the PHREEQC calculations presented here consider 1 kg of water in the initial mix. The rest of components of the mix are scaled accordingly. The results presented below are given in volume (cm^3) per 100 g of solid, including all the binders. The dissolution of the clinker and binder components as a function of time are shown in Figures 2.1. Alite dissolves relatively fast: after 28 days of hydration almost 90% is dissolved. On the other hand, dissolution of belite, aluminate, and ferrite occurs much more slowly. The blast furnace slag also dissolves relatively slowly, which is due to the reduction of the rate as a function of the water content. Silica fume dissolves fast at the beginning, but after some hundreds of days the pH of the pore solution drops and therefore the dissolution of silica fume is significantly slowed down.

The evolution of the main phase assemblage of the cement hydrates is shown in Figure 2.2. Portlandite and C-S-H with C/S ratio of 1.6 rapidly precipitate. As hydration proceeds and silica is released from the binder dissolution, portlandite redissolves and C-S-H is gradually decalcified, ending up in a C-S-H with C/S ratio of 0.8 (only these three discrete phases are available in Thermochimie). Other phases present after long hydration period (larger than 100 days) are ettringite, ferrihydrite, calcite, hydrotalcite, and strätlingite. After 28 days, CSH1.6, portlandite, ettringite, monocorboaluminate (not shown) and hydrogarnet (C3AH6, not shown) are the stable phases. However, after 32 days of hydration, portlandite, monocarboaluminate, and C3AH6 are completely dissolved.

The evolution of the pH is shown in the previous figures. It reaches a maximum after ∼30 days (12.94) and gradually decreases as portlandite completely disappears and the C/S ratio of the C-S-H decreases. The pH stabilizes at around 10.2 after ∼2 years of hydration. The alkali uptake in the C-S-H, modelled here using a cation exchange model, also has an impact on the pH. The largest pH drop is observed when CSH1.2 total replacement by CSH0.8 takes place. At these values, the dissolution of silica fume and quartz filler is significantly low, and the system reaches a situation close to equilibrium.

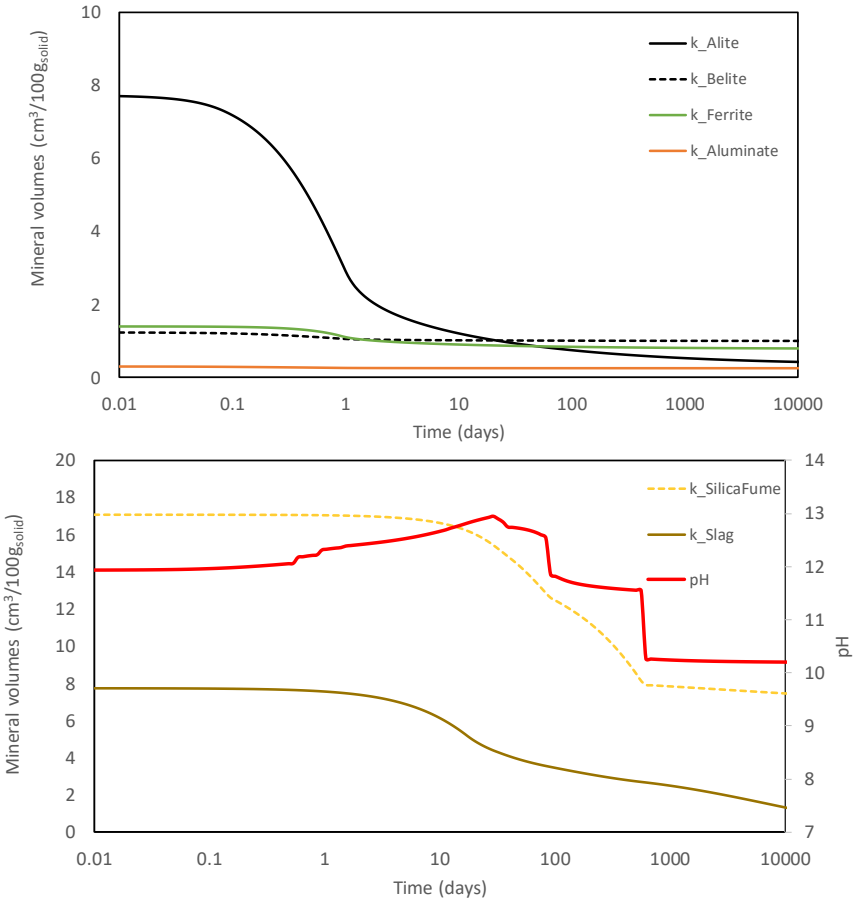

Figure 2.1. *Dissolution of the clinker phases and of blast furnace slag (k_Slag) and silica fume (k_SilicaFume) in cm^3/100g solid as a function of hydration time (days).*

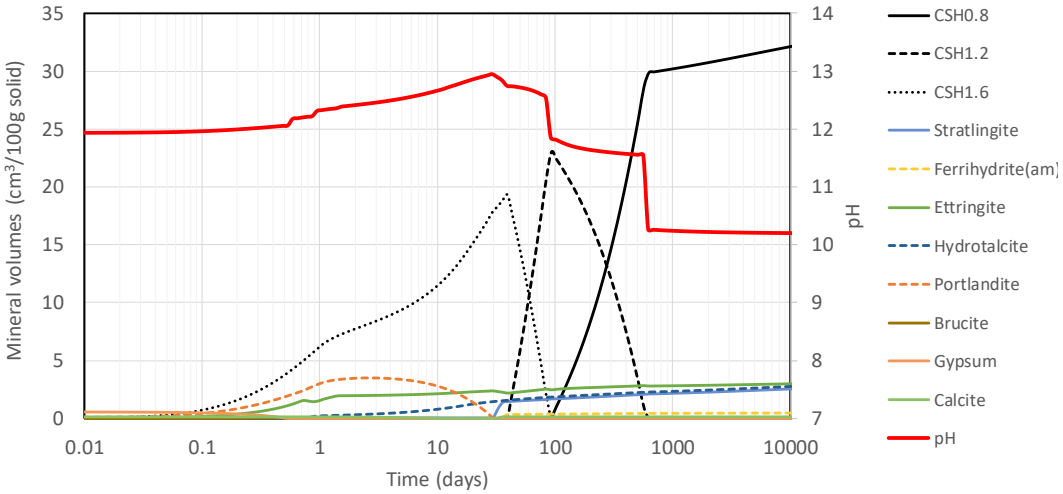

Figure 2.2. *Evolution of main cement hydrates (cm^3/100g solid) as a function of hydration time (days).*

The mineralogical phase assemblage in mol/kg$_{water}$ and porewater composition after 28 days and 365 days of hydration is shown in Table 2.4. It may be observed how the hydration is still significantly evolving between 1 month and 1 year of hydration, even if the amount of water is substantially reduced due to the closed system assumption. Note that this reduction in water leads to higher concentrations of clinker phases (in mol/kg$_{water}$) after 1 year compared to 28 days.

Table 2.4. *Model results of the mineralogical phase assemblage and porewater composition after 28 days and 365 days of hydration.*

Concentration (mol/kg$_w$)	**Hydration time (days)**			**Hydration time (days)**	
Mineral	28	365		28	365
Portlandite	0.189	0.000	pH	12.94	11.57
CSH0.8	0.000	53.061	Ionic strength (M)	0.394	0.041
CSH1.2	0.000	17.717	Water mass (g)	10.88	6.28
CSH1.6	19.420	0.000	Concentration (M)		
Ettringite	0.308	0.621	Al	7.85E-04	1.92E-04
Monocarbo-Al	0.310	0.000	Ca	9.43E-04	1.40E-03
Calcite	0.000	0.537	Fe	1.28E-06	5.14E-07
Hydrotalcite	0.592	1.535	C	5.69E-05	2.20E-05
Strätlingite	0.000	1.451	K	2.57E-01	1.97E-02
C_3AH_6	0.216	0.000	Mg	5.54E-10	7.31E-09
Ferrihydrite(am)	0.000	1.950	Na	1.56E-01	1.12E-02
Alite	1.194	1.313	S	7.61E-03	9.62E-03
Aluminate	0.271	0.468	Si	1.84E-04	8.51E-04
Belite	1.769	3.041			
Ferrite	0.617	1.012			
Silica fume	50.520	53.763			
Blast furnace slag	8.941	10.005			

The total porosity (ϕ_{tot}) can be calculated from the hydration simulation if autogenous shrinkage is neglected. To this end, equation 1 can be used, which can be shown to be equivalent to more traditional porosity update expressions as a function of mineral concentrations (equation 2, see e.g. Nardi et al., 2014). In these equations, V stands for volumes (litre), ϕ for volume fractions (litre/litre medium), M_v for molar volumes (litre/mol), and c_m for mineral concentrations (mol/litre medium). Subscripts *cem*, *water*, *hydrates*, *aggr*, *sp* and *inert* stand for unhydrated binder, water, cement hydrates, aggregates (zero in this case), superplasticizer (considered inert), and chemically inert fraction, respectively. The result as a function of hydration time is shown in Figure 2.3 together with the evolution of volume fraction of non-chemically bound water in the system (ϕ_w). The difference between these two quantities is the chemical shrinkage, ε_{ch} (litre/litre medium), see e.g. Mehta and Monteiro (2006), which is the reduction in volume due to the hydration reactions (equation 3). The value of total porosity after 28 days of hydration is 0.23, somewhat higher than the value of 0.19 measured experimentally (which is reached in the model after 90 days).

$$\phi_{tot} = \frac{V_{cem,0} + V_{water,0} - V_{cem,t} - V_{hydrates,t}}{V_{cem,0} + V_{water,0} + V_{aggr} + V_{sp}} \quad (1)$$

$$\phi_{tot} = 1 - \phi_{inert} - \sum_{i=1} c_{m,i} \cdot M_{v,i} \quad (2)$$

$$\varepsilon_{ch} = \phi_{tot} - \phi_w \quad (3)$$

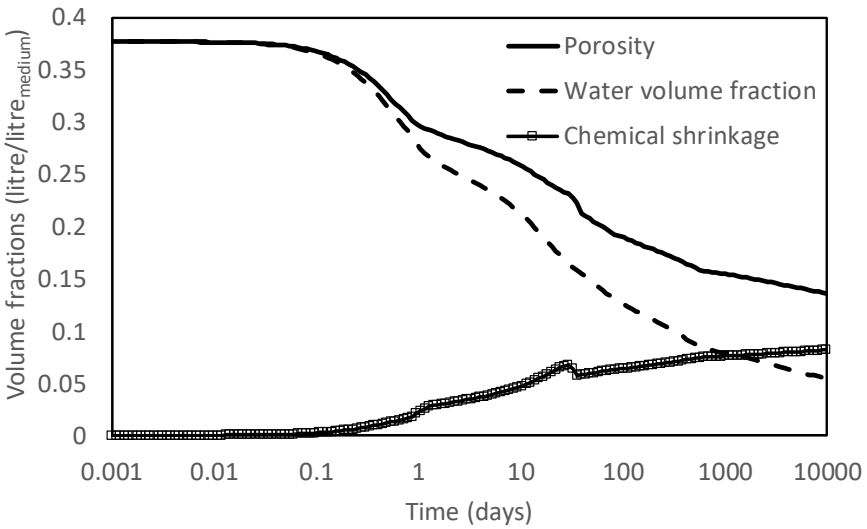

Figure 2.3. *Evolution of non-chemically bound water in the system, of total porosity (equation 1) and chemical shrinkage (equation 3) as a function of hydration time (days).*

As a result of the hydration, the internal degree of saturation can be significantly reduced. From Figure 2.3, after 28 days this reduction is from 1.0 to 0.7 litre water/litre pores. Therefore, further hydration is hindered by this lack of water. This is a consequence of the modelling approach, which assumes a closed system, i.e. water transfer from an external source is not included. Explicit consideration of the moisture transfer during hydration and curing at 95% relative humidity would lead to different results, i.e. a higher degree of hydration. Coupling of the hydration model to moisture transfer (e.g. Idiart et al., 2011) is currently on-going, although the desorption isotherm of this cement paste at different degrees of hydration, relating internal relative humidity to mass water content, would be rigorously needed. This coupling may be especially relevant for the present study, given the small dimensions of the samples.

2.5 PERSPECTIVES AND FUTURE WORK

The hydration of the low-pH cement paste samples that are used for leaching experiments by USFD has been modelled using thermodynamic calculations coupled to a set of kinetic equations for the dissolution of the cement mix components. Given the mix design of the reference CEBAMA cement paste, it is expected that hydration will continue to a significant degree for a much longer period than the 28 days, which has been considered as curing time in USFD experiments. As a result, modelling of the leaching experiments require to simultaneously consider hydration and reactive transport in the simulations. In addition, due to the low water-to-solid ratio and the small dimensions of the samples, it is expected that during the curing period, moisture transfer from the external conditions can play a non-negligible role in maintaining an internal relative humidity closer to saturation. On-going modelling work aims at coupling the three processes (i.e., hydration, reactive transport, and moisture transport) in a single model. The model results presented in this contribution are also being used within WP3 by JUELICH to setup a reactive transport model at the pore scale of the same experiments (see JUELICH contribution to this deliverable D3.05).

2.6 REFERENCES

Giffaut E., Grivé M., Blanc P., Vieillard P., Colàs E., Gailhanou H., Gaboreau S., Marty N., Madé B., Duro L. (2014). Andra thermodynamic database for performance assessment: ThermoChimie. Applied Geochemistry, 49, 225-236.

Hong S.-Y., Glasser F.P. (1999). Alkali binding in cement pastes. Part I. The C–S–H phase. Cem. Concr. Res., 29, 1893–1903.

Idiart A., López C.M., Carol I. (2011). Modeling of drying shrinkage of concrete specimens at the meso-level. Materials and Structures, 44(2), 415–435.

Idiart A., Coene E., Laviña M. (2017). Detailed description and Setup of the Modelling Task. CEBAMA Public Report. Available from the CEBAMA Intranet.

Kosakowski G. (2017). Contribution of PSI to Deliverable D3.05.

Lothenbach B., Le Saout G., Gallucci E., Scrivener K. (2008). Influence of limestone on the hydration of Portland cements. Cem. Conc. Res., 38, 848-860.

Lothenbach B., Winnefeld F. (2006). Thermodynamic modelling of the hydration of Portland cement. Cem. Concr. Res., 36(2), 209-226.

Mehta P. K., Monteiro P. J. (2006). Concrete: Microstructure, Properties, and Materials, Mc Graw-Hill, 3rd edition.

Missana T., García-Gutiérrez M., Mingarro M., Alonso U. (2017). Analysis of barium retention mechanisms on calcium silicate hydrate phases. Cem. Concr. Res., 93, 8–16.

Nardi A., Idiart A., Trinchero P., de Vries L.M., Molinero J. (2014). Interface COMSOL-PHREEQC (iCP), an efficient numerical framework for the solution of coupled multiphysics and geochemistry. Computers and Geosciences, 69, 10-21.

Palandri J.L., Kharaka Y.K. (2004). A compilation of rate parameters of water-mineral interactions kinetics for application to geochemical modeling. USGS-Report (2004-1068), Menlo Park, California, USA.

Parrot L.J., Killoh D.C. (1984). Prediction of cement hydration, Br. Cer. Proc. 35, 41-53.

Schöler A., Winnefeld F., Ben Haha M., Lothenbach B. (2017). The effect of glass composition on the reactivity of synthetic glasses. J. Am. Cer. Soc. 100, 2553–2567.

SKB (2014). Initial state report for the safety assessment SR-PSU. Report SKB TR-14-02.

Vasconcelos R.G.W., Idiart A. Hyatt N.C., Provis J.L., Corkhill C.L. (2017). Preliminary assessment of interaction between UK backfill cement material and groundwater. In Proc. 2nd Annual Workshop CEBAMA, Helsinki, Finland, May 2017.

Vehmas T., Schnidler A., Löija M., Leivo M., Holt E. (2016). Reference mix design and castings for low-pH concrete for nuclear waste repositories. In Proc. 1st Annual Workshop CEBAMA, Barcelona, Spain, May 2016.

3 BRGM/ P. Leroy, S. Gaboreau, F. Claret (BRGM), A. Hördt (Braunschweig Univ., Germany), S. Huisman (FZJ)

Abstract

This contribution presents the first results of the modelling of the spectral induced polarization (SIP) laboratory measurements on cement. Geophysical measurements were interpreted in terms of porosity and pore size distribution using a surface complexation combined with a transport model (membrane polarization model).

Keywords: spectral induced polarization, cement, electrical double layer, zeta potential, partition coefficient in the Stern layer, porosity, pore size distribution.

3.1 SPECTRA TO BE INTERPRETED AND SAMPLE PETROPHYSICAL AND WATER CHEMICAL PROPERTIES

SIP measurements on cement were provided by the research team of Professor Johan Alexander Huisman (FZJ). The main features of the spectra are shown in Figure 3.1. The data are characterized by very large resistivities (mostly > 10000 Ohm m), relatively large phase shifts (between injected current and measured voltage) (mostly > 40 mrad) at low frequencies (≤ 100 Hz), and extremely large phase shifts at high frequencies (> 100 Hz). The phase shift exhibits a moderate peak between 1 and 10 Hz for the concrete only. At this stage, we have not looked into the subtle differences between SIP of concrete and cement. The aim of the modelling is to be able to estimate the porosity and pore size distribution from the measured spectra, in order to monitor the reactive transport properties of cement.

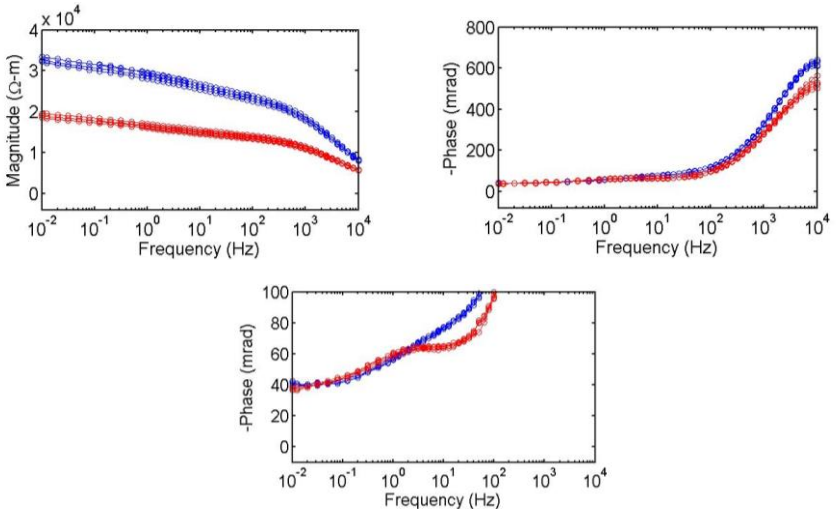

Figure 3.1. *SIP data measured on cement (blue) and concrete (red) samples. Top: Magnitude spectra. Middle: phase spectra. Bottom: zoom into low-frequency range of phase spectra.*

The porosity of the cement paste (CEBAMA reference mix design provided by VTT) was measured (35%) and the chemical composition of its bulk electrolyte (at equilibrium) was estimated using extracted interstitial solutions and the Phreeqc software (Table 1). The water chemical composition obtained is relatively approximate and further work is currently carry out to estimate it more accurately. Preliminary results show that the bulk electrolyte contains high concentrations of OH^- (7.6 mM), Ca^{2+} and SO_4^{2-} ions (~5-6 mM) and significant concentrations of Na^+ and K^+ ions (~4 mM). The geophysical model can only consider a binary symmetric electrolyte and we chose to

only consider for it the concentration of Ca^{2+} and SO_4^{2-} ions because they carry twice the charge of the other ions.

Table 3.1. *Chemical composition of the bulk electrolyte of our cement sample (pH=11.8). Concentrations in mM.*

Ca^{2+}	Na^{+}	K^{+}	H^{+}	OH^{-}	SO_4^{2-}
5.87	3.94	3.92	1.82×10^{-9}	7.60	6.12

3.2 GEOPHYSICAL AND SURFACE COMPLEXATION MODEL

The membrane polarization model developed by Bücker and Hördt (2013) was used to compute the SIP spectra. It consists in considering two cylindrical pores of different dimensions and surface electrical properties that exhibit an increase of their impedance at low frequencies of the injected sinusoidal current (between mHz and kHz) (Figure 3.2). The increase of the impedance is due to the presence of ion non-selective and selective zone responsible for the increasing polarization of the medium at low frequencies. For cement, the nanopores of calcium-silicate-hydrates (C-S-H) were assumed to be the ion selective zones and the macropores of siliceous materials were assumed to be the ion non-selective zones. The parameters of the membrane polarization model are the lengths and radii of the two pores, their zeta potentials and fractions of their counter-charge in the Stern layer at the solid/water interface (partition coefficient), and the electrolyte concentration. To give some indications of their values for cement, the zeta potentials and fractions of the counter charge in the Stern layer were also computed using the software Phreeqc and the surface complexation models of Kari et al. (2013) for C-S-H and Hiemstra et al. (1989) for amorphous silica, the last one being extended to describe the sorption of calcium counter-ions using the surface charge density measurements of Dove and Craven (2005).

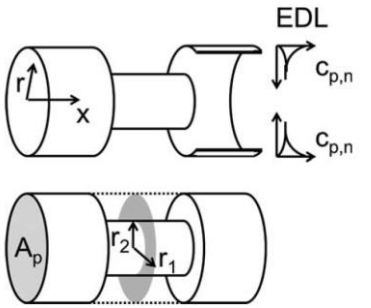

Figure 3.2. *Sketch of the membrane polarization model of Bücker and Hördt (2013) showing ion non-selective and selective zone (smaller pore). The variable $C_{p,n}$ is respectively the concentration of positive and negative charge on the wall. EDL means electrical double layer.*

Since with the original membrane polarization model of Bücker and Hördt (2013), some of the features in the SIP measured data cannot be reproduced, based on the work of Andreas Hördt (personal communication), the membrane polarization model has been extended by two aspects:
1) It now simulates the impedance of not only one pore but of two pore systems (each defined by 2 cylinders) in parallel. The pore systems are properly scaled such that the model can calculate the resistivity and phase shifts from the bulk impedance of the two parallel impedances. For each of the two pore systems, the model also considers a non-conducting matrix cylinder encompassing the pores. This allows to determine porosity and controls resistivity. The specific internal surface area is also calculated. The model can also consider the relative volumetric proportion of the two pore systems, i.e. it can require that 1 pore system (including the encompassing matrix) occupies 10 times more volume than the other one.

2) A displacement current term $1/i\,\omega\,\varepsilon$ is added to the resistivity, using 80 for the dielectrical permittivity of water ε (ω is the angular frequency).

3.3 RESULTS

We tried to reproduce the basic features of the measured SIP data by trial-and-error modelling. We did not use any inversion code or attempt to fit the spectra quantitatively. The current "best fit" model is characterized by the parameters given in Table 3.2, an electrolyte valence z = 2 and bulk ion concentration of 10 mM (according to Table 1). We considered negative zeta potential values for macropores (siliceous materials) and positive zeta potential values for nanopores (due to the sorption of Ca^{2+} ions). For nanopores, we did not consider mobile counter-ions in their Stern layer because calcium ions were assumed to be adsorbed very close to the surface as inner-sphere surface complex (Hou and Li, 2014). The volume shared by the pore system 1 is 200 times the volume shared by the pore system 2. Their non-conducting matrix has a respective thickness of 2 and 4 µm.

Table 3.2. *Parameters characterizing the 2-in-parallel membrane polarization model producing the spectra shown in Figure 3.3.*

	Radius (µm)	Length (µm)	Zeta potential (mV)	Partition coefficient
Pore system 1				
Wide pore	1	10	-50	0.5
Narrow pore	0.001	1	25	0
Pore system 2				
Wide pore	1	10	-50	0.5
Narrow pore	0.05	1	25	0

For this model, we obtained the spectra given in Figure 3.3. The porosity defined by the model is 35%. The model reproduces the main features of the data shown in Figure 3.1:
a) Resistivity of ~30000 Ohm m.
b) Phase peak between 1 and 10 Hz.
c) Extreme phase shifts at 10 kHz.

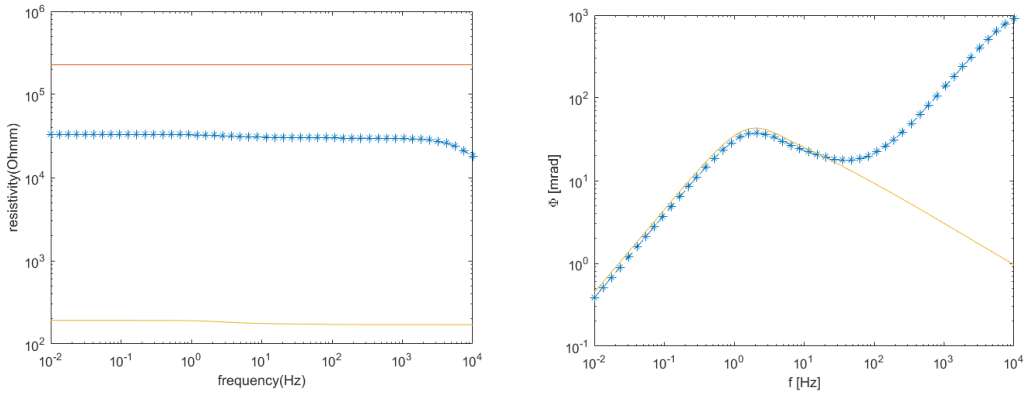

Figure 3.3. *Resistivity (left) and phase spectra (right) calculated for the membrane polarization model defined by Table 2. The blue stars denote the full response, the red and yellow lines are the separate responses of pore system 1 and 2, respectively.*

The model also has a large porosity of 35%, which was one of the main difficulties. Pore system 1 actually does not polarize (i.e. phase shift close to zero). It represents large pores connected by very small ones, and thus consists of "dead" pores. They increase porosity, and at the same time they have a very high resistivity. The very small pores may correspond to the interlayer space of C-S-H.

Pore system 2 is polarizable and produces the phase peak at 2 Hz. Therefore, only a tiny volume (1/200) of the whole pore space is responsible for the polarization, the rest is "dead pores". In general, the main difficulty is to explain the large resistivities and large porosities at the same time.

The extreme phase shifts at 10 kHz may be due to the displacement current term. This becomes strong, because the resistivities are so high. We did not look into any details, but in our opinion, the displacement currents are sufficient to explain the phase shifts. Other effects, like Maxwell-Wagner polarization, are probably not necessary. In our opinion, there is also some confusion in the literature about the Maxwell-Wagner effect. Normally, this is calculated by a mixing law. We believe that often, the simple displacement current dominates in these mixing laws. The "original" Maxwell-Wagner effect, which is due to the build-up of charge at the boundary between two materials, may not be really that important.

The phase peak in the simulated data is much sharper than the one in the measured data. This is due to the impedance of a simple pore system. In order to match the broad phase peak, one has to use an impedance network, or a distribution of pore lengths, instead of simple systems like this.

3.4 CONCLUSIONS AND PERSPECTIVES

We have developed a membrane polarization model to describe the laboratory spectral induced polarization measurements on cement and concrete in terms of porosity and pore size distribution. Our model is based on the assumption that the ion exclusion in the smaller (nanometric) pores is responsible for the polarization of the medium made of ion non-selective and selective zones. An improvement of the original membrane polarization model of Bücker and Hördt (2013) was carried out in order to be able to define in the model a porosity, another two-pore system and a dielectric displacement term. With the improved model, it was possible to reproduce quantitatively the very high resistivity, high porosity and phase shift of the cement. Nevertheless, we must include in the model a pore size distribution to be able to reproduce the flat phase spectra recorded a low frequencies (< 100 Hz). In addition, more work should be undertaken to describe accurately the surface electrical properties of cement and concrete.

3.5 REFERENCES

Bucker, M., Hordt, A. (2013). Analytical modelling of membrane polarization with explicit parametrization of pore radii and the electrical double layer. Geophysical J. Int., 194 (2), 804-813.

Dove, P. M., Craven, C. M. (2005). Surface charge density on silica in alkali and alkaline earth chloride electrolyte solutions. Geochimica Et Cosmochimica Acta, 69 (21), 4963-4970.

Hiemstra, T., J. C. M. De Wit, Van Riemsdijk, W. H. (1989). Multisite proton adsorption modelling at the solid/solution interface of (hydr)oxides: a new approach. II. Application to various important (hydr)oxides. Journal of Colloid and Interface Science, 133, 105-117.

Hou, D., and Li, Z. (2014). Molecular dynamics study of water and ions transport in nano-pore of layered structure: A case study of tobermorite. Microporous Mesoporous Materials, 195, 9-20.

Kari, O. P., Y. Elakneswaran, T. Nawa, Puttonen, J. (2013). A model for a long-term diffusion of multispecies in concrete based on ion-cement-hydrate interaction. Journal of Materials Science, 48 (12), 4243-4259.

7 JUELICH/ S. Rohmen, G. Deissmann, D. Bosbach (JUELICH), A. Idiart (AMPHOS 21)

Abstract

Pore-scale models represent an appealing approach to include a more accurate and mechanistic description of physical and chemical processes occurring in heterogeneous porous media such as cementitious materials or clay rocks. Here we describe approaches to derive microstructural information of cement-based materials from scanning electron microscopy data and micro X-ray computer tomography. The reconstructed geometric data from two different samples are used as input for pore-scale simulations using a modelling framework based on the Lattice Boltzmann method. Based on the microstructural data, effective diffusion coefficients for the two samples were derived using the Lattice-Boltzmann based code iPP.

Keywords: pore-scale modelling, Lattice-Boltzmann-Method, microstructural analysis, geometry reconstruction, diffusivity

7.1 INTRODUCTION

In the frame of the CEBAMA project, a pore-scale reactive transport modelling framework for the simulation of concrete degradation processes is developed. Compared to continuum-scale models, pore-scale models can be used to obtain a more accurate and mechanistic description of physical and chemical processes in heterogeneous porous media such as cement-based materials. Processes of interest to be addressed with this approach within CEBAMA comprise chemical degradation processes due to calcium leaching and the carbonation of cementitious materials and its impact on physical properties, such as porosity, pore-size distribution, permeability or diffusivity (Taylor 1997).

The pore-scale reactive transport modelling framework, named *iPP* (Rohmen et al. 2017), couples Palabos (Flowkit 2011) and PhreeqC (Parkhurst and Wissmeier 2015). *iPP* will be used to model experiments performed within WP1 of CEBAMA, namely leaching experiments conducted at USFD and USURREY, which address the leaching of cementitious materials (e.g. CEBAMA VTT reference paste and Nirex Reference Vault Backfill NRVB) in various types of groundwaters (saline, granite and clay synthetic waters).

Recently, experimental data from the 1st Data Freezing on the characterization of the low-pH cement paste prior to leaching were made available from JUELICH and USFD. These data encompass in particular imaging data from scanning electron microscopy (SEM/EDX) and micro-X-ray computer tomography (µXCT), which will be used as input data for the materials microstructure for pore scale simulations using iPP. Here we describe our approach for geometry reconstruction from both, SEM/EDX measurements and µXCT and a procedure to derive effective diffusion coefficients from the microstructural analysis.

7.2 GEOMETRY RECONSTRUCTION FROM SEM/EDX

A sample of the VTT CEBAMA reference paste (age on preparation 404 days) was cut using a diamond saw, polished and analyzed by SEM/EDX, using a Quanta 200F instrument (FEI) equipped with an Apollo X silicon drift Detector (EDAX) by JUELICH. With help of EDX technique the resulting 2D pixel maps are enriched with spectroscopic data corresponding to the elemental composition. Since the SEM grey values alone only provide limited information about spatial distribution of cementitious phases, the spectroscopic information per pixel was used to reconstruct the phase assemblage and microstructure.

For this purpose, an input reader for the proprietary raw data output format of the EDAX software was implemented. With this, all spectral pixel data were available as data arrays and a phase mapping and geometry reconstruction algorithm could be implemented. In order to reduce noise in the spectroscopic data, 2*x*2 pixels were averaged. Eight reference domains were manually selected for different phases, based on their chemical composition, i.e. quartz, silica fume, blast furnace slag, C_2S/C_3S, C_4AF, some form of FeS, graphite and hydration products. Thereafter, averaged spectral reference data were extracted from these domains and assigned to the respective phase.

These reference spectral data are fed into a newly implemented algorithm which performs an error minimization step for each pixel in which the error is determined by comparing linear combinations of the reference spectra by the spectra of each pixel. After finding the minimum error combination with help of a golden section search algorithm (Press et al. 2002, pp. 379), the major phase (i.e. with the highest weighting) is assigned to the pixel (see Figure 7.1).

Figure 7.2 shows the resulting phase distribution in the hardened VTT cement paste based on the mapped data. Qualitative comparison shows similar results to the microstructure as from visual inspection of the raw SEM/EDX image. The total model size is 512 *x* 400 pixels with a resolution of 1.852 µm per pixel (corresponding to a total physical size of 948 *x* 741 µm).

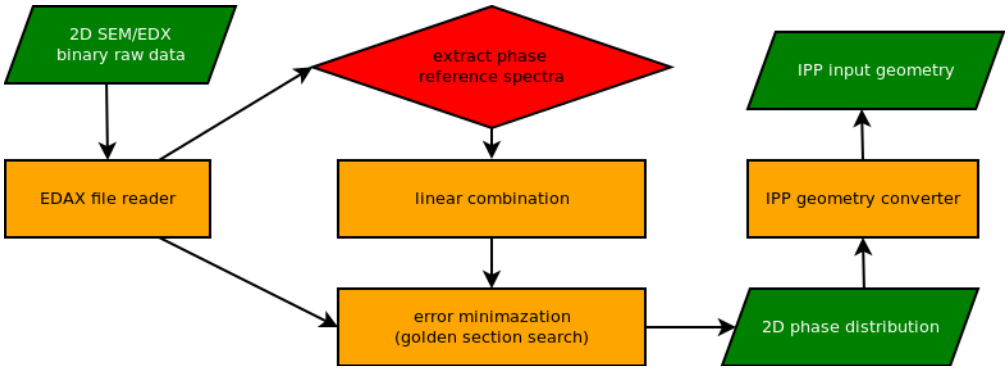

Figure 7.1. *Schematic representation of the phase detection algorithm for EDX spectroscopic data.*

7.3 GEOMETRY RECONSTRUCTION FROM µXCT DATA

µXCT data taken on samples from the CEBAMA reference paste (casted at USFD, dimensions 2 mm diameter and 5 mm height) were provided by USFD. In contrast to the original VTT reference mix, this cement mixture did not contain quartz filler (see Amphos 21 contribution in this deliverable D3.05 for more details). The sample was cured for 28 days and measured by µXCT with a resolution of 3 µm per voxel, resulting into a grey value data set of 671 *x* 742 *x* 1449 = 721 431 018 voxels.

From the grey scale images, six different grey value ranges were outlined, corresponding to certain materials phases. A common artifact known from CT measurements is the so-called partial volume effect, also known as volume averaging artifact.

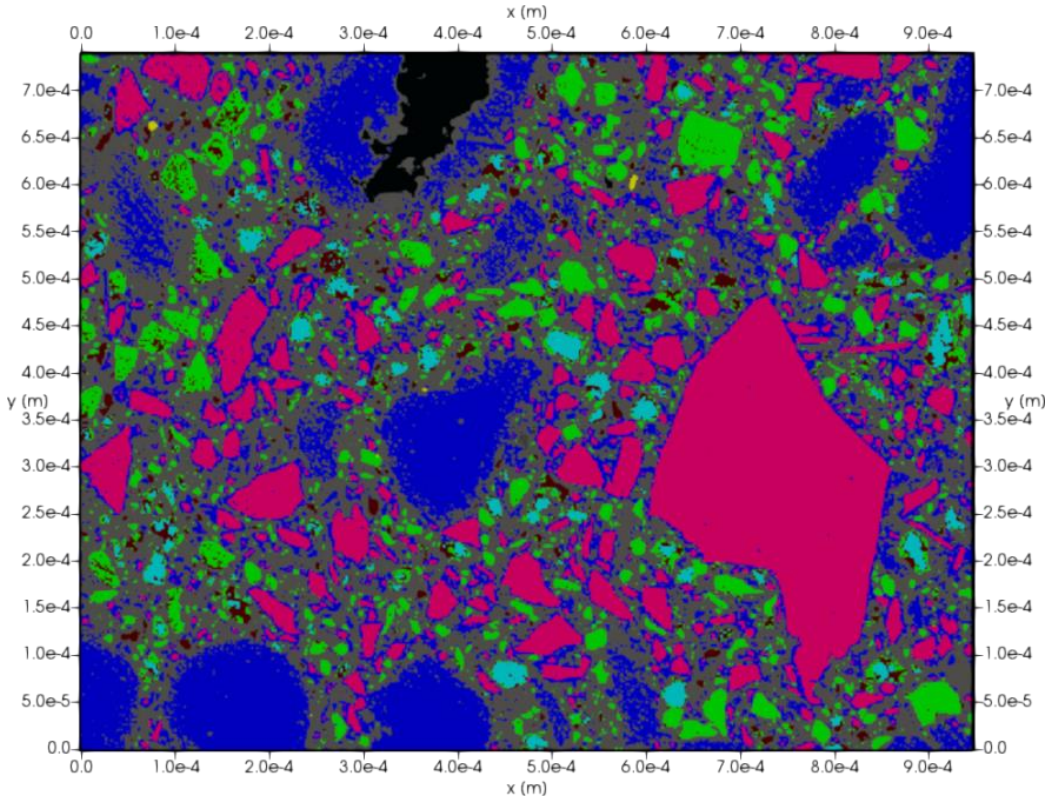

Figure 7.2. *Segmented phases from SEM/EDX measurement data of VTT reference cement paste. Phases: Quartz (pink), silica fume (blue), blast furnace slag (green), alite/belite (light blue), ferrite (brown), small amount of FeS (yellow, see top left corner), graphite (black), and hydration products, primarily CSH (grey).*

This artifact occurs when a single voxel contains more than one phase, leading to an intermediate X-ray attenuation value between all material fractions present in the voxel's volume. For this reason, using a simple thresholding segmentation scheme for relating the different phases to grey values would eventually lead into false positive assignments for voxels corresponding to phase mixtures (Ketcham and Carlson 2001). In order to mitigate this effect, an algorithm was developed which is based on canny edge detection and an image masking step, followed by removal of the intermediate voxels in first place before performing a threshold range segmentation. The prototype development of this scheme is sketched in Figure 7.3. After application, gaps between different phases occur in the images, which were filled by using a newly developed volume fill scheme. This algorithm applies a Gaussian smoothing of each input image and prevents intersecting with other phases at the same time. As a consequence, the gaps are only partially filled with distinct phases. In the next step, at each gap voxel the phase with the maximum fraction in the neighbouring voxels is selected and assigned to it. The above scheme is repeated until a phase is assigned to all empty gap voxels. This µXCT image processing with partial volume artifact mitigation leads potentially to edge/surface smoothing and loss of insufficient resolved geometries (i.e. small volumes below µCT resolution can be lost).

Application to the USFD sample is shown in Figure 7.4. The segmented data from the cylindrical sample of the VTT CEBAMA reference paste show quasi-spherical silica fume particles with a diameter up to 300 µm and a significant number of air inclusions and cracks, connecting spherical pores with a diameter up to 500 µm. Air bubbles occur in particular in the lower Z-domain, which might be due to buoyancy effects during curing and possibly measurement of the sample upside down.

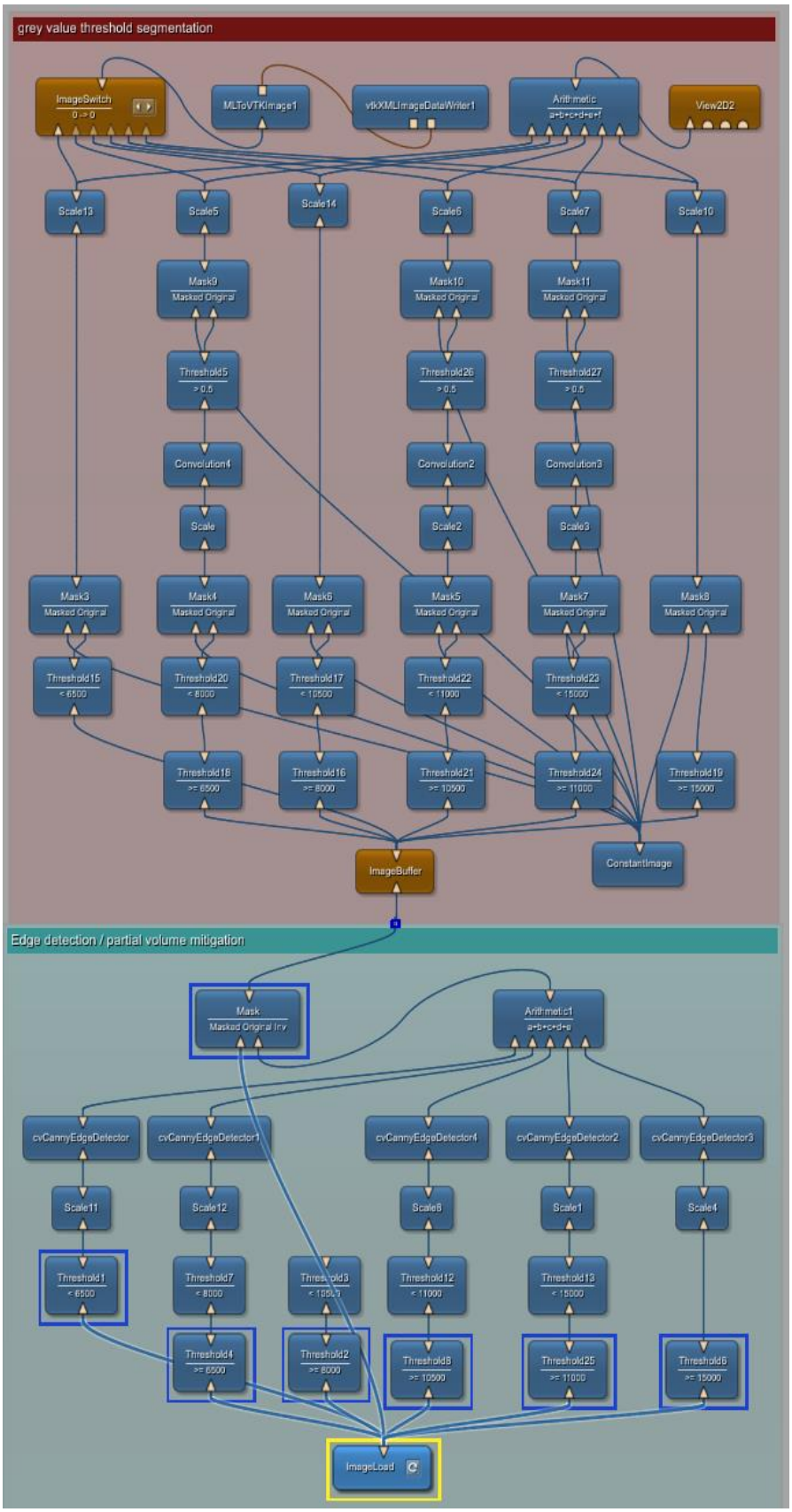

Figure 7.3. *First part of µXCT data segmentation algorithm. Partial volume artifact mitigation (bottom/green) and grey threshold value separation (top/red).*

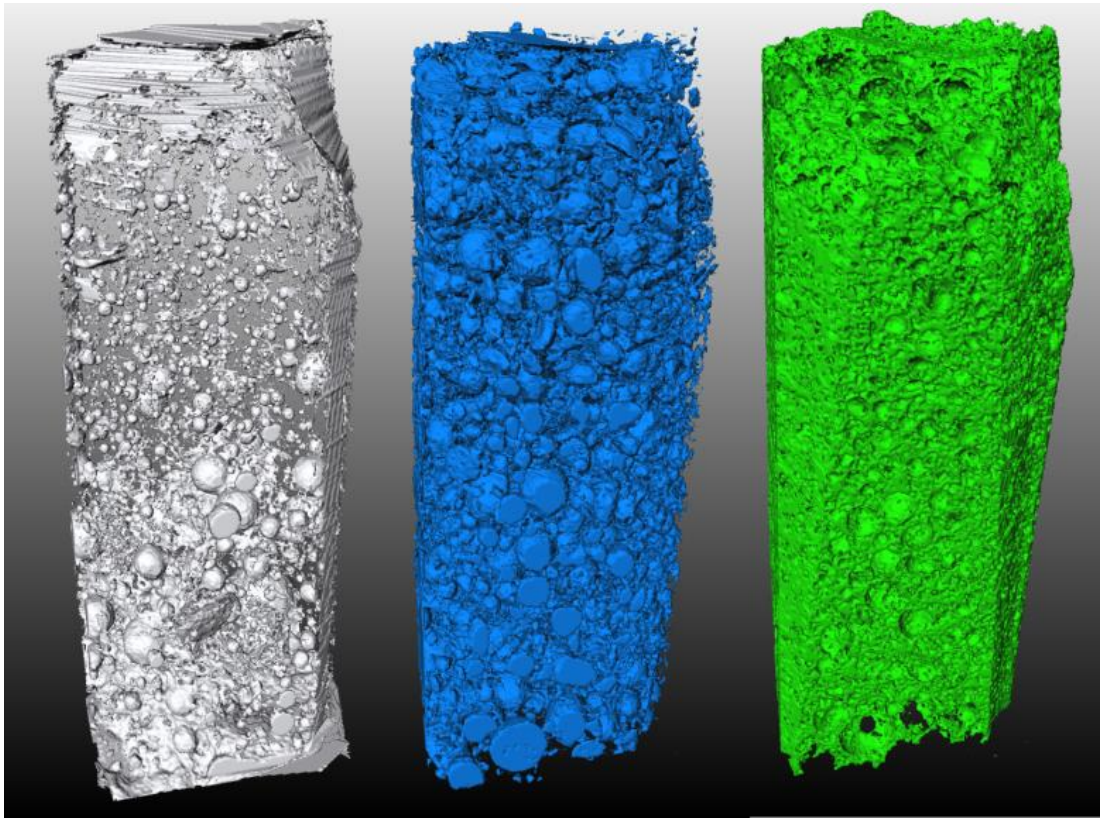

Figure 7.4. *Segmented phases from µXCT measurement data of the USFD cement mix. Phases shown: Air (left/white, out-of-cylinder volume cropped), silica fume (centre/blue) and hydration products, i.e. primarily C-S-H (right/green).*

7.4 CALCULATION OF EFFECTIVE DIFFUSION COEFFICIENTS

Both geometries derived from the segmented data of SEM/EDX and µXCT measurements were used as geometric input data for iPP to determine the effective diffusion coefficients in X and Y direction. For this, a through diffusion test on the microstructure was simulated. The model consists of the geometry described above with closed (slip) boundary conditions assigned to all boundaries, except those corresponding to the axis to be measured. At these boundaries, a constant concentration (Dirichlet) boundary condition of either 1 mol/L (left/bottom) or 0 mol/L (right/top) of inert tracer was imposed. According to Fick's first law, the diffusive flux J in relation to the diffusion coefficient D and concentration gradient ∇c is defined as:

$$J = -D \cdot \nabla c$$

Therefore, at steady state, the diffusion coefficient is equivalent to the quotient of the flux and the concentration gradient. In both geometry models, the diffusivity of the hydration products was linked to the diffusivity of C-S-H. For both cases, a homogeneous distribution of diffusive hydration products as C-S-H and other (crystalline) hydration products was assumed, since the imaging techniques used are not able to resolve hydration products in a separate way. All other segmented phases like silica fume, quartz, blast furnace slag and clinker were assumed as non-diffusive for the inert tracer.

It has to be pointed out that both data sets are not completely comparable since the USFD paste did not contain quartz filler and was measured after 28 days of curing and casted by USFD themselves, while the data produced by JUELICH treated the original reference material from VTT. In contrast, the VTT reference material did actually contain quartz filler and the silica fume was pre-dispersed by high speed mixture devices and had an age of 400 days on preparation date. These differences in

casting process and age, and curing time (degree of hydration) can probably have a non-negligible effect on the microstructure and on the phase composition as well.

VTT reference cement using reconstructed SEM/EDX geometry:

For the SEM/EDX based simulation, a diffusion coefficient of 1.0E-12 m^2/s for the hydration products (CSH) was assumed, using the input geometry depicted in Figure 7.2. Flux convergence was reached after 17.5 mio. iterations (corresponding to 10 mio. s in physical time) and 5 mio. iterations (corresponding to 3 mio. s in physical time) for x and y, respectively. The resulting concentration profiles and fluxes are depicted in Figure 7.5.

Dividing the steady-state outlet flux by the concentration gradient, effective diffusion coefficients of 1.5E-14 m^2/s and 4.4E-14 m^2/s for x and y direction, respectively, were determined. Relating the effective diffusion coefficients with the assumed diffusion coefficient for C-S-H results in a relative diffusivity of 0.0145 and 0.044 in x and y direction. Therefore, average relative diffusivity is 0.029. The distinctively lower diffusivity in x direction can be explained by the huge quartz filler grain, which was included in the input geometry on the right-hand side. Thus, it has to be emphasized that the selection of a representative geometry plays a crucial role for determining isotropic effective transport properties in these materials.

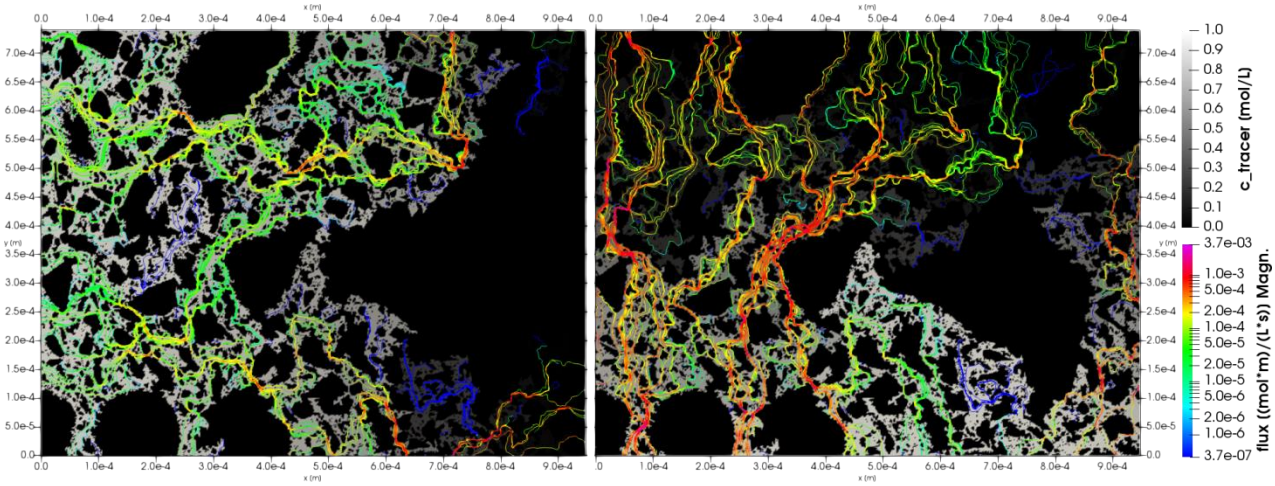

Figure 7.5. *Steady-state diffusion results of inert tracer in VTT reference paste for x (left) and y (right) direction. Concentration profiles are indicated in grey background values while diffusive flux streamlines are coloured in foreground.*

UFSD cement using reconstructed µXCT geometry:

In order to calculate the effective diffusive properties in a similar way as for the SEM/EDX based geometries, a rectangular section of the original 3D image data was extracted. The domain selected originates at the upper part of the scan (in terms of Z), in order to have limited amount of air inclusions, since the imaging and porosimetry results for the VTT reference material indicated only a small amount of porosity with volumes exceeding a few microns in diameter. In total, an image containing 250 *x* 250 pixels was extracted leading to a total system size of about 750 *x* 750 µm (see Figure 7.6).

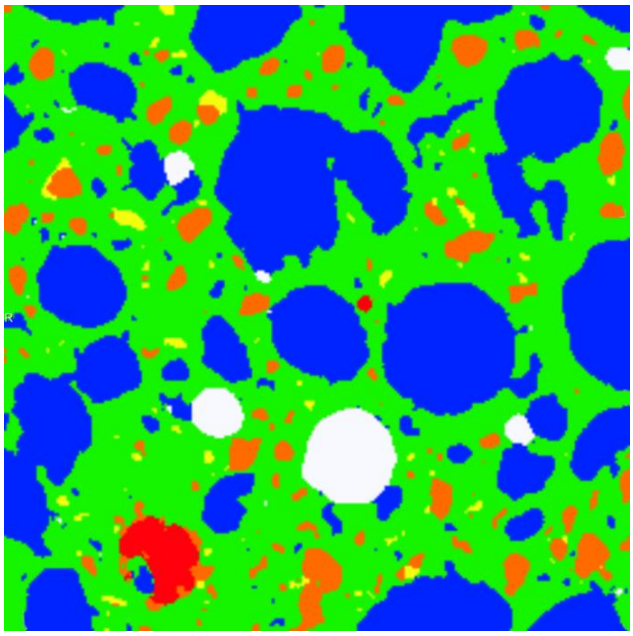

Figure 7.6. *Rectangular slice from segmented µXCT data used as input geometry for the calculation of effective diffusion coefficients. Phases: Air (white), silica fume (blue), alite/belite (yellow), blast furnace slag (orange), ferrite (red) and hydration products (green). Total model size is 750x750 µm with a resolution of 3 µm.*

Phase	amount [mol/L_{hp}]	volume fraction [L/L_{hp}]
CSH1.6	5.159	0.402
Ettringite	0.072	0.051
Monocarboaluminate	0.075	0.020
Hydrotalcite	0.140	0.031
Stratlingite	0.135	0.029
C3AH6	0.034	0.005
Inert/Superplasticizer	-	0.111
Hydrates total porosity	-	0.351

Table 7.1. *Calculated amount of hydration product (hp) phases and volume fractions in the USFD cement paste.*

The composition and total porosity of the hydration products were determined by modelling the hydration with PhreeqC (Table 7.1, see Amphos 21 contribution for more details). In order to estimate the diffusion coefficient of the hydration products, a multiscale homogenization model was implemented. As first step, a water-to-cement ratio of 0.25 and a degree of hydration of 0.6 was assumed as input for the model of Tennis and Jennings (2000), in order to distinguish low-density (LD) and high-density (HD) C-S-H.

As next step, the effective medium approach of Phan-Thien and Pham (2000) was used to determine the C-S-H matrix diffusion coefficients for the given total porosity. For this an intrinsic gel porosity of 0.38 and 0.26 for LD and HD C-S-H, respectively (Bary et al., 2014), spherical C-S-H building blocks and a diffusion coefficient in gel water of 1.0E-9 m^2/s was assumed. All other hydration products were assumed as non-diffusive inclusions embedded in the C-S-H matrix. The sum of their volume fractions and the C-S-H matrix diffusion coefficient was used to apply the Mori-Tanaka effective medium approach (Zheng and Du 2001, Bary et al. 2014).

All in all, this led to a diffusion coefficient of inert tracer in C-S-H/hydration products of 3.0E-10 m^2/s which was subsequently used in the transport calculation. The value seems quite high for C-S-H gel which is due to the assumption that the complete C-S-H gel pore volume is available for diffusion and the assumption of spherical building C-S-H blocks. The development of a more physical accurate model describing the nano-scale behaviour of the C-S-H phase is currently in progress.

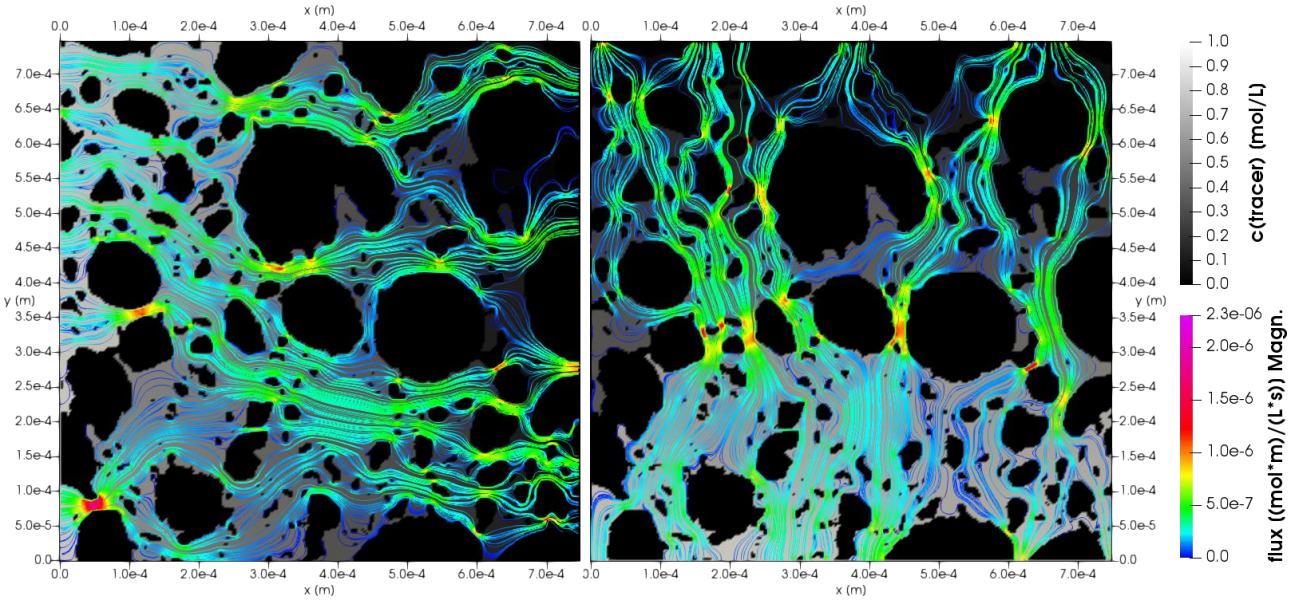

Figure 7.7. *Steady-state diffusion results of inert tracer in USFD HCP mixture for x (left) and y (right) direction. Concentration profiles are indicated in grey background values while diffusive flux streamlines are coloured in foreground.*

Since the model does also include free pore space, a value of 1.0E-9 m^2/s was used as free water pore diffusion coefficient for the inert tracer. Steady-state was reached after 1.3 mio. iterations (equals to 4000 s physical time) for x direction and 0.85 mio. iterations (equals to 2500 s physical time) for y direction. The resulting concentration profiles and fluxes are visualized in Figure 7.7. From the outlet fluxes, effective diffusion coefficients of 8.51E-11 m^2/s and 8.55E-11 m^2/s were estimated for x and y direction, respectively. Both values are quite similar leading to the conclusion that the diffusivity is isotropic for the depicted sub-geometry of the USFD cement paste derived from the µXCT data set. Relating the effective diffusion coefficients to the matrix diffusion coefficient of the hydration products yields a relative diffusivity value of approximately 0.085.

<u>Comparison of USFD/µXCT and JUELICH/SEM results:</u>
Besides the already mentioned differences in the input data the results are not directly comparable on absolute scale due to the different assumptions made in terms of C-S-H/hydration product diffusivity. Nevertheless, the relative diffusivities determined from the effective diffusion results are comparable to some extent since the diffusive matrix contained primarily hydration products only and only minor amount of other diffusive domains (meso-pores in case of USFD data). For the USFD data 0.085 was determined while for the JUELICH input an average value of 0.029 was obtained. Concluding on these scalar values the diffusivity obtained from the USFD data is three times higher than for the JUELICH data set. This outcome can be explained by the fact that the JUELICH model included diffusivity reducing quartz filler and smaller grains of slag while the USFD model, in contrary, contained diffusivity increasing meso-pores. In order to confirm this result and analyse uncertainties further samples have to be measured and simulated.

7.5 CONCLUSIONS AND FUTURE WORK

Recently, first imaging data of the VTT CEBAMA reference paste were provided from CEBAMA experimental groups, which can serve as input data for reactive transport simulations at the pore-scale (sub mm scale). Several algorithms and approaches were developed and implemented to derive microstructural information in appropriate format from raw data from SEM/EDX and µXCT

for subsequent usage in iPP. It could be shown that the developed framework iPP is capable of simulating solute transport in experimentally-derived data.

On-going efforts are dedicated to the coupling of diffusion with chemical reactions at this scale. Future simulations will address the degradation of the cementitious materials due to leaching with different waters. Calculation of diffusivities will be repeated for degraded cementitious materials in order to quantify the effect of alteration and degradation on the transport properties. The simulation results will be compared to experimental data from USFD (leaching and degradation) and USURREY (HTO diffusion) when available.

7.6 REFERENCES

Bary, B., Leterrier, N., Deville, E., and Le Bescop, P. (2014). Coupled chemo-transport-mechanical modelling and numerical simulation of external sulfate attack in mortar. Cement and Concrete Composites, 49, 70–83.

FlowKit. (2011). Palabos user guide.

Ketcham, R. A., and Carlson, W. D. (2001). Acquisition, optimization and interpretation of x-ray computed tomographic imagery: Applications to the geosciences. Computers and Geosciences, 27(4), 381–400.

Parkhurst, D. L., and Wissmeier, L. (2015). PhreeqcRM: A reaction module for transport simulators based on the geochemical model PHREEQC. Advances in Water Resources, 83, 176–189.

Phan-Thien, N., & Pham, D. C. (2000). Differential multiphase models for polydispersed spheroidal inclusions: Thermal conductivity and effective viscosity. International Journal of Engineering Science, 38(1), 73–88.

Press, W., Teukolsky, S., Vetterling, W., and Flannery, B. (2002). Numerical Recipes in C: The Art of Scientific Computing. Technometrics (2nd edition). Cambridge: Cambridge University Press.

Rohmen, S., Idiart, A., Deissmann, G., and Bosbach, D. (2017). Implementation of crystallization and precipitation mechanism in pore-scale models based on the Lattice-Boltzmann method, In Proceedings of the 2nd Annual Workshop of CEBAMA project, Espoo, Finland, May 2017 (in press).

Taylor, H. F. W. (1997). Cement chemistry. Thomas Telford.

Tennis, P. D., and Jennings, H. M. (2000). A model for two types of calcium silicate hydrate in the microstructure of Portland cement pastes. Cement and Concrete Research, 30(6), 855–863.

Zheng, Q. S., and Du, D. X. (2001). An explicit and universally applicable estimate for the effective properties of multiphase composites which accounts for inclusion distribution. Journal of the Mechanics and Physics of Solids, 49(11), 2765–2788.

9 NRG/ H. Meeussen

9.1 INTRODUCTION

During the reporting period, the work undertaken by NRG has focused on the following subjects:

1) Implementation of an electromigration term and multicomponent diffusion within the ORCHESTRA framework (Meeussen, 2003);
2) Performing scoping calculations for the cement clay diffusion experiments carried out at the TU-Delft.

9.2 IMPLEMENTATION OF ELECTROMIGRATION MODULE WITHIN THE ORCHESTRA FRAMEWORK

A multicomponent diffusion / electro-migration module was implemented in the ORCHESTRA modelling framework. This module takes into account the effect of electric potential on ion diffusion rates. In contrast with existing implementations this implementation not only allows simplified calculations for zero charge fluxes, but can also calculate ion diffusion rates under given electric potential gradients. The method takes into account individual diffusion coefficients for aqueous species and is fully compatible with existing reactive transport calculations. The module can use concentration or activity gradients as driving force for diffusion.

The new model was evaluated by reproducing the 1D diffusion calculation benchmarks described in the paper by Rasouli et al. (2015). The calculated results of two benchmarks agree very well with the reported results (Figure 9.1 and Figure 9.2), which indicates that the implementation in ORCHESTRA is correct.

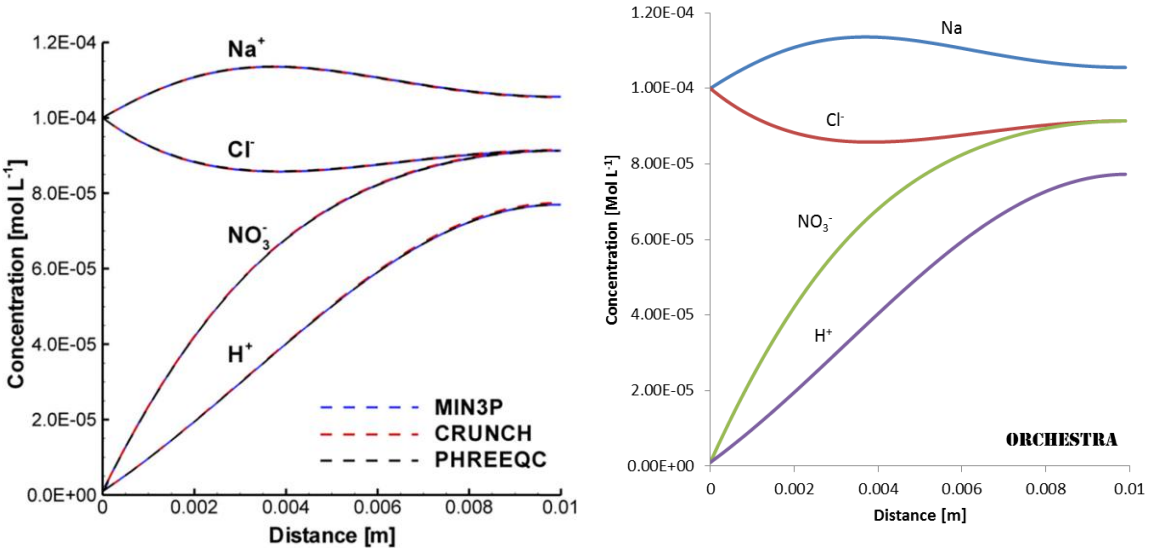

Figure 9.1. *Comparison of electromigration model results of Benchmark 1 between MIN3P, CRUNCH, PHREEQC (left), and the implementation in the code ORCHESTRA (right).*

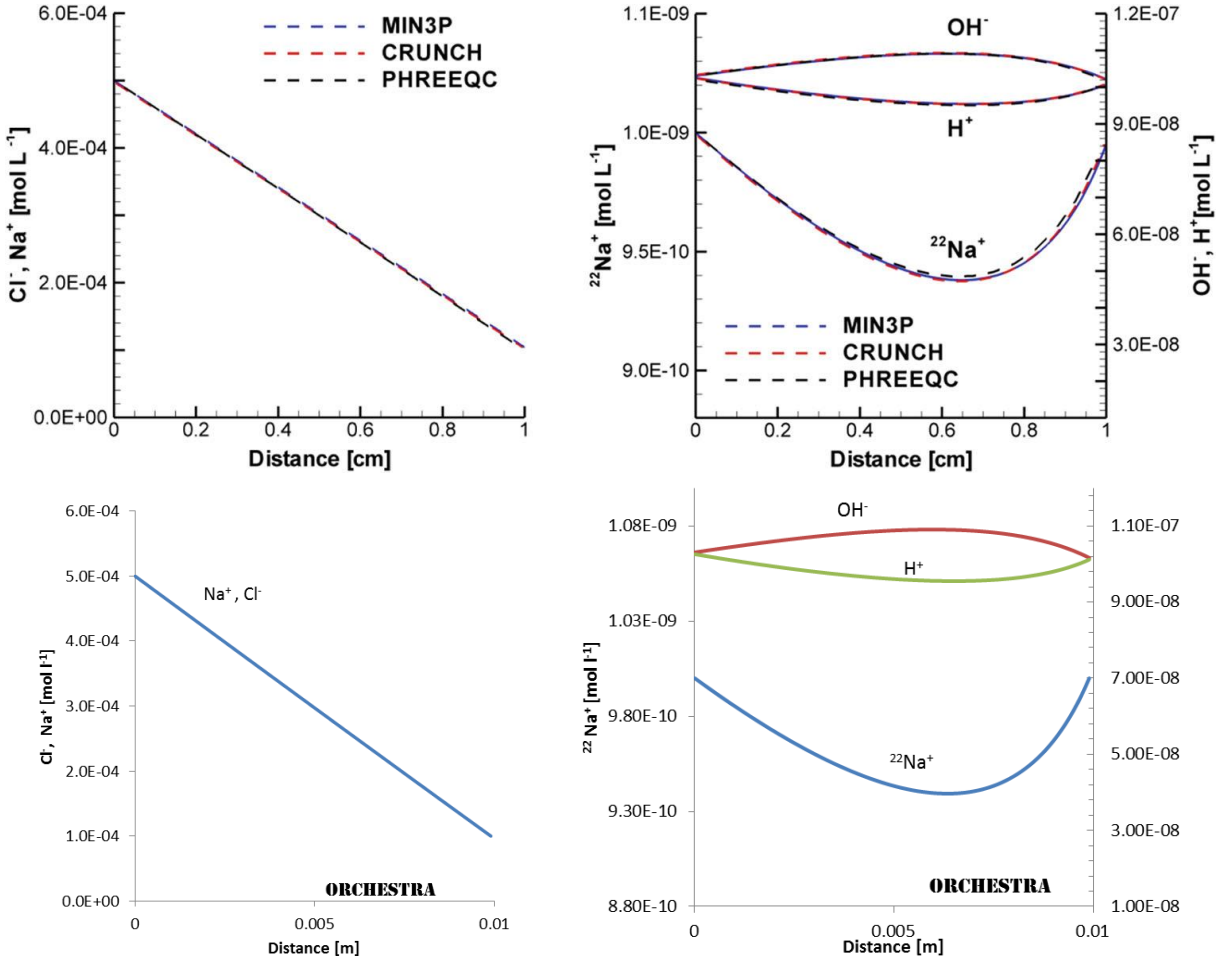

Figure 9.2. *Comparison of electromigration model results of Benchmark 2 between MIN3P, CRUNCH, PHREEQC (top), and the implementation in the code ORCHESTRA (bottom).*

9.3 SCOPING CALCULATIONS OF CEMENT CLAY INTERACTION EXPERIMENTS CARRIED OUT BY TU-DELFT

Over the reporting period we have implemented a diffusion model for migration in a Boom Clay - Concrete system that aimed to assist with set up of experimental work by TU-Delft. The cement model includes the latest CEMDATA14 thermodynamic database with chemical reactions specific of cementitious systems (EMPA, Lothenbach).

The clay model includes equilibrium with charged clay surfaces (Donnan model), organic matter surfaces (NICA-DONNAN model), iron oxides (Generalized 2-layer model), and mineral equilibrium with calcite and pyrite. The input for this model are the physical and chemical parameters of the clay and concrete sub-systems, and the model calculates concentration profiles in the diffusion system as a function of time.

This model was used to design the Cement-Clay interaction experiment and to estimate the time and spatial scales over which alterations are to be expected. Figure 3 below shows parameter profiles resulting from the model.

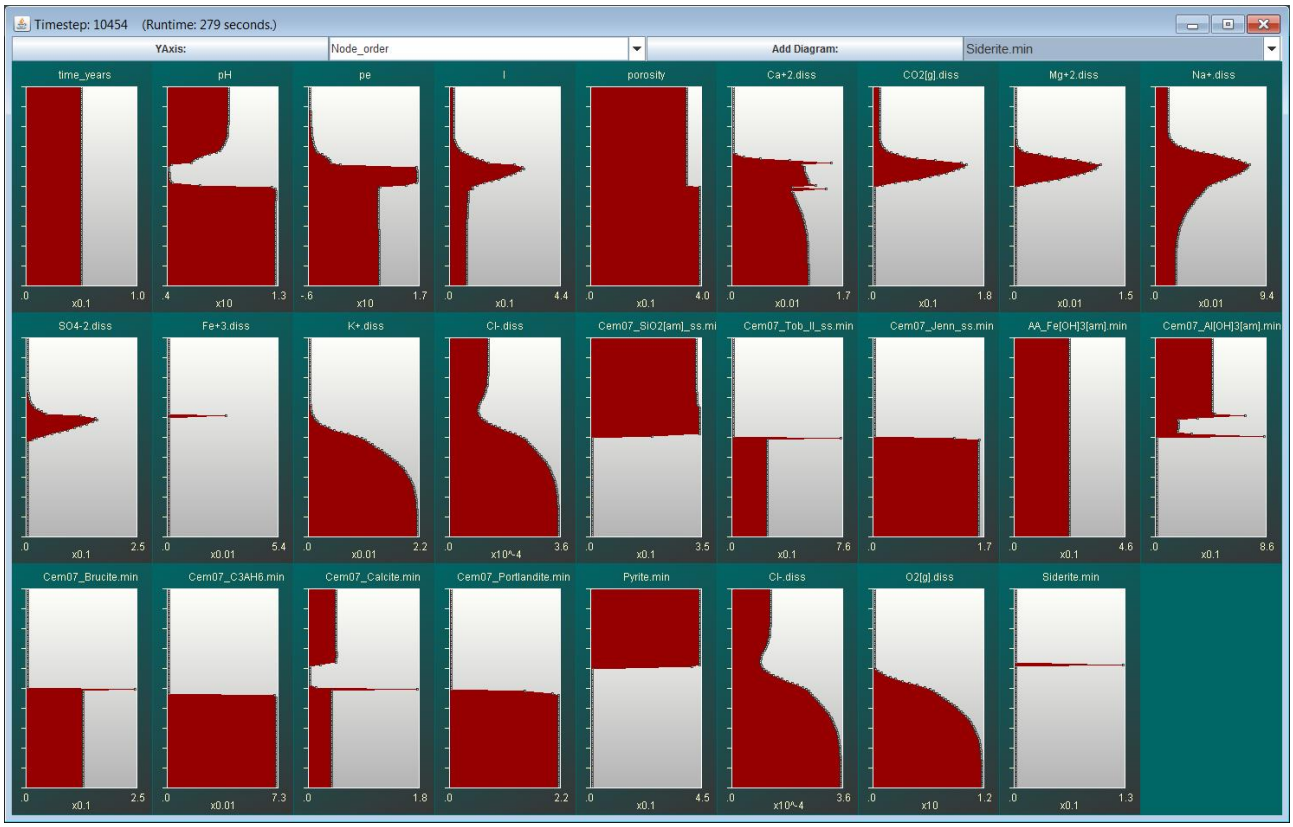

Figure 3. *Real time output of parameter profiles of the ORCHESTRA cement-clay interaction model.*

From the predicted profiles in Figure 3, after 35 days of simulation time, a number of observations could be made:

1) A developing drop in the pH of the clay layer, resulting from the oxidation and dissolution of pyrite. (The magnitude is determined by amounts of pyrite in the clay and oxygen concentration in the cementitious layer)
2) The dissolution of calcite in the clay zone (widening zone)
3) The precipitation of calcite in a narrow zone band in the cementitious zone
4) The precipitation of siderite in clay at some distance from clay concrete boundary
5) The precipitation of brucite at clay concrete boundary
6) The precipitation of tobermorite at clay concrete boundary

The distance of the affected zone in the cementitious layer is likely to remain small over the simulated time, as the buffer capacity of this zone is much larger than boom clay layer. This also depends on the porosities of the used materials under experimental conditions but the interaction zone is likely to be limited to several mm into the clay matrix.

9.4 REFERENCES

Rasouli, P., Steefel, C.I., Mayer, K.U. et al. (2015). Comput Geosci, 19: 523. doi:10.1007/s10596-015-9481-z.

Marty, N.C.M., Bildstein O., Blanc P., Claret F., Cochepin B., Gaucher E.C., Jacques D., Lartigue J., Liu S., Mayer K.U., Meeussen J.C.L., Munier I., Pointeau I., Su D., Steefel C.I. (2015). Benchmarks for multicomponent reactive transport across a cement/clay interface, Computational Geosciences, 19,635-653.

Steefel C.I., Appelo C.A.J., Arora B., Jacques D., Kalbacher T., Kolditz O., Lagneau V., Lichtner P.C., Mayer K.U., Meeussen J.C.L., Molins S., Moulton D., Shao H., Šimůnek J., Spycher N., Yabusaki S.B., Yeh G.T. (2015). Reactive transport codes for subsurface environmental simulation, Computational Geosciences, 19, 445-478.

Meeussen J.C.L. (2003). ORCHESTRA: An object-oriented framework for implementing chemical equilibrium models, Environmental Science & Technology, 37(6), 1175-1182.

10 SCK·CEN/ L. Yu, L. Lemmens, Q.T. Phung, J. Perko, D. Jacques, R. Patel* (Waste & Disposal Expert Group, Belgian Nuclear Research Centre, * now at PSI)

Abstract

Pore-scale models are an attractive way to evaluate the evolution of a porous structure during interaction with the environment and to estimate effective transport parameters. We evaluate the performance of different approaches to generate the microstructure. We report the evaluation a porous media reconstruction technique using SEM images to estimate the effective diffusion coefficient by comparison of an existing experiment. The 3D porous reconstruction technique gives values very close to the measured effective diffusivity. We applied the approach of generating a microstructure with a cement hydration model to the concrete used in the in-situ experiment (no data for validation are available yet). Lastly, we illustrate the framework of modelling geochemical alterations of the microstructure which will be used in further steps to model the experimental data (not available yet).

Keywords: Pore-scale modelling, diffusion coefficients

10.1 VALIDATION OF PORE SCALE MODELLING

The main objectives are to validate if a pore-scale modelling approach is able to predict macro-scale (continuum) transport properties using experimental information at the micro-scale and to apply a reactive coupled pore-scale model for simulating the spatial-temporal evolution of geochemical changes during the interaction of high pH-cementitious material and Boom Clay. The modelling results will be compared to experimental data. Microstructural information can be obtained in three ways: (i) using hydration model, (ii) derive 2D/3D microstructures based on 2D measurements (SEM), (iii) use 3D microstructures obtained by FIB-SEM. Experimental data used in this work are: (i) previously studies on cement conditions during leaching/carbonation (Phung et al. , 2015, 2016a), (ii) experimental laboratory studies on leaching and carbonation during interaction of cement and Boom Clay (WP1, Phung et al. (2016b)) , and (iii) characterisation of long-term interaction between concrete and Boom Clay on samples obtained from the underground research laboratory HADES (WP1, Phung et al. (2016b)).

Generation of 2D/3D microstructures

***Approach 1: Simulated using a cement hydration model*.** Virtual microstructures are generated with the hydration model CEMHYD3 (Bentz, 1994) similar to approaches described in Patel (2016).

Approach 2: Porous media reconstruction algorithm using SEM images. Using a porous media reconstruction algorithm has several advantages: (i) it offers the possibility to combine information from different imaging techniques and scales e.g. SEM and µCT, (ii) it allows for assessing uncertainty on the estimated effective properties based on the uncertainty on the structure of the porous media using multiple realizations, and (iii) it provides the opportunity to derive 3D models from a single 2D image. To reconstruct the cement paste, currently an in-house hierarchal porous media reconstruction algorithm based on simulated annealing is used – the reconstruction algorithm might be improved during further studies.

The reconstruction algorithm was trained using a 4 phase (pores, portlandite, clinker, C-S-H) 2D SEM image (Figure 1) with a resolution of 50 nm and a size of 96 x 128 mm.

The reconstruction algorithm simulates one phase after each other. To initialize the reconstruction process, the training image is therefore transformed into a binary image i.e. the first phase to simulate (e.g. clinker phase) and the background of the phases not simulated yet. In the next step, the algorithm determines the histogram of this binary image and initializes a reconstruction with the desired shape and the same histogram as the training image (Ti). Next the Ti and the reconstruction grid (Rg) are scanned in various direction and two spatial two- points correlation functions from Torquato (2013) are determined: (i) the two-point probability function, which describes the probability that two points separated by a specific distance lie in the same phase, and (ii) the lineal path function, which determines the probability that an entire line segment between two points belongs to one phase. Subsequently the misfit between the individual structural descriptors in Ti and the Rg is determined. In the so-called pixel switching phase, the algorithm will minimize the misfit between the structural descriptors. In this phase, always a pixel from currently simulated phase and the background in the Rg are exchanged. If this switching leads to a decrease in the structural descriptor misfit, the exchange is always excepted and the next points are exchanged. If the switch increases the misfit, the exchange is accepted with a given probability, this probability decreases as the number of pixel switching increases. The algorithm stays in the pixel switching phase until a predefined number of iterations or until the misfit drops under a predefined threshold. Now the simulation of the first phase is finished and the pixel of this phase are frozen and the next phase is simulated. To do so, the Ti is transformed in a ternary image (the first phase simulated, the current one and the background). The Rg is adapted by transforming pixels from the initial background in the Rg to the currently simulated phase so that the new Ti and Rg have the same histogram. Afterwards the structural descriptor for the currently simulated phase and the background are determined and the pixel switching phase stars again. The algorithm stays in this loop until all phases are simulated.

The results of such cement past reconstructions in 2D can be seen in Figure 1. We assumed an isotropic material for the 3D simulation. Accordingly, the structural descriptors for the third dimension could be predicted and used for the misfit determination. Figure 1 shows the reconstruction of an isotropic medium in 3 directions, where the continuity between the different slices is ensured.

Approach 3: Measured using FIB-SEM. This is not applied at this stage because the measurements of WP1 are not available yet.

Estimating effective properties – effective diffusion – using a pore-scale model

Simulation tool YANTRA (Patel et al., 2014). YANTRA is a flow and transport pore-scale modelling tool using lattice Boltzmann to solve the flow and transport equations. It can be coupled to iPhreeqc (Charlton and Parkhurst, 2011) or any other geochemical solver for reactive transport modelling. It can model processes in a multilevel porous media where part of the pore structure is described at a lower scale than the size of the voxel. This is called unresolved pore space and is treated through the application of effective (continuum) properties to these phases in the microstructure. Specific for cement systems, this technique is used to assign diffusive properties to the C-S-H phase. The C-S-H diffusivity is calculated with the model described in Patel et al. (2017a).

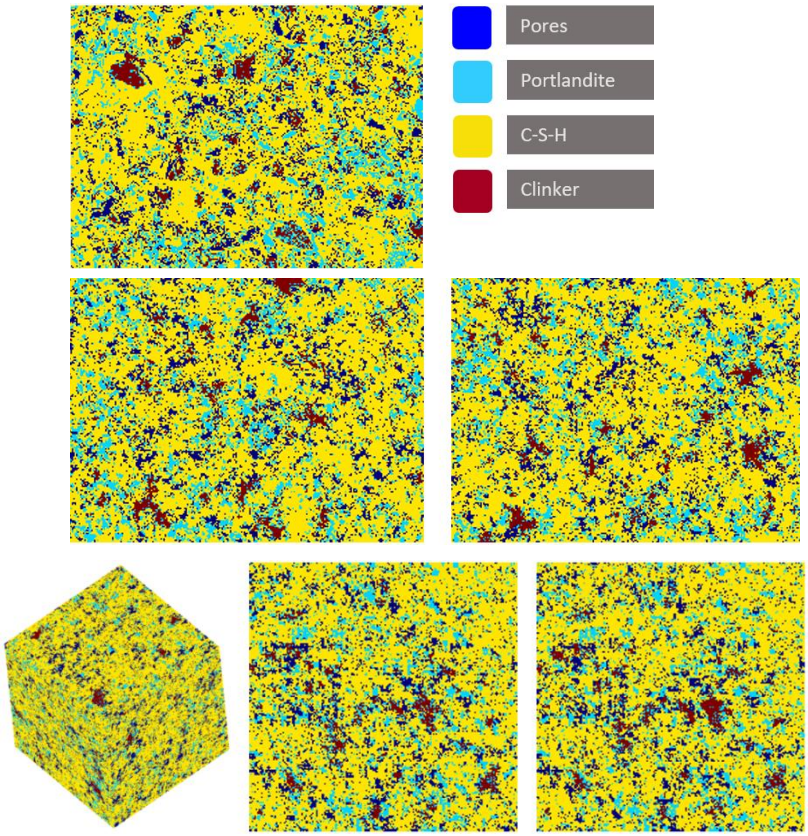

Figure 1. *(Top) Schematic SEM image used as a training image in the algorithm. (Middle) Two independent 2D reconstructions of the training image. (Bottom) 3D view of a reconstructed block using the 2D training image plus two consecutive slices of the Block in z direction to show that the continuity of the particles is also ensured in the z direction.*

Table 1. *Overview of simulation cases.*

	Experiments from Phung et al., 2015, 2016a		**Laboratory experiments in CEBAMA (Phung et al., 2016b, 'BF')**
	2D reconstruction	**3D reconstruction**	**CEMHYD3D**
Domain size (µm)	95	100	100
Resolution (µm)	1	1	1
Water/cement ratio	0.425	0.425	1.5
Hydration rate	0.83	0.83	0.75
Phase fraction			
C-S-H:	0.66	0.74	0.51
capillary pores	0.15	0.10	0.36
portlandite	0.15	0.11	0.11
clinkers	0.04	0.05	0.02
Property of CSH phase			
C-S-H porosity	0.35	0.38	0.78
C-S-H diffusivity	0.0024	0.0024	0.0664 (or typical value of 0.0025)
D_e/D_0*	0.0017 (x-direction) 0.0016 (y-direction)	0.0028	0.1652 (0.0823)

*D_e: the effective diffusion coefficient, D_0: the diffusion in capillary water.

Evaluation of the approach – experimental data of Phung et al. (2015, 2016a)

The experimental data is used to evaluate the porous media reconstruction algorithm as an input to estimate the effective diffusion coefficient using a pore-scale model. Both a 2D and 3D reconstruction are tested (respectively, case 1 and 2 in Table 1). Figure 2 summarizes the simulation results. The 2D pore structure gave slightly smaller values compared to the 3D pore structure. The latter compares very well with the measured values from Phung (2015) with a measured value of D_e/D_0 of 0.0032.

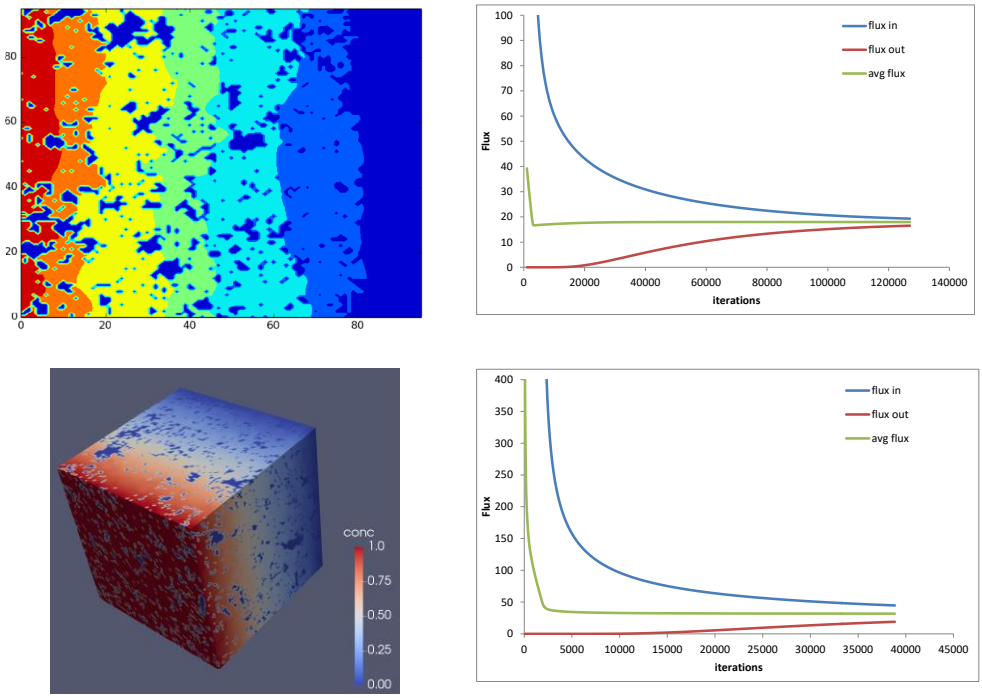

Figure 2. *(Top) Case 1 - (left) Steady-state concentration profile in x-direction, (right) in, out and average flux in the domain as a function of the number of iterations in x-direction. (Bottom) (left) Steady-state concentration distribution, (right) in, out and average flux in the domain as a function of number of iterations.*

Evaluation of the approach – Experimental data from WP1 (BF, Phung et al., 2016b)

Approach 1 is applied here. Data is not available yet for validation or to apply the other approaches (SEM and FIB SEMB images). Parameters used in the hydration model and the transport model are listed in Table 1. The CEMHYD3 hydration model gives a less heterogeneous porous media compared to the porous reconstruction approach based on SEM images (Figure 3 versus Figure 1). The high w/c ratio induces a high fraction of capillary pores, so as a high diffusion coefficient of CSH phase. In turn, this result in a much larger D_e/D_0 of 0.0664.

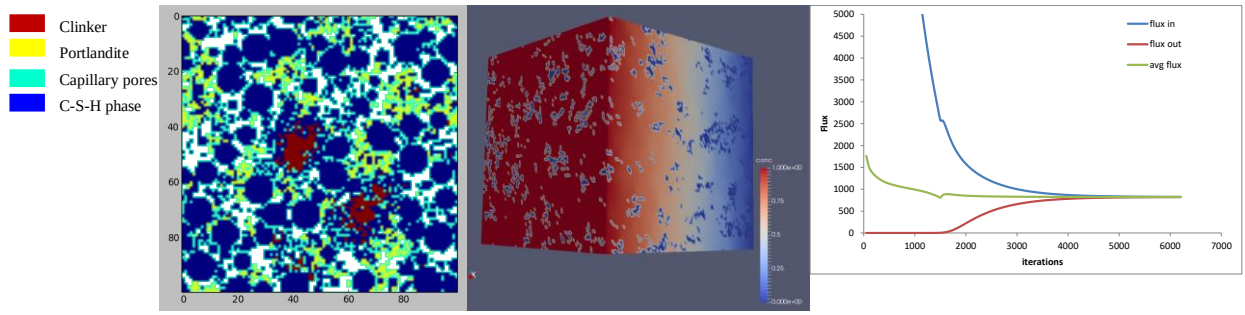

Figure 3. *Case 3 (left) microstructure at 50µm obtained by CEMHYD3D, (middle) Concentration distribution at steady-state, (left) in, out and average flux in the domain as a function of number of iterations.*

Estimating leaching – effective diffusion – using a pore-scale model

Simulation of leaching/carbonation of cement during interaction with other materials will be done by the geochemical solvers in YANTRA. The approach was tested by simulating leaching of a hardened cement paste using a microstructure obtained from hydration models (Patel et al., 2017b). Figure 4 shows some 3D pictures after 800s of leaching. Figure 5 shows some variables which potentially could be used to validate the pore-scale models.

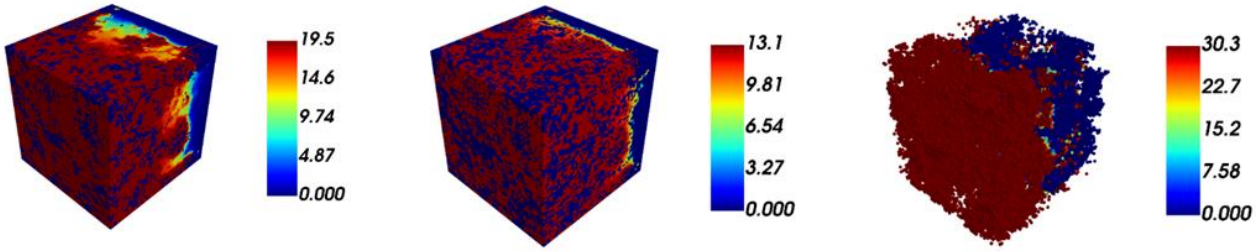

Figure 4. *Simulation of leaching of a hardened cement paste (w/c 0.4) using a microstructure generated with CEMHYD3. (left)Ca concentration in aqueous phase (mol/l), (middle) C-S-H phase (mol), (right) portlandite phase (mol).*

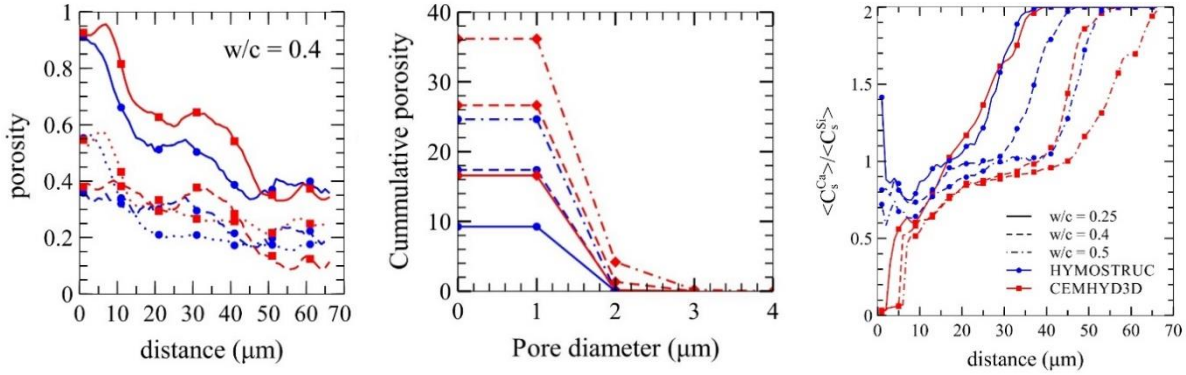

Figure 5. *Simulation results of leaching (left) porosity as a function of distance (blue: CEMHYD3D, red: HYMOSTRUC, solid: total porosity, dashed: capillary porosity, points: gel porosity), (middle) Pore size distribution (blue: t=0, red: t=800s, w/c see right figure), (right) Ca/Si ratio at the end of the simulation in planes perpendicular to the leaching direction.*

10.2 REFERENCES

Bentz, D.P. , Coveney, P.V., Garboczi, E.J.;, Kleyn, M.F., Stutzman, P.E. (1994). Cellular automaton simulations of cement hydration and microstructure development. Modelling and Simulation in Materials Science and Engineering, 2, 783-808.

Charlton, S.R., Parkhurst, D.L. (2011). Modules based on the geochemical model PHREEQC for use in scripting and programming languages. Computers & Geosciences, 37, 1653-1663.

Patel, R.A. (2016). Lattice Boltzmann method based framework for simulating physico-chemical processes in heterogenous porous media and its application to cement paste. PhD-thesis Department of Structural Engineering, Ghent university.

Patel, R., Perko, J., De Schutter, G., Van Breugel, K., Ye, G. (2014). A versatile pore-scale multicomponent reactive transport approach based on lattice Boltzmann method: Application to portlandite dissolution. Physics and Chemistry of the Earth, 70-71, 127-137.

Patel, R., Perko, J., Jacques, D., De Schutter, G., Ye, G., van Breugel, K. (2017a). Effective diffusivity of cement pastes from virtual microstructures: role of gel porosity and capillary pore percolation. Construction and Building Materials (under review).

Patel, R., Perko, J., Jacques, D., De Schutter, G., Ye, G., van Breugel, K. (2017b). A three-dimensional lattice Boltzmann method based reactive transport model to simulate changes in cement paste microstructure due to calcium leaching. Construction and Building Materials (under review).

Phung, Q.T. (2015). Effects of Carbonation and Calcium Leaching on Microstructure and Transport Properties of Cement Pastes PhD-thesis Department of Structural Engineering, Ghent University.

Phung, Q. T., Maes, N., Jacques, D., Bruneel, E., Van Driessche, I., Ye, G., De Schutter, G. (2015). Effect of limestone fillers on microstructure and permeability due to carbonation of cement pastes under controlled CO2 pressure conditions. Construction and Building Materials, 82, 376-390.

Phung, Q. T., Maes, N., Jacques, D., De Schutter, G., Ye, G. (2016a). Investigation of the changes in microstructure and transport properties of leached cement pastes accounting for mix composition. Cement and Concrete Research, 79, 217-234.

Phung, Q. T., Maes, N., Claret, F., Gaboreau, S., Leysen, J. (2016b). Methodology to study the changes in microstructure and transport properties of the Boom Clay - concrete interface. CEBAMA, Deliverable n°D4.08 - Draft of the 1st annual project workshop proceeding, 37-48.

Torquato, S. (2013). *Random heterogeneous materials: microstructure and macroscopic properties* (Vol. 16). Springer Science & Business Media.

14 UDC/ J. Samper, A. Mon, L. Montenegro, A. Naves, J. Fernández (UDC), J. Cuevas, R. Fernández (UAM), M.J. Turrero, E. Torres (CIEMAT)

Abstract

Coupled thermal (T), hydrodynamic (H) and chemical (C) models that account for soil mechanical (M) deformation have been performed to study and quantify the time evolution of the engineered barrier system (EBS) of a HLW repository. Here we present coupled THCM models of the heating and hydration tests (HB1 to HB6) performed by Ciemat and UAM on column tests containing OPC concrete in contact with compacted FEBEX bentonite which lasted from 0.5 to 11 years. The tests provide unique data on the interactions of concrete and bentonite under repository conditions and potential changes in bentonite and concrete properties. These tests were performed on columns heated at 100ºC at the bottom and hydrated at the top. The numerical models reproduce the general trends of the measured water content, porosity and temperature data and the experimental observations of mineral dissolution/precipitation.

Keywords: FEBEX bentonite, THCM model, OPC concrete

14.1 INTRODUCTION

The main objectives of UDC contribution to the CEBAMA Project include: 1) Improving THCM codes and models for the interactions of concrete and bentonite; 2) Performing THCM models of the heating and hydration HB tests; 3) Performing long-term predictions of the interactions of bentonite, concrete and clay rock; and 4) Contributing to the analysis of time scaling issues. Here we present coupled THCM models of the HB1, HB2, HB3, HB4, HB5 and HB6 tests (Turrero et al., 2011; Torres et al., 2013) and a detailed sensitivity analysis of the model of the HB4 test. The models were solved with the UDC code INVERSE-FADES-CORE. The first version of INVERSE-FADES-CORE was developed within the FEBEX I Project and was later improved within the FEBEX II, NFPRO, and PEBS Projects (Zheng et al., 2010; Samper et al., 2013; Mon, 2017).

14.2 HEATING AND HYDRATION TESTS

Several tests were performed to study the interactions of concrete and bentonite pore water at the conditions prevailing in the EBS during the early hydration stage (Turrero et al., 2011; Torres et al., 2013). The tests are denoted as HB ("*Hormigón -Bentonita*"). They were performed on medium-size cells containing a 7.15 cm thick bentonite sample in contact with a 3-cm thick piece of concrete. The concrete was sulphate-resistant ordinary Portland cement (CEM I-SR) following the recipe by CSIC-IETcc CEM-SR: 400 kg of cement, 911 kg of sand (0-5 mm), and 946 kg of aggregates (6-16 mm) with a w/c ratio of 0.45. Each cell was hydrated at a constant pressure at the top of the cell through the concrete while the temperature was maintained constant at 100ºC at the bottom of the cell (Figure 14.1). The HB tests provide data on the concrete and bentonite interface at several times. They were dismantled after 6, 12, 18, 54, and 80 months for the HB1 to the HB5 tests and 104 months for the HB6 test, which was dismantled within the CEBAMA Project. The experimental data from HB5 and HB6 tests are not yet available for modelling. The initial porosity of the bentonite is 0.4 and the initial water content is 13.3%, which corresponds to a saturation of 57% and a suction of $1.27 \cdot 10^8$ Pa. There were experimental problems to maintain a constant water injection pressure during the experiment. The cells were hydrated with a synthetic Spanish Reference Clay Porewater (Turrero et al., 2011; Torres et al., 2013).

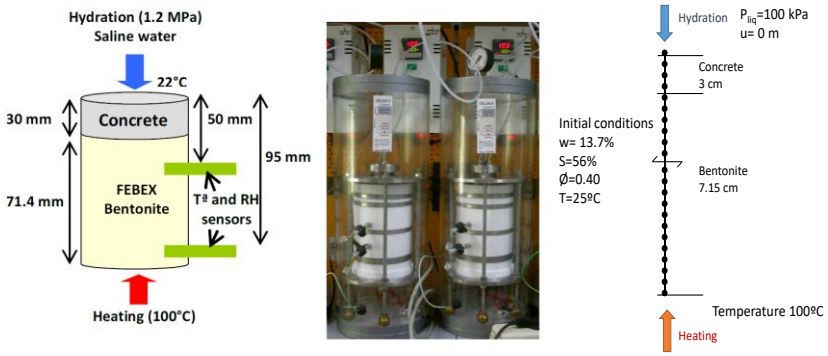

Figure 14.1. *Setup of the concrete-bentonite HB tests (left) and finite element mesh and boundary conditions for the numerical model (right).*

14.3 MODEL DESCRIPTION

HB1 to HB6 tests were modelled with a 1D grid (see Figure 14.1). Bentonite and concrete parameters were taken from the previous model of the HB4 test in Samper et al. (2013). The concrete has a porosity of 0.125 and a gravimetric water content of 2.2%. The initial temperature is 22ºC along the cell. Similar to previous THCM models of the FEBEX bentonite (Zheng et al., 2010), the initial total stress was assumed uniform, isotropic and equal to 250 kPa. Given the lack of reliable water injection pressure data, the injection liquid pressure was estimated from measured cumulative inflow data. Its value is equal to 100 kPa.

The initial composition of the OPC concrete porewater was derived from speciation runs performed with EQ3/6 (Wolery, 1992) by assuming that the concentration of dissolved Ca^{2+} is controlled by local chemical equilibrium with respect to portlandite, HCO_3^- concentration is at equilibrium with respect to calcite, Mg^{2+} concentration is derived from the equilibration with brucite, Al^{3+} is at equilibrium with ettringite and SiO_2(aq) is controlled by equilibrium with respect to C1.8SH. The initial mineral volume fractions in the concrete are: 7.4% for portlandite, 2.2% for ettringite, 14.6% for C1.8SH, 1% for brucite, 0.1% for calcite and 62.2% for quartz. Quartz is assumed to be nonreactive. The initial pore water composition of the FEBEX bentonite was taken from Fernández et al. (2004). The initial mineral volume fractions in the bentonite are: 0.36% for calcite, 0.08% for gypsum and 1.192% for cristobalite. The smectite was assumed to be not reactive. The model allows for the precipitation of the following secondary minerals: sepiolite, C0.8SH, anorthite and anhydrite. The dissolution/precipitation of portlandite, ettringite, C1.8SH, C0.8SH, quartz and cristobalite was simulated with the kinetic rate laws of Fernández et al. (2009).

14.4 MODEL RESULTS

THM results

The computed water content and porosity reproduce the general trends of the measured data at the end of the HB1 to HB 4 tests (see Figure 14.2). The concrete is fully saturated at 7 days and then, the bentonite hydrates at a very low rate through the concrete. Water content increases near the concrete and decreases near the heater due to the evaporation. The porosity increases in the bentonite near the concrete interface due to bentonite swelling. The model predictions of water content and porosity for the HB5 and HB6 tests are similar to those of the rest of the HB tests. The results of the HB1 to HB6 tests are similar because the water intake is fast in the first months and slows down after 10 months.

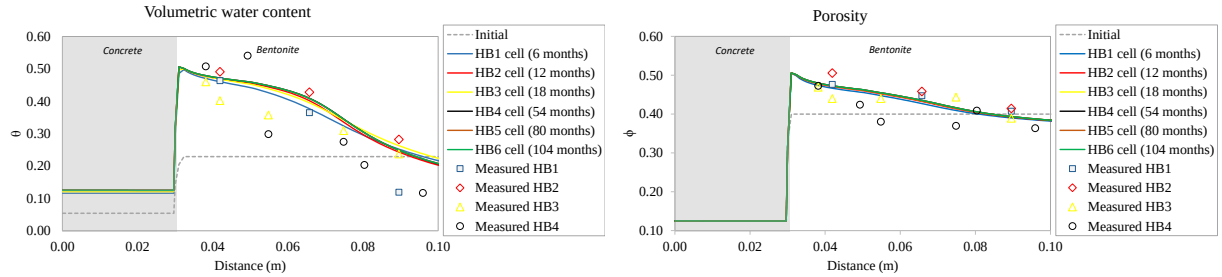

Figure 14.2. *Computed (lines) volumetric water content (left) and porosity (right) and measured data (symbols) for the HB1, HB2, HB3, HB4, HB5 and HB6 tests.*

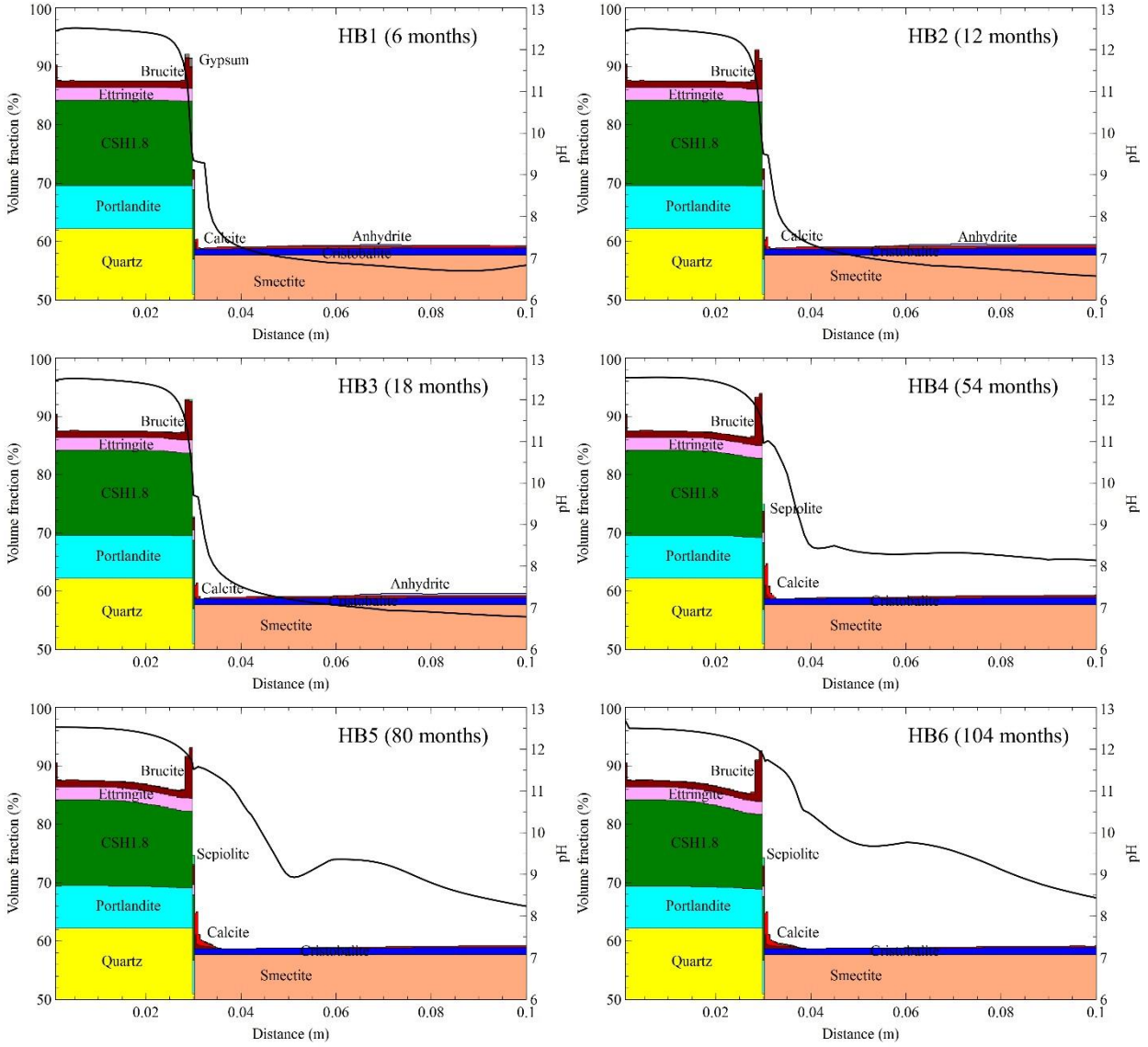

Figure 14.3. *Computed pH and mineral volume fractions for the HB1, HB2, HB3, HB4, HB5 and HB6 tests.*

Chemical results

Figure 14.3 shows the computed pH and the mineral volume fractions for the HB1 to HB6 tests. The main experimental observations on mineral phases at the end of the HB1, HB2, HB3 and HB4 tests are listed in Table 14.1. This table includes also a summary of the main trends of the computed mineral dissolution/precipitation for the HB1 to the HB6 tests.

A qualitative comparison of the computed values and the experimental mineral observations reveals that the numerical model captures the main trends of the experimental mineralogical observations. However, there are some discrepancies for ettringite and C-S-H precipitation. The numerical model predicts a precipitation of ettringite and C-S-H much smaller than the observed values. Model discrepancies could be caused by uncertainties in: 1) CSH, MSH and CASH phases; 2) Kinetic parameters (rate laws and specific surfaces); and 3) The secondary clay minerals. The porosity decreases in the bentonite/concrete interface and at the hydration boundary mainly due to brucite and calcite precipitation.

The computed mineral dissolution/precipitation concentrations in the HB5 and HB6 tests are similar to those of the rest of the HB tests. The penetration of the pH front into bentonite increases with time. The pH plume (pH > 9) penetrates 5.5 cm into the bentonite in the HB6 test. The diffusion of the alkaline plume is retarded by mineral precipitation in the bentonite near the concrete interface.

14.5 SENSITIVITY ANALYSIS OF THE MODEL OF THE HB4 TEST

Sensitivity analysis to the temperature

The base run model of the HB4 test is non-isothermal. The temperature is 100ºC at the heater and 25ºC at the hydration side. A sensitivity run was performed at a constant and uniform temperature of 25ºC. Figure 14.4 shows the computed cumulative precipitation of calcite and brucite for the base run and the sensitivity run. The model results for constant temperature show significant differences in the precipitation of calcite and brucite. The peaks of brucite and calcite precipitation for constant temperature are smaller than those of the base run. Moreover, the thickness of the bentonite zone where calcite and brucite precipitate in the constant temperature run is larger than that of the base run. Brucite precipitates in the concrete and in the bentonite in the base run while brucite precipitates only in the bentonite in the constant temperature run.

The reduction in porosity in the concrete near the bentonite interface and in the bentonite in the constant temperature run is smaller than that of the base run (Figure 14.5).

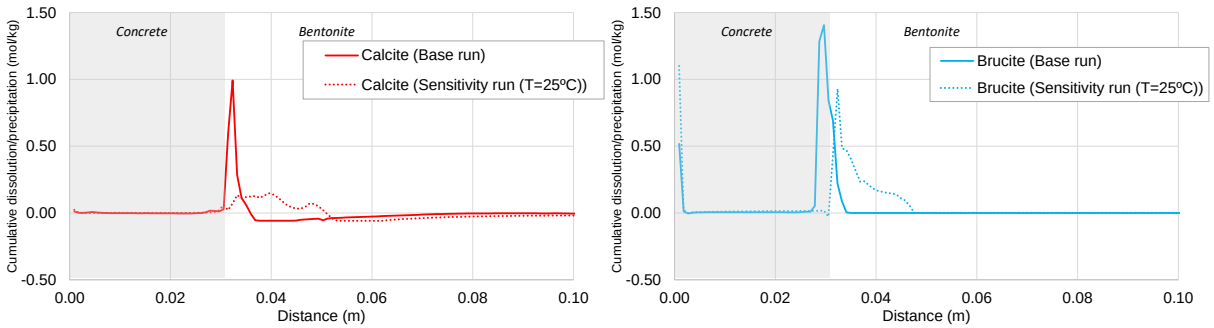

Figure 14.4. *Computed calcite (left) and brucite (right) precipitation/dissolution for the base run and the sensitivity run with a uniform temperature (25ºC) for the model of the HB4 test.*

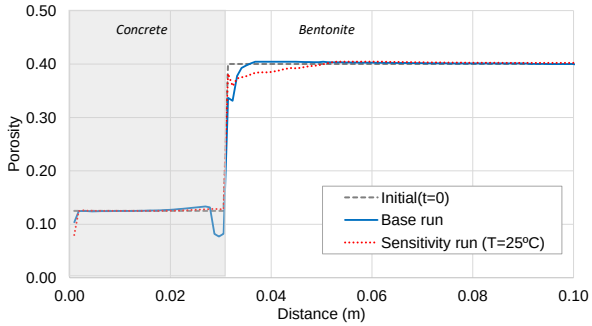

Figure 14.5. *Computed porosity for the base run and the sensitivity run with uniform temperature (25ºC) for the model of the HB4 test.*

Sensitivity analysis to mineral phases

Sensitivity runs were performed to investigate the sensitivity of model results to changes in the specific surfaces of kinetically-controlled minerals (portlandite and ettringite). Model results are sensitive to an increase of the specific surface of portlandite by a factor of 2 and an increase of the specific surface of ettringite by a factor of 10 (see Figure 14.6). The increase in the specific surface of portlandite leads to larger portlandite dissolution rates, larger calcite precipitation and larger pH in the bentonite. The increase of the specific surface of ettringite leads to more precipitation of ettringite in the mid upstream part of the concrete, more ettringite dissolution in the concrete near the bentonite interface and larger pH in the bentonite. On the other hand, model results are not sensitive to kinetic smectite dissolution and analcime precipitation at equilibrium. The model lacks sensitivity to the kinetic Mg-saponite precipitation (Figure 14.6). The smectite and Mg-saponite dissolution/precipitation was set with kinetic law taken from Mon et al. (2017) and the analcime precipitation was considered at equilibrium.

Sensitivity analysis to grid size

Grid size in the reference model is uniform and equal to 0.9 mm. Several sensitivity runs were performed in which the grid was refined in a 3 cm wide band around the concrete/bentonite interface. Grid sizes of 0.45 mm, 0.18 mm and 0.1 mm were considered in three simulation runs while the size of the rest of the elements was equal to 0.45 mm. Mineral precipitation increases at both sides of the concrete/bentonite interface when the grid size is reduced (Figure 14.6). The calculated porosity in the concrete near the bentonite interface decreases drastically, reaching pore clogging for grid sizes smaller than 0.18 mm.

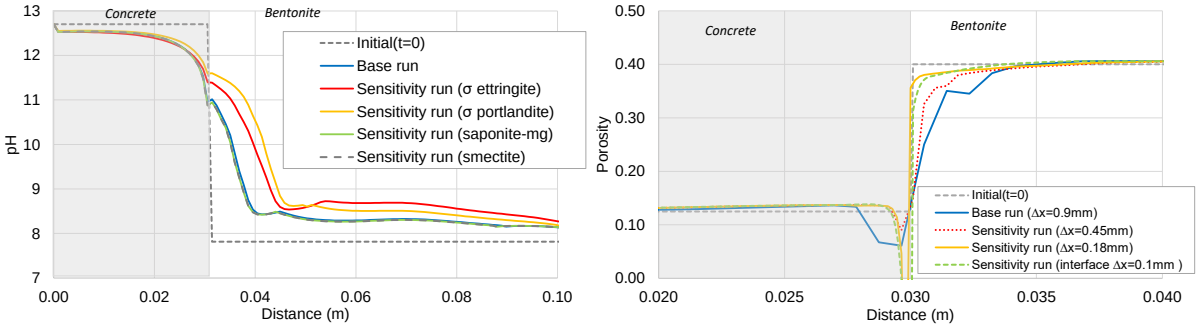

Figure 14.6. *Model of the HB4 test: Sensitivity of the computed pH to changes in the mineral parameters (left) and sensitivity of the computed porosity to changes in the grid size (right).*

14.6 CONCLUSIONS AND FUTURE WORK

Coupled THCM models of the HB1, HB2, HB3, HB4, HB5 and HB6 tests have been presented. Model results reproduce the general trends of the measured water content, porosity, and temperature and the observed patterns of mineral phases for the HB1 to HB4 tests. The predictions of the HB5 and HB6 tests show similar trends to those of the rest of the tests.

The thickness of the bentonite zone where calcite and brucite precipitate in the constant temperature run is larger than that of the base run. While brucite precipitates in the concrete and in the bentonite in the base run, this mineral precipitates only in the bentonite in the constant temperature run. The reduction in porosity in the concrete near the bentonite interface and in the bentonite in the constant temperature run is smaller than that of the base run. Model results are sensitive to the increase of the specific surfaces of portlandite and ettringite. On the other hand, model results are not sensitive to kinetic smectite dissolution, analcime precipitation at equilibrium and kinetic Mg-saponite precipitation. Mineral precipitation increases at both sides of the concrete/bentonite interface when the grid size is reduced. The calculated porosity in the concrete near the bentonite interface decreases drastically, reaching pore clogging for grid sizes smaller than 0.18 mm. The THCM models of the HB tests could be improved by: 1) Considering additional C-S-H and M-S-H phases; 2) Deriving optimum kinetic parameters and 3) Accounting for the feedback effect of the changes in porosity.

14.7 REFERENCES

Bentz, D.P. (2005). CEMHYD3D: A three-dimensional cement hydration and microstructure development modeling package. Version 3.0.

Fernández A.M., Bayens B., Bradbury M. and Rivas P. (2004). Analysis of pore water chemical composition of a Spanish compacted bentonite used in an engineered barrier. Phys. Chem Earth (29), 105-118.

Fernández, R., Cuevas, J. and. Mäder, U. K, (2009). Modelling concrete interaction with a bentonite barrier. Eur. J. Mineral., 21, 177-191.

Mon, A, 2017. Coupled thermo-hydro-chemical-mechanical models for the bentonite barrier in a radioactive waste repository. Ph. D. Dissertation. Universidad de A Coruña, Spain.

Mon, A., J. Samper, L. Montenegro, A. Naves, J. Fernández, (2017). Long-term non-isothermal reactive transport model of compacted bentonite, concrete and corrosion products in a HLW repository in clay. Journal of Contaminant Hydrology, 197, 1-16.

Samper J., Mon A., Montenegro L., Pisani B. and Naves A. (2013). Report on testing multiple-continua THCM models with laboratory and large-scale tests. Deliverable 3.4-1 of the PEBS Project.

Torres E., Turrero M.J., Escribano A., Martín P.L. (2013). Geochemical interactions at the concrete-bentontie interface of column experiments. Deliverable 2.3-6-1 of PEBS Project.

Turrero M. J., Villar M. V., Torres E., Escribano A., Cuevas J., Fernández R., Ruiz A. I., Vigil de la Villa R., del Soto I. (2011). Laboratory tests at the interfaces, Final results of the dismantling of the tests FB3 and HB4. Deliverable 2.3-3-1 of PEBS Project.

Wollery T.J. (1992). EQ3/3. A software package for geochemical modeling of aqueous system: package overview and installation guide version 7.0. UCRL-MA-110662-PT-I, Lawrence Livermore National Laboratory, Livermore, California.

Zheng L., Samper J., Montenegro L. and Fernández A.M. (2010). A coupled model of heating and hydration laboratory experiment in unsaturated compacted FEBEX bentonite. Journal of hydrology 386, 80-94.

Table 14.1. *Qualitative comparison of laboratory and model results for mineral reactions.*

	HB1		HB2		HB3		HB4		HB5	HB6
	Laboratory observations	**Model results**	**Laboratory observations**	**Model results**	**Laboratory observations**	**Model results**	**Laboratory observations**	**Model results**	**Model results**	**Model results**
Concrete (Hydration)	**Portlandite** dissolution	√	**Portlandite** dissolution	√	**Portlandite** dissolution	√			**Portlandite** dissolution	**Portlandite** dissolution
	Calcite precipitation	√	**Calcite** precipitation	√	**Calcite** precipitation	√	**Calcite** precipitation	√	**Calcite** precipitation	**Calcite** precipitation
	Brucite precipitation	√	**Brucite** precipitation	√	**Brucite** precipitation	√	**Brucite** precipitation	√	**Brucite** precipitation	**Brucite** precipitation
Concrete (30 mm)	**Portlandite** precipitation	√	**Portlandite** precipitation	√	**Portlandite** precipitation	√	**Portlandite** dissolution	√	**Portlandite** dissolution	**Portlandite** dissolution
		√	**Calcite** precipitation in concrete	√	**Calcite** precipitation in concrete	√	**Calcite** precipitation in concrete	√	**Calcite** precipitation in concrete	**Calcite** precipitation in concrete
	CSH gels precipitation	~	**CSH gels** precipitation	~	**CSH gels** precipitation	~	**CSH gels** precipitation	~	**Some CSH** precipitation	**Some CSH** precipitation
	Quartz precipitation	*N*	**Quartz** precipitation	*N*	**Quartz** precipitation	*N*				
	MSH precipitation	√	**MSH** precipitation	√	**MSH** precipitation	√				
							Ettringite precipitation	*N*	**No Ettringite** precipitation	**No Ettringite** precipitation
					Gypsum and **thaumasite** precipitation	√				
	Zeolites precipitation	Not considered	**Halite** and **K-feldespar** precipitation	Not considered	**Vaterite** and **aragonite** precipitation	Not considered				
Concrete/ bentonite interface (some mm)	**Brucite** precipitation	√	**Brucite** precipitation	√	**Brucite** precipitation	√	**MSH** precipitation	√	**MSH** precipitation	**MSH** precipitation
	Portlandite precipitation	*N*	**Portlandite** precipitation	*N*	**Portlandite** precipitation	*N*				
	Calcite precipitation	√	**Calcite** precipitation	√	**Calcite** precipitation	√	**Calcite** precipitation	√	**Calcite** precipitation	**Calcite** precipitation
	CSH gels (tobermorite and jennite type) precipitation	*N*	**CSH gels (tobermorite and jennite type)** precipitation	*N*	**CSH gels (tobermorite** and **jennite type)** precipitation	*N*	**CSH gels (0.8)** precipitation	*N*	**No CSH** precipitation	**No CSH** precipitation
			Ettringite precipitation	*N*	**Ettringite** precipitation	*N*	**No Ettringite** precipitation	√	**No Ettringite** precipitation	**No Ettringite** precipitation
			Gypsum precipitation	√	**Gypsum** precipitation	√				
					Quartz dissolution	√				
	Smectite alteration not observed	Not considered	**Smectite alteration** (brucite saponite-smectite mixed phase")	Not considered	**Smectite alteration** (brucite saponite-smectite mixed phase") **Saponite** formation	Not considered Not considered				
									Brucite precipitation	**Brucite** precipitation
Bentonite	Unaltered bentonite mineralogy	~	Unaltered bentonite mineralogy	~	Unaltered bentonite mineralogy	~	**Calcite** dissolution	√		
							Gypsum and **chloride** precipitation	√		

16 CTU/ T. Rosendorf, D. Vopálka (CTU), R. Červinka (ÚJV)

Abstract

The determination of changes in tritium diffusivities on samples of hardened OPC that interacted with groundwater (9 / 18 / 27 months) at two different temperatures (10 °C and 95 °C), belongs to the goals of Czech laboratory program within WP1. The first through diffusion experiment dataset after 9 months of interaction was offered by UJV partner. It showed that the increase of a temperature negatively influenced diffusion properties of tritium on hardened OPC samples (especially the increase of pore diffusion coefficient D_p). The second part of the contribution deals with an input preparation for common modeling task within WP3. An illustrative parametric study was performed with the aim to show the role of different D_p values for D_e keeping constant in modeling of diffusion transport in field conditions of double-barrier layer.

Keywords: cement, OPC, diffusion, GoldSim, groundwater, tritium, double-barrier, layer.

16.1 METHODOLOGY: EXPERIMENTAL & MODELING INPUT

The determination of changes in tritium diffusivities on samples of hardened OPC that interacted with underground water (GW Josef), belongs to the goals of Czech laboratory program within WP1. The interaction experiments are designed for 9, 18 and 27 months under two different temperatures: 10 °C corresponds to in-situ conditions of Josef Underground Facility and 95 °C as extreme temperature (Večerník et al., 2016). For an evaluation, we obtained results of the set of 1D-through diffusion experiments on samples of hardened OPC that interacted with groundwater for 9 months. Each through-diffusion experiment was described by three datasets, the time evolution of relative volume activity a/a_0 of tritium in the inlet and outlet reservoirs, and the concentration profile of tritium in the porous layer of hardened cement paste. These datasets enabled us to apply our method of evaluation prepared in the GoldSim environment (Vopálka, 2016).

Experimental setup and modeling conditions are schematically described as follows:

- WP1 Czech program – hardened OPC mixture: CEM II A-S 42.5R + H_2O (w = 0.45), hydratation 28 days.
- Hardened OPC cylinders: ca 50 mm diameter, ca 8.3 – 8.4 mm length.
- Diffusion cells identification, samples after 9 months of interaction:
  - Vessel 11: hydrated OPC and GW Josef at 95 °C, cells A, B, C: series labelled as "V11_OPC95_9M_dif3H",
  - Vessel 14: hydrated OPC and GW Josef at 10 °C, cells D, E, F: series labelled as "V14_OPC10_9M_dif3H".
- 1D-through diffusion experiment: non-constant concentration of tracer (^3H) in the reservoirs in diffusion cells without filters.
- Duration of diffusion experiments: 62 – 111 days.
- Inlet and outlet reservoirs volumes: $V = 57 – 60$ cm^3.
- Reference diffusivity of HTO in water: $D_w = 2.44\times10^{-9}$ m$^2\cdot$s^{-1}, Berne et al. (2010),
- Pore diffusion coefficient D_p ($=D_w \cdot G$) and effective diffusivity D_e ($= D_p \cdot \varepsilon$) were evaluated on the base of geometrical factor G and porosity ε fitting,
- For HTO as a conservative tracer no sorption was expected ($K_d = 0$ l$\cdot$g^{-1}, then capacity factor $\alpha = \varepsilon$).

16.2 RESULTS & INTERPRETATION OF WP1 DATASET FROM DIFFUSION EXPERIMENTS OF ^{3}H

Diffusion module prepared in the GoldSim environment can model and evaluate diffusion experiments with variable concentration (radioactivity) of radiotracer in both reservoirs, unlike in the standard analytical solution (the time-lag method) that is limited to five or less percent change of the concentration from initial conditions. Furthermore, the use of our module is not limited to experiments that reach steady state, characterized by a constant mass flow in and out the studied layer, but also for experiments terminated during the transient regime. Therefore, this module is more complex and precise in the evaluation of through diffusion experiments. OPC samples in diffusion cells A – F after nine months of interaction with GW Josef at two different temperatures (10 °C, 95 °C) are described in Table 16.1.

Table 16.1. *Basic information about OPC samples in diffusion cell A – F, where L is length, d is diameter of sample and V is volume of inlet and outlet reservoir.*

	cell A	**cell B**	**cell C**	**cell D**	**cell E**	**cell F**
VESSEL	11	11	11	14	14	14
DURATION [months]	9	9	9	9	9	9
TEMPERATURE	95 °C	95 °C	95 °C	10 °C	10 °C	10 °C
***L* [mm]**	8.37	8.32	8.25	8.30	8.29	8.24
***d* [mm]**	50.30	50.38	50.40	50.35	50.37	50.38
V_{in} [mL]	58.0	57.0	57.0	57.5	58.0	58.0
V_{out} [mL]	57.5	57.0	57.0	58.0	58.0	57.5
DIFF. EXP. DURATION [d]	62	62	111	111	62	111

The experimental datasets were fitted in the GoldSim environment with the aim to obtain characteristic diffusion coefficients. Comparisons of experimental data with fitted curves are shown in Figures 16.1 – 16.2 (for cells A – C, 95 °C) and Figures 16.3 – 16.4 (for cells D – F, 10 °C). Evaluation of D_p and D_e is shown in Table 2.

These results have shown that diffusion through samples that were under temperature load (95 °C) for 9 months was faster with significant increase of D_p (approx. one order of magnitude) in the comparison with samples under ambient temperature (10 °C). Less significant difference was observed in porosity (0.43 – 0.46 for cells D – F, 10 °C; 0.44 – 0.54 for cells A – C, 95 °C) evolution due to the fact that more mass from OPC samples was dissolved. From this comparison, it can be concluded that chemical processes caused by long term heating led to less tortuous diffusion pathway (larger *G* values).

These results show that thermal load has a high importance on stability of OPC samples, the raise of diffusion coefficient D_p is significant. This finding should be taken into account in the common modeling task in WP3, in which porosity development (that influences development of D_e) is currently considered as one of the most important changes during the long-term alteration of cement and clay phases. Ongoing ^{36}Cl through diffusion experiments (where the sorption process is considered) on the OPC affected by same thermal loads in UJV will outline how effective diffusion coefficient D_e develops for a non-conservative tracer.

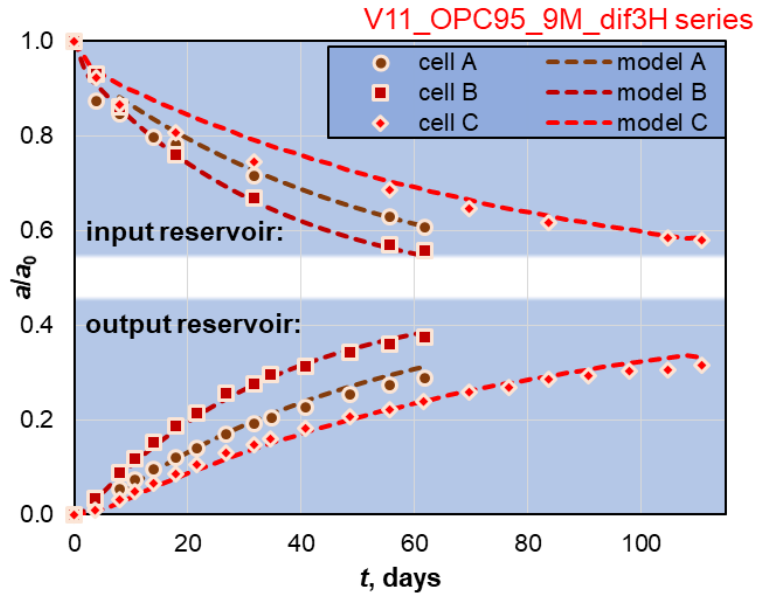

Figure 16.1. *The time evolution of the relative volume activity of ^{3}H with model fit in both reservoirs (cells A – C, 95 °C).*

Table 16.2. *Evaluation of diffusion coefficients in both series (A – C: 95 °C) and (D – F: 10 °C).*

	cell A	**cell B**	**cell C**	**cell D**	**cell E**	**cell F**
$D_p \cdot 10^{11}$ [m^2·s^{-1}]	4.9 ± 1.2	9.3 ± 0.9	3.7 ± 0.5	0.63 ± 0.25	0.56 ± 0.06	0.56 ± 0.28
$D_e \cdot 10^{11}$ [m^2·s^{-1}]	2.6 ± 0.7	4.1 ± 0.6	1.8 ± 0.3	0.29 ± 0.12	0.24 ± 0.03	0.25 ± 0.13

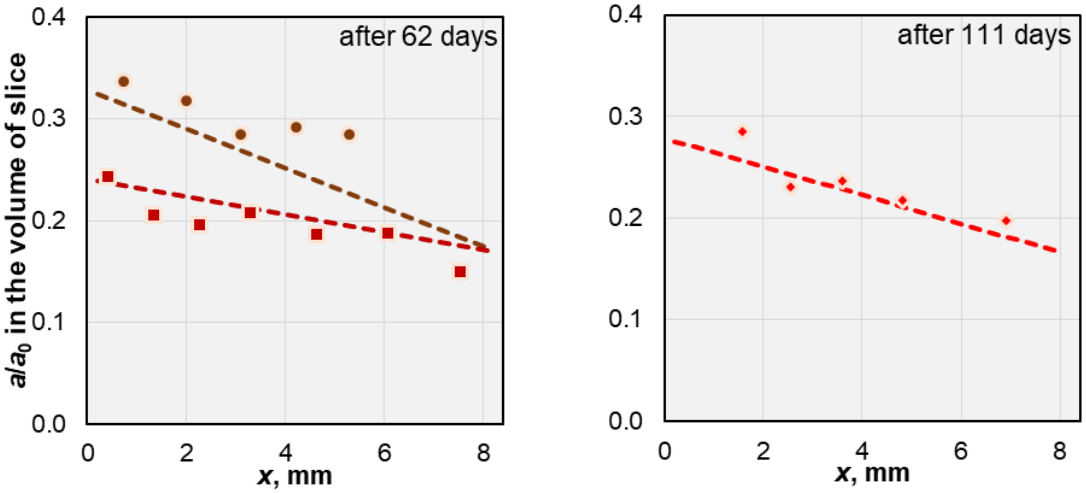

Figure 16.2. *The relative volume activity of ^{3}H in the profile of the OPC with model fit (cells A – C, 95 °C), for legend see Figure 1.*

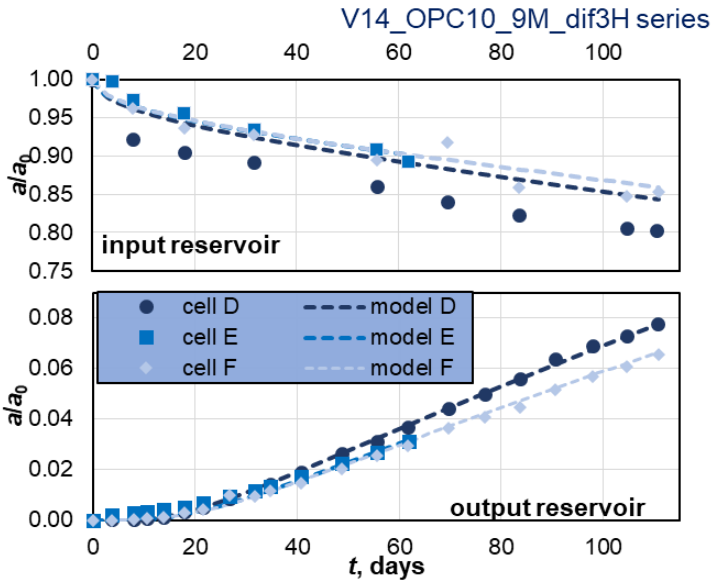

Figure 16.3. *The time evolution of the relative volume activity of ^{3}H with model fit in both reservoirs (cells D – F, 10 °C).*

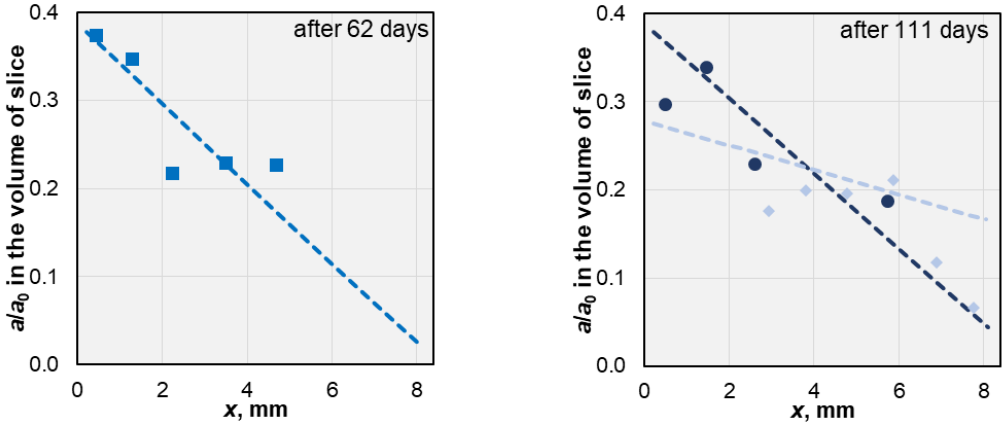

Figure 16.4. *The relative volume activity of ^{3}H in the profile of the OPC with model fit (cells D – F, 10 °C), for legend see Figure 16.4.*

16.3 MODELING OF DIFFUSION ON DOUBLE-BARRIER LAYER: A PREPARATION FOR COMMON MODELING TASK

Diffusion module for system of barrier interfaces in the environment of GoldSim was developed for modeling and evaluating diffusion experiments through two and more layers of materials, each characterized by the length, diameter, density, porosity, geometrical factor, and sorption characteristics (K_d, parameters of Langmuir and Freundlich isotherms) in Czech national program (SÚRAO). This model was presented and experimentally confirmed by evaluation of a set of HTO diffusion on the bentonite and hardened cement OPC interface (Rosendorf et al., 2017).

This module could be suitable also for the modeling within CEBAMA WP3 Modeling Task (diffusion of Ra or conservative tracer on sandwich of CEBAMA Low-pH reference mix and Callovo Oxfordian Clay). A disadvantage of this module lies in the absence of the time evolution of barriers characteristics, through which the diffusion transport is modeled (e.g. sorption parameters, porosity and tortuosity). However, it offers a useful tool for an assessment of diffusion in porous layers of barrier materials.

An illustrative parametric study was performed with the aim to show the possibility of the model to give information about the role of different parameters in modeling of diffusion transport in field conditions. In this study, it was supposed that the first layer, that is in connection with the source of a conservative tracer with half-life time of 1000 years (Layer A) is less permeable than the second layer (Layer B), on the outer boundary of which the concentration of studied tracer equals zero. Layers and boundary conditions of the systems were described as follows:

- Source: inconstant concentration of a tracer with half-live of 1000 years (decreases due to the diffusion into the first porous layer), initial mass of 10 mol in the inlet reservoir of volume 1 L.
- Outlet: volume 1000 L (→ constant concentration $c \sim 0$ mol·l^{-1}).
- Layer A: cylinder (1 m in diameter, 1 m in length, grid size 5 cm), no sorption sites, $D_p = (0.5 / 1 / 2) \cdot 10^{-12}$ m^2·s^{-1}, $D_e = 10^{-13}$ m^2·s^{-1}.
- Layer B: cylinder (1 m in diameter, 30 m in length, grid size 1.5 m), no sorption sites, $D_p = (1 / 2 / 5) \cdot 10^{-10}$ m^2·s^{-1}, $D_e = 10^{-11}$ m^2·s^{-1}.
- Time: 365 000 days, time-step: 36.5 days.
- Monitored concentration of tracer in the layer (mol in the volume of the grid / slice).

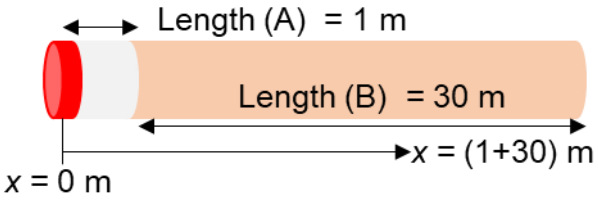

Figure 16.5. *Geometry conditions considered in the model.*

Results of modeling of concentration profiles in subsequent layers after 365 000 days for different characteristics of both layers (see Table 16.3) are presented in Figure 16.6.
WP1 and WP2 did not offer retention properties of Radium on the low-pH cement reference mix design. Thus, Radium is considered as a conservative tracer and therefore the models are simplified. If the change in the mentioned issue occurs, it will be necessary to take into account sorption properties of the tracer on the matter.

Table 16.3. *Parameters of nine models of two layer of barrier materials.*

layer		model 1	model 2	model 3	model 4	model 5	model 6	model 7	model 8	model 9
A	D_p [m^2·s^{-1}] ·10^{12}	2.0	1.0	0.5	2.0	1.0	0.5	2.0	1.0	0.5
A	D_e [m^2·s^{-1}] ·10^{13}	1.0	1.0	1.0	1.0	1.0	1.0	1.0	1.0	1.0
B	D_p [m^2·s^{-1}] ·10^{10}	2.0	2.0	2.0	1.0	1.0	1.0	0.5	0.5	0.5
B	D_e [m^2·s^{-1}] ·10^{11}	2.0	2.0	2.0	2.0	2.0	2.0	2.0	2.0	2.0

Models in Figure 16.6 show, how the D_p is crucial for the description of the system at constant D_e in both layers during the diffusion of a conservative tracer, therefore its evolution (as it was observed in real diffusion experiment in the previous chapter) should be taken into account in modeling of diffusion transport in Modeling Task.

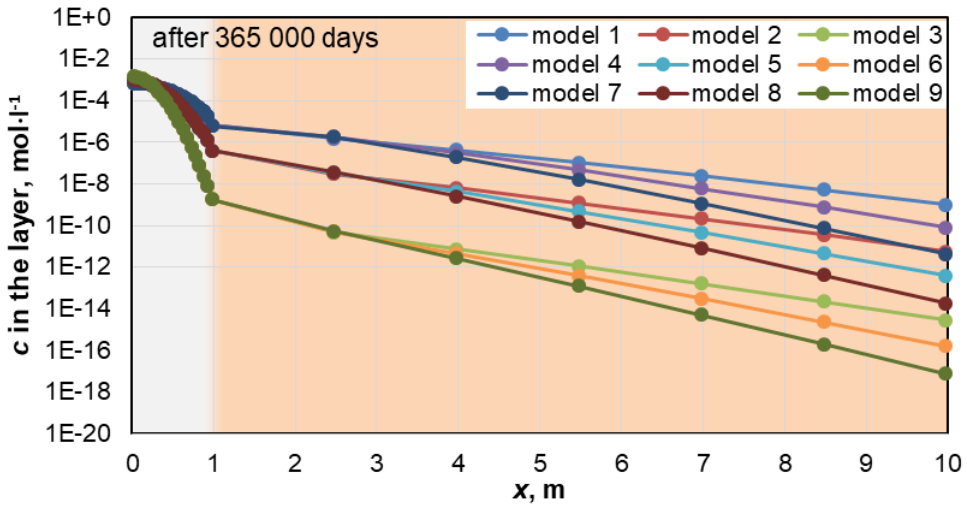

Figure 16.6. *Concentration of a conservative tracer in the layer of two barrier materials for nine models.*

16.4 REFERENCES

Berne P., Bachaud P., Fleury M. (2010). Diffusion Properties of Carbonated Caprocks from the Paris Basin Oil & Gas Science and Technology – Rev. IFP, Vol. 65, No. 3, pp. 473-484.

Rosendorf T., Hofmanová E., Vopálka D., Vetešník A., Večerník P., Červinka R. (2017). Diffusion experiments on bentonite/cement interface: development of methodology and evaluation. Migration 2017: Booklet of abstracts.

Večerník, P., Hausmannová, L., Červinka, R., Vašíček, R., Roll, M., Hloušek, J., Havlová, V. (2016). Interaction between cement and Czech bentonite under temperature load and in in-situ conditions: an overview of experimental program. Deliverable n° D4.08, CEBAMA: Draft of the 1st Annual Project Workshop Proceeding.

Vopálka, D. (2016). Czech Technical Univ. (CTU), Dep. Nuclear Chemistry (DNC) – modeling approach. Deliverable n° D3.02, CEBAMA: Review and definition of modeling approaches: scale of analysis, physico-chemical processes, software, HPC resources.

18 VTT/ T. Vehmas, A. Itälä

Abstract

The report describes progress made at VTT during the first 28-months of the four-year project. The on-going studies must be completed before the prediction of Portland cement based materials dissolution in deep geological nuclear waste repository is possible. Any single method is not able to forecast the cementitious materials behaviour, but the combination of experimental research and modelling is able to give boundary values for the cementitious materials dissolution in various scenarios.

Keywords: low-pH concrete, bentonite, modelling, groundwater

18.1 INTRODUCTION

Cementitious materials' pore solution has a naturally high pH of 13–14. Bentonite backfill and buffer properties are potentially altered due to high -pH leachate interaction from plug materials. Some of the nuclear waste managing organizations, such as Posiva (Finland), SKB (Sweden) and NUMO (Japan), have targeted a pH limit ≤11 for cementitious leachates. It has been suggested that more natural pH limit would be pH ≤10, as silicates aqueous behaviour changes. In pH <10, silicates are in neutral $SiO_2(aq)$ form in solution whereas in pH > 10 silicates dissociates to charged species $HSiO_3^-$. Correspondingly, the solubility of quartz increases by three orders of magnitude compared to the pH range 1–10 (Savage, 2007).

18.2 MATERIALS RELATED TO MODELLING

The highest tolerable pH of the leachate is 10 or 11 in the bentonite system. Otherwise the long-term stability of the engineered barrier system might be endangered. Mix designs having a leachate pH lower than natural pH of 13–14 have been formulated (Cau dit Coumes et al., 2006; Holt et al., 2014; Vogt et al., 2009; Martino et al., 2011; Holt et al., 2016). The low-pH mix designs consist of low alkaline Portland cements mixed with large amounts of pozzolanic materials. Pozzolanic materials are known to react with the hydration products that control the pH of the cementitious materials pore solution. Low-pH materials are still highly basic but the pH value is significantly lower than in traditional Portland cements.

The materials used to study low-pH concretes in repository environment were:

1. Ordinary Portland cement from Degerhamn manufactured by Cementa Ab.
2. Granulated silica fume (Parmix supplied by Finnsementti Oy)
3. Blast furnace slag was from Finnsementti Oy
4. Fly ash was from Denmark by E-mineral.
5. Quartz filler purchased from Silbeco Nordic
6. Concrete samples were manufactured using aggregates from ONKALO provided by Rudus Oy.
7. 3 different water compositions (ion-exchanged, saline bentonite porewater and simulated saline groundwater from ONKALO)

18.3 MODELLING

Modelling of EU Dopas samples

Thermodynamic modelling of EU Dopas experiments (Holt et al., 2016) was performed by using Gibbs energy minimization simulation method for calculating chemical equilibria in the experimental system. The software used was GEMS- Selektor v.3, developed by Paul Scherrer Institut. Suppelementary database CEMDATA14 was used for cementitious materials together with PSI-Nagra database. GEMS –Selektor software and CEMDATA14 –database have been widely used in cement and concrete research. GEMS-Selektor was chosen at this phase of the project because CEMDATA 14 database was already built-in the modelling software.

Pore solution pH of various CaO/SiO2 –ratio concretes were determined. Three water types were used. Ion exchanged water represents the pore solution pH, whereas saline groundwater sample represents the pH in the vicinity of the concrete structure when the concrete is exposed to the groundwater. Saline bentonite porewater represents the situation in which the groundwater composition is in equilibrium with the bentonite materials. Modelling of the concretes was performed by adding the exact experimental compositions of the used cement together with the used solutions to the model and thus modelling the pore solution compositions. Results of pore solution pH are presented in Figure 18.1.

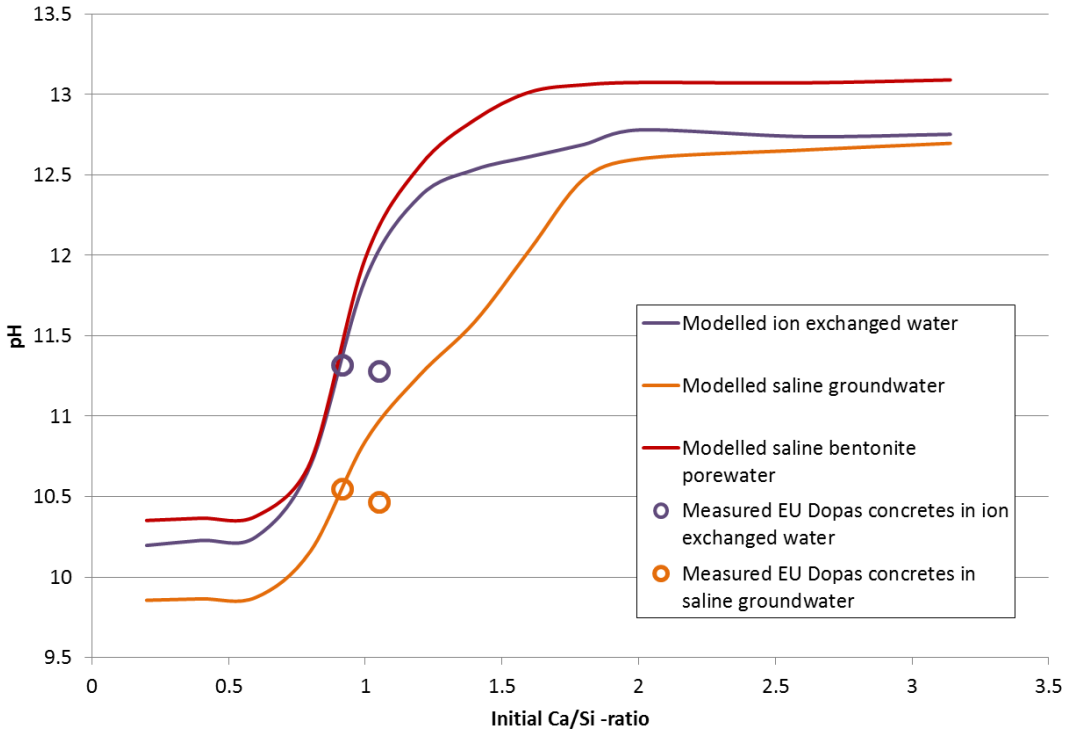

***Figure 18.1**. Experimental and modelled pore solution pH of accelerated paste Samples on different water types.*

Modelling of Leaching experiments

Leaching experiments are still ongoing. The modelling of these was performed in a stepwise manner. The exact compositions of the leaching samples were modelled and the resulting solid phases were used as an input values for next leaching step. Selected method enabled comparison between modelled and measured values because the leaching processes in both cases were identical. The modelling and Leaching results can be seen in Figure 18.2.

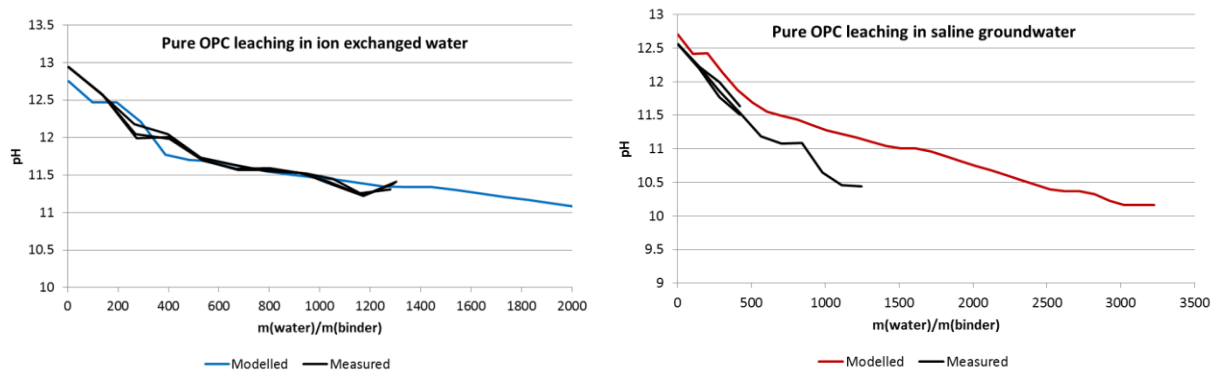

Figure 18.2. *Modelled and measured leaching of pure OPC in ion exchanged water and saline groundwater.*

Equilibrium calculations of leachate bentonite interaction with varying leachate/bentonite ratios

The results from the third modelling exercise were presented in Davos Clay conference. The leachate compositions were results from an experiment between saline groundwater and cementitious materials interaction with varying CaO/SiO_2 -ratios from 3.14 to 0.4 in equilibration. The results from an experiment having groundwater/binder ratio of 1 can be seen in Figure 18.3 and more info about the experiments can be found from (Vehmas et al., 2017).

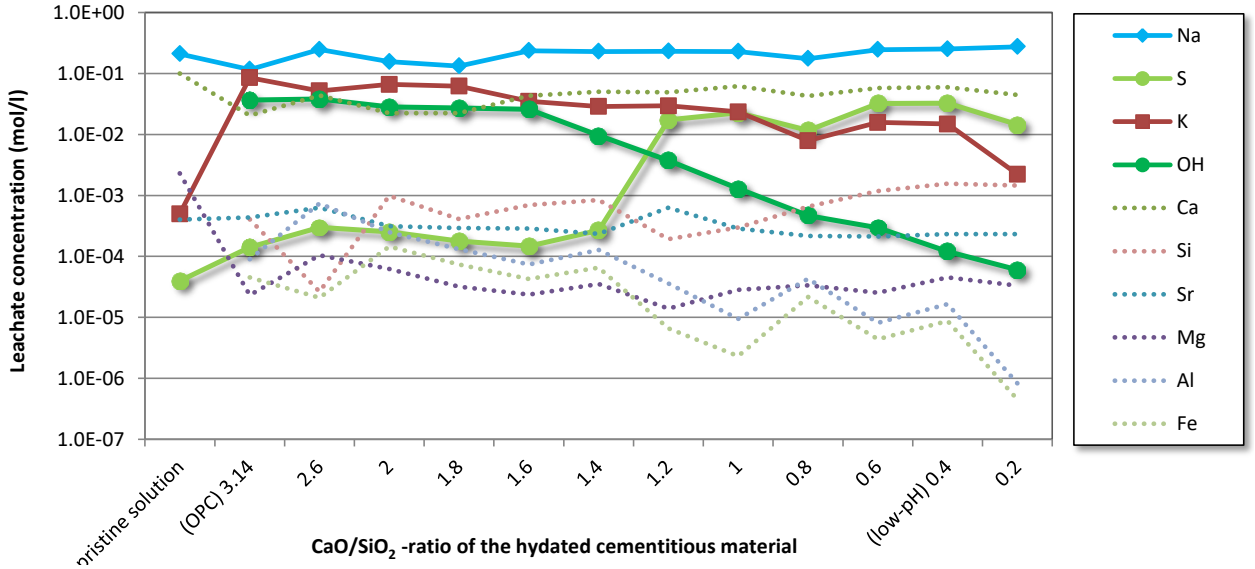

Figure 18.3. *Cementitious materials leachate composition at various CaO/SiO2 –ratios at saline groundwater. Groundwater to binder -ratio of the samples was 1.*

Ca/SiO_2 -ratios 3.14 and 0.4 were chosen as the modelling cases since they present a traditional Portland cement and "low-pH" alternative. The modelling was performed using PHREEQC and Thermoddem database. The model was calibrated using experimental samples to determine the active species and solid components that are relevant to leachate/MX-80 bentonite interaction. The experiments used in the calibration were taken from Heikola et al. (2013). Correlation between calibrated model and experimental samples was good, having correlation R=0.9999. Modelling was performed as equilibrium calculation with 3.14 and 0.4 CaO/SiO_2 -ratios chosen as relevant test cases and mass of leachate/mass of bentonite ratio chosen as variable.

The results are shown in Figure 18.4 and 18.5. The results seem to indicate that the main mechanism of MX-80 bentonite degradation caused by cementitious leachates would not be

dissolution in long-term but the leachates from Portland cement would cause MX-80 to transform to cementitious reaction products, mainly calcium-silicate-hydrates. The transformation was complete as leachate/bentonite -ratio of 500 with pristine Portland cement based leachates. Low pH alternative did not cause major changes in bentonite content but formation of gypsum was observed. The modelling results in low pH and 0.4 -ratio indicate that the leachates interaction would not dissolve the clay based buffer materials but the forming of secondary reaction products will densify the bentonite structure and clog the initial porosity of buffer and backfill material.

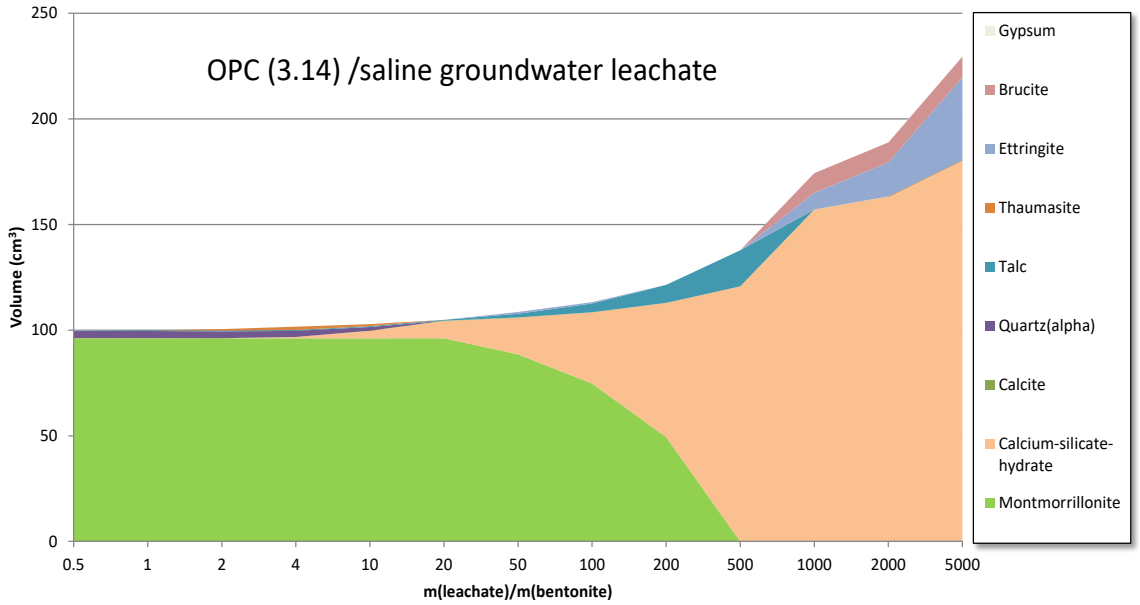

Figure 18.4. *Modelled solid compositions of Portland cement/saline groundwater –leachate and MX-80 bentonite with various leachate/bentonite –ratios.*

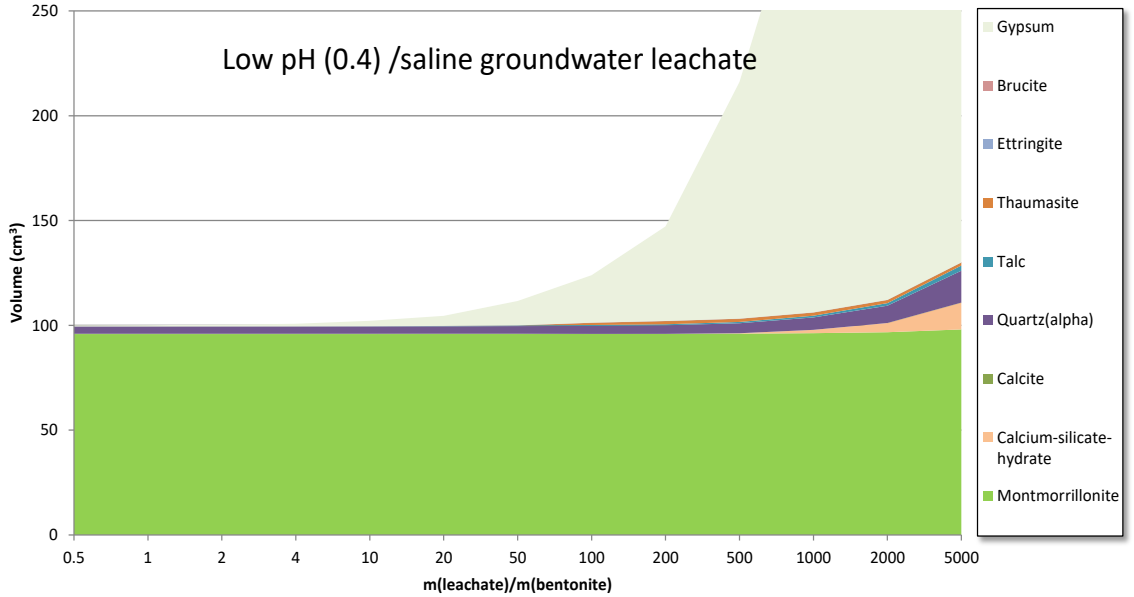

Figure 18.5. *Modelled solid compositions of low–pH cement/saline groundwater –leachate and MX-80 bentonite with various leachate/bentonite –ratios.*

18.4 DISCUSSION

There are unsettled questions regarding to the nature of the CSH gel and reliability of thermodynamic modelling. These questions may not get the final answer in the current project but their effect on the uncertainty of the results can be determined. High C/S –ratio CSH is either in

nanocrystalline form of defect tobermorite or jennite. Although the exact nature of CSH form is not known, both of these forms are in equilibrium with solid portlandite which determines the pH at the high C/S –ratios. C/S –ratios below 0,6, the CSH is either solid solution of tobermorite and silica or low C/S –ratio CSH. The exact nature of CSH at low C/S –ratios in not a necessity to know because the pH of the low C/S –ratio CSH can be experimentally obtained.

There are also uncertainties related to the applicability of thermodynamic modelling. For example, some databases use ion activity products which are poorly applicable or will cause errors to highly concentrated solutions above 0.1 molarity. Thermodynamic modelling should be therefore performed with a conservative approach, so that the amount of modelled hydroxyl ions is always equal or greater than the measured values. According to the first modelled leaching results, the selected modelling method seems to do that naturally. Modelled and measured leaching of pure OPC paste in ion-exchanged water has good correlation. As the water is changed to more saline, the modelled pH values become greater than the measured values. According to first results, the difference originates from precipitating phases. As equilibrium modelling assumes that each phase is in fully equilibrated, the measured values have not reached full equilibrium. This tends to lower the solubility of the phases in modelled leaching and causes higher pH values compared to the measured values. Thus, kinetics should be included in the leaching models and this will be tried to be done later on year 2018.

18.5 REFERENCES

Cau Dit Coumes C., Courtois S., Nectoux D., Leclercq S., Bourbon X. (2006). Formulating a low-alkalinity, high-resistance and low-heat concrete for radioactive waste repositories. Cem. Concr. Res., 36(12), 2152–2163.

Heikola T., Kumpulainen S., Vuorinen U., Kiviranta L., Korkeakoski P., (2013). Influence of alkaline (pH 8.3-12.0) and saline solutions on chemical, mineralogical and physical properties of two different bentonites. Clay Minerals, 48, 309-329.

Holt E., Koho P. (eds.) (2016). DOPAS Deliverable D4.5 POPLU Experimental Summary Report. 170 p. available from http://www.posiva.fi/en/dopas/deliverables.

Holt E., Leivo M., Vehmas T. (2014). Low-pH concrete developed for tunnel end plugs used in nuclear waste containment. In Concrete Innovation Conference (CIC 2014), 11-13 June, Oslo, Norway.

Martino J., Dixon D., Holowick B., Kim C.-S. (2011). Enhanced sealing project (ESP) Seal Construction and Instrumentation. NWMO report.

Savage D. (2007). Low pH Cements, SKI Report 2007:32.

Vehmas T., Leivo M., Holt E., (2017). Comparison of experimental and modelled pore solutions of low-pH Ordinary Portland Cement based mix designs. Proceedings of the 2nd annual Cebama workshop.

Vogt C., Lagerblad B., Wallin K., Baldy F., Johansson J.-E. (2009). Low pH self compacting concrete for deposition tunnel plugs. Swedish Nuclear Fuel and Waste Management Co. SKB report R-09-07.

20 LML/ H. Yang, Z.B. Liu, S.Y. Xie, J.F. Shao

Abstract

In the framework of CEBAMA project, the LML is involved in the experimental investigation and numerical modeling of hydromechanical behavior of interfaces between the COx claystone and low pH concrete, respectively in WP1 and WP3. In this contribution, we present the formulation of the constitutive model and some examples of application to concrete fracture.

Keywords: concrete fracture, normal compression, direct shear, hydromechanical behaviour, constitutive modelling, permeability evolution

20.1 INTRODUCTION

During the last period, we have designed a specific device in order to perform hydrostatic and direct shear tests on an interface in a cylinder sample composed of claystone for the half part and concrete for another half part. We poured an ultra-high-performance concrete onto the planar surface of Callovo-Oxfordian (COx) claystone to make cylindrical specimens for laboratory tests. Our experiment results showed that the ultra-high-performance concrete can adhere well to the COx claystone due to the settlement of concrete binders. A buffer zone was observed around the interface during the curing of concrete. A first series of triaxial direct shear tests have been performed and have demonstrated that the mechanical properties such as the shear strength, shear modulus of the interface were dependent on the normal stress. The optical microscopic scanning results showed that high normal stress contributed to the smoothing of sheared interface morphology. Based on the first experimental data, an elastoplastic model is formulated for the description of hydromechanical behavior of interface subjected to normal stress, shear stress and fluid pressure (Yang et al., 2017).

However, as the experimental tests on interfaces are still ongoing and due to the similarity of behaviour between a fracture and an interface, the calibration and validation of the model has so far performed only on a concrete fracture. The calibration and validation of the model on the claystone-concrete interface will be done during the next period.

In this deliverable, we present the formulation of the constitutive model and some examples of application to concrete fracture (Yang et al., 2017).

20.2 ELASTOPLASTIC MODEL

Interface behavior under normal stress

Under a normal compression stress, the interface exhibits a nonlinear mechanical response. For the sake of simplicity, it is proposed to develop a simple incrementally elastic model for modeling the interface deformation under normal stress by neglecting the irreversible strain during unloading process. Furthermore, when the interface is saturated with a fluid, the variation of fluid pressure should also induce a normal deformation (opening or closure) in the interface. Assuming that the effect of fluid pressure on interface deformation can be described by using the classical Terzaghi's effective stress concept, the following incremental elastic model is proposed:

$$d\sigma_n = \tilde{K}_n(\tilde{V})\,d\tilde{V} - dp \tag{1}$$

σ_n is the normal stress and p is the fluid pressure. V denotes the normal relative displacement of interface (with a negative value denoting a closure of interface) while $\tilde{V} = \frac{V}{b_0}$ the normalized

relative displacement with b_0 being the initial hydraulic aperture of interface. K_n represents the normal stiffness (expressed in MPa/mm) while $\tilde{K}_n = K_n b_0$ is the normal modulus of interface (expressed in MPa). It is obvious that the normal stiffness K_n should be a function of relative normal displacement. Based on the experimental data and according to Bandis and al. (1983), the following relation is proposed:

$$K_n = \frac{K_{ni}}{(1-\Delta V/V_m)^2} \qquad (2)$$

K_{ni} denotes the initial normal stiffness at $\Delta V = 0$ while V_m is the maximum closure of the interface at its complete mechanical closure state.

Elastic-plastic behavior under shear test

One denotes dv as the incremental normal displacement and $d\vec{u}$ the shear displacement vector. Each component of displacement is divided into an elastic part (with superscript e) and plastic part (with superscript p):

$$\begin{cases} dv = dv^e + dv^p \\ d\vec{u} = d\vec{u}^e + d\vec{u}^p \end{cases} \qquad (3)$$

The incremental stress-strain relations can be written as:

$$\begin{cases} d\sigma_n + dp = \tilde{K}_n \left(d\tilde{v} - d\tilde{v}^p \right) \\ d\vec{\tau} = K_t \left(d\vec{\tilde{u}} - d\vec{\tilde{u}}^p \right) \end{cases} \qquad (4)$$

The plastic strains should be determined by defining a plastic yield function and a plastic potential in case of a non-associated flow rule. According to experimental data, plastic strains (irreversible opening or closure and sliding) are induced by shear stress and influenced by effective normal stress defined by $\sigma_n^{eff} = \sigma_n + p$. The rate of plastic strain is dependent not only on the friction angle but also on the inclination angle of asperities of interface surfaces. To this end, a simplified microstructure morphology of rough interface is considered here and illustrated in Figure 20.1. In this figure, θ_0 denotes the initial inclination angle of asperities. Due to shearing process, asperities are progressively destructed. This leads to a reduction of asperity inclination angle to the current value θ. When all asperities are fully damaged, one gets $\theta \to 0$. On the other hand, the shear strength of interface is also affected by the surface roughness which is represented here by a frictional angle ϕ_r. Further, in some situations, interface surfaces may be cemented and this cementation provides the shear strength in unconfined condition ($\sigma_n^{eff} = 0$), which is here described by the cohesion parameter C_0. Considering all these features and making the projection of effective normal stress and shear stress along the inclined interface surface, one adopts here a generalized Mohr-Coulomb criterion as the yield surface function of interface:

$$F = \left(\sigma_n^{eff} \sin\theta + |\vec{\tau}| \cos\theta \right) + \tan(\phi_r) \left(\sigma_n^{eff} \cos\theta - |\vec{\tau}| \sin\theta \right) + C_0 \le 0 \qquad (5)$$

ϕ_r denotes the friction angle and C_0 the cohesion of interface. θ represents the current inclination angle of asperities. Due to the presence of such asperities, the tangential plastic sliding can induce a normal plastic closure or opening. Note that the Mohr-Coulomb criterion adopted for interface is formally equivalent to the widely used Patton criterion. In order to properly the normal plastic deformation induced by shear stress, a non-associated plastic flow rule is necessary. The following plastic potential is proposed:

$$G = \sigma_n^{eff} \sin\theta + |\tau| \cos\theta \qquad (6)$$

The plastic strain rates can be now expressed by the following plastic flow rule:

$$\begin{cases} dv^p = d\lambda \dfrac{\partial G}{\partial \sigma_n^{eff}} \\ d\vec{u}^p = d\lambda \dfrac{\partial G}{\partial |\tau|} \dfrac{\vec{\tau}}{|\tau|} \end{cases} \quad \text{if } F = 0 \text{ and } \dot{F} = 0 \tag{7}$$

Here the plastic multiplier verifies the following loading-unloading condition:

$$d\lambda \geq 0 \, , \, F \leq 0 \, , \, d\lambda F = 0 \tag{8}$$

The plastic multiplier can be determined from the plastic consistency condition such as:

$$d\lambda = \frac{K_n \dfrac{\partial F}{\partial \sigma_n^{eff}} dv + K_t \dfrac{\partial F}{\partial |\tau|} \dfrac{\vec{\tau}}{|\tau|} d\vec{u}}{\dfrac{\partial F}{\partial \sigma_n^{eff}} K_n \dfrac{\partial G}{\partial \sigma_n^{eff}} + \dfrac{\partial F}{\partial |\tau|} K_t \dfrac{\partial G}{\partial |\tau|} - H} \tag{9}$$

The scalar valued function H denotes the plastic hardening modulus which is expressed as a function of the plastic strain energy:

$$H(w_t^p) = \frac{\partial F}{\partial w_t^p} |\tau| \frac{\partial G}{\partial |\tau|} \quad , \quad w_t^p = \int \vec{\tau} \cdot d\vec{u}^p \tag{10}$$

During the plastic sliding process, asperities of interface are progressively destroyed. In order to describe this kind of surface evolution, each asperity is idealized by a saw tooth form. The degradation process is represented by a decrease of its inclination angle with the plastic energy. According to Plesha (1987) the following exponential form is adopted:

$$\theta = \theta_0 \exp\left(-c w_t^p \right) \tag{11}$$

θ_0 denotes the initial value of asperity inclination angle and the parameter c controls the rate of asperity degradation. Moreover, it is assumed that this parameter usually depends on the effective normal stress and the following relation is adopted (Nguyen and Selvadurai, 1998):

$$c = a \left(\frac{\left\langle -\sigma_n^{eff} \right\rangle}{P_{atm}} \right)^b \; ; \; a > 0 \, , \, b > 0 \tag{12}$$

where P_{atm} is the atmospheric pressure. a and b are two model's parameters.

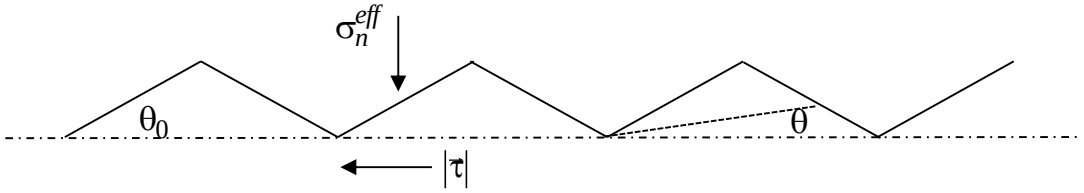

Figure 20.1. *Illustration of the fracture microstructure with initial asperity angle (θ_0) and damaged asperity angle ($\theta \to 0$).*

20.3 VERIFICATION OF MODEL ON CONCRETE FRACTURE

Before the completion of experimental tests on the claystone-concrete interface, the verification of the proposed model is carried out through the simulation of both mechanical tests and fluid flow tests performed on a concrete fracture created from a cylinder sample (Yang et al. 2017).

In Figure 20.2, the stress-displacement curves in shear tests under three different normal stresses are presented. One can see that there is a good agreement between the experimental data and numerical results. In particular, the fracture softening due to asperity damage in the post-peak regime is

correctly reproduced. The normal strain induced by the shear stress remains very small until the peak stress is reached. In the post-peak regime, the asperity damage generates a normal closure during the shear tests.

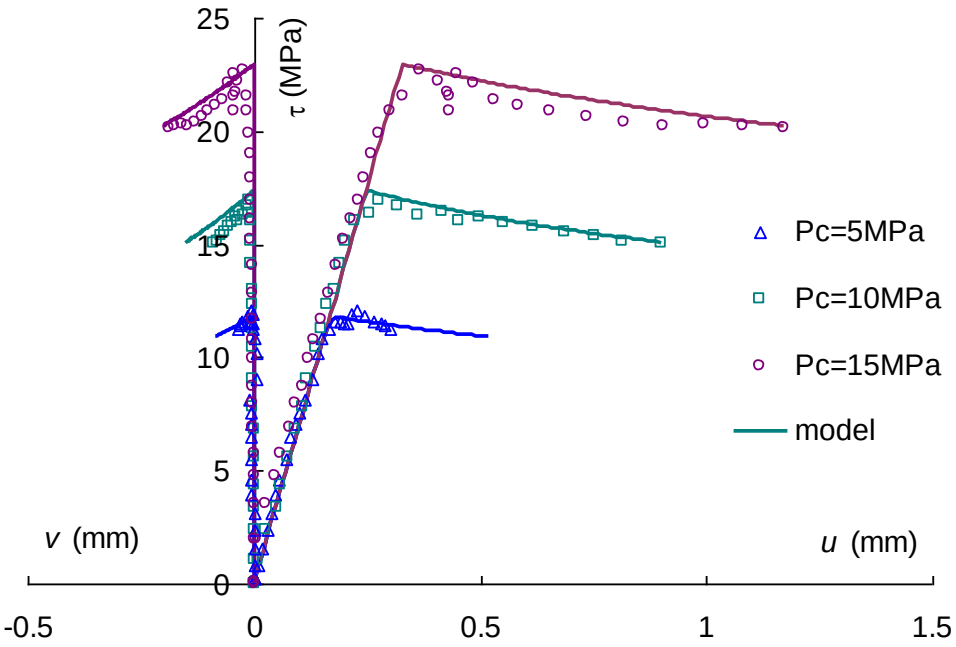

Figure 20.2. *Numerical simulation of direct shear tests with different normal stresses.*

For the study of water flow tests, the fluid pressure distribution is no more uniform along the fracture. Therefore, it is needed to solve a boundary value problem. However, the objective of the present study is to establish the relationship between the pressure gradient and flow rate in the hydraulic flow tests. Some simplifications are retained. It is assumed that the water flow takes place only along the axial direction. Further, one assumes that the permeability of concrete matrix is much smaller than that of the fracture so that the fluid flow occurs entirely through the fracture. Therefore, it consists in solving a one-dimensional flow problem along a planar fracture with varying opening as illustrated in Figure 3. Using the cubic law, the one-dimensional hydraulic diffusion equation along the fracture can be expressed as follows:

$$Q = \frac{We_h^3}{12\mu}\frac{\Delta p}{L} \tag{13}$$

Q denotes the total flow rate through the fracture, μ is the dynamic viscosity of fluid, e_h is the hydraulic aperture. W and L are respectively the width and length of fracture. Δp is the difference of fluid pressure between the injection and outlet points. As the fluid pressure distribution is not uniform along the fracture, the deformation is not uniform and should be correlated with the pressure distribution. However, as there is no shear stress applied to the fracture, no plastic strains occur. Only the normal strain (relative displacement) is coupled with the fluid pressure according to the elastic stress-strain relation (4) with $d\tilde{v}^p = 0$. It is then convenient to express the hydraulic aperture as a function of normal opening or closure so that $e_h = e_h(V)$. The latter can be calculated using the elastic stress-strain relation mentioned above. Due to the nonlinear relation between hydraulic aperture and fluid pressure, it is not easy to establish an analytical solution of diffusion equation. Therefore, a simple finite difference method is here used to obtain a numerical solution. The fracture is divided into N intervals along its length (Figure 20.3), so that at any interval i, the diffusion equation is written as:

$$Q_i = \frac{We_{hi}^3}{12\mu}\frac{\Delta\bar{p}}{\bar{L}} \quad , \quad \Delta\bar{p} = \frac{\Delta p}{N} = \frac{p_{in} - p_{out}}{N} \quad , \quad \bar{L} = \frac{L}{N} \tag{14}$$

Q_i and e_{hi} are respectively the fluid flow rate and hydraulic aperture of the i^{th} fracture interval. Moreover, the empirical relation proposed by Barton et al. (1985) is used here to define the relation between e_{hi} and V_i:

$$e_{hi} = \frac{(b_0 + V_i)^2}{JRC^{2,5}} \tag{15}$$

The fracture roughness coefficient JRC is a morphological parameter which is related to the asperity distribution form of fracture. The average fluid pressure in the i^{th} interval is calculated by $p_i = p_{in} - i\Delta\bar{p}$, which is used in the elastic stress-strain relation (4) to calculate the average normal displacement V_i. The fluid mass balance leads to the continuity equation:

$$Q = Q_i = W\frac{(e_{h1})^3}{12\mu}\frac{\Delta\bar{p}}{\bar{L}} = \ldots = W\frac{(e_{hi})^3}{12\mu}\frac{\Delta\bar{p}}{\bar{L}} \tag{16}$$

The flow rate of the fracture is finally determined as a function of injection fluid pressure by:

$$Q = W\frac{\Delta\bar{p}}{12\mu}\frac{\sum_{k=1}^{N}\left(e_h^k\right)^3}{L} \tag{17}$$

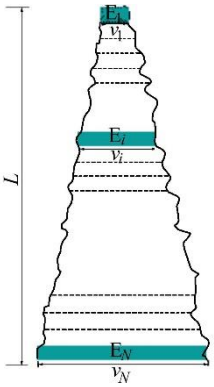

Figure 20.3. *Division of fracture in finite difference calculation.*

In Figure 20.4, the fluid flow rate is presented as a function of injection pressure for three fluid flow tests with different normal stresses. One can see that the numerical results are very close to the experimental data. The flow rate is higher when the normal stress is lower because the normal opening of fracture is lower. There is a strong coupling between fracture normal deformation and fluid flow process.

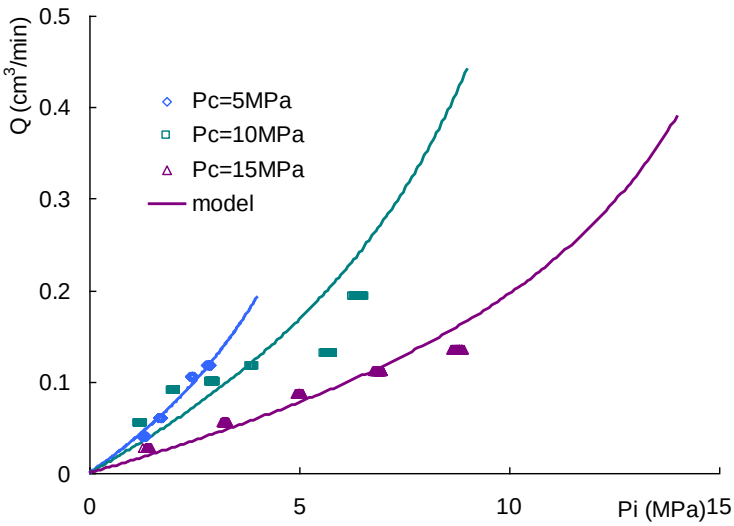

Figure 20.4. *Comparison between numerical results and experimental data for fluid flow rate with injection pressure.*

20.4 CONCLUSIONS

An elastoplastic model has been formulated and so far, applied to concrete fracture. It seems that the proposed model is able to describe the main features of hydromechanical responses of the fracture. Due to the similarity of behaviour between the fracture and interface, the proposed model will be applied to the claystone-concrete interface and it will possibly be improved in order to account for the specific features of the interface. Furthermore, some extensions will also be proposed including chemical degradation of interface.

20.5 REFERENCES

Bandis S., Lumsden A., Barton N. (1983). Fundamentals of rock joint deformation, Int. J. Rock Mechanics and Mining Science, 20, 249-268.

Nguyen T.S., Selvadurai P.S. (1998). A model for coupled mechanical and hydraulic behavior of a rock joint. Int. J. Numer. Anal. Methods Geomech., 22, 29-48.

Plesha M.E. (1987). Constitutive models for rock discontinuities with dilatancy and surface degradation, Int. J. Numer. Anal. Methods. Geomech., 11, 345-362.

Shao J.F., Yang H., Xie S.Y. (2016). Experimental studies of hydromechanical behavior of concrete fractures: a state-of-the art, report to the European Commission, Project CEBAMA, Contract 662147, deliverable D1.03, WP1, Experimental studies - State of the art literature review (M09 - Feb 2016), 113-118.

Yang Y., Xie S.Y., Secq J., Shao J.F. (2017). Experimental study and modeling of hydromechanical behavior of concrete fracture. Water Science and Engineering, 10(2), 97-106.

Acknowledgements:
This study was jointly funded by ANDRA (French National Agency for radioactive waste management) through the grant number 51992 and the European Commission through the project CEBAMA (grant number 662147).

24 PSI/ G. Kosakowski

24.1 INTRODUCTION

Modelling work related to WP1/2 concentrated on the thermodynamic modelling of the hydration of the CEBAMA reference mix, as input for a planned WP3 benchmarking study on cement/clay. This planned WP3 benchmarking study will compare modelling approaches and numerical models by calculation of the long-term evolution of a low pH concrete/clay rock interface. As the clay rock, the Callovo-Oxfordian claystone is considered, while the CEBAMA reference mix is considered as low-pH concrete (Holt et al., 2016; Vehmas et al., 2016).

As preparation for the benchmark, calculations on the initial state of the materials had to be conducted. It was agreed to use the same setup as in Marty et al. (2015) for the Callovo-Oxfordian claystone. For the CEBAMA reference mix, no modelling study existed and detailed experimental data on the long-term hydration of the concrete will be not available before end of the project. Amphos 21 and PSI therefore conducted a modelling study on the hydration of the reference mix. While Amphos modelled the system based on the Thermochimie thermodynamic database with Phreeqc, we used the scripting engine of GEM-Selektor V3 and the CEMDATA thermodynamic database.

24.2 HYDRATION MODELLING OF THE CEBAMA REFERENCE MIX

Thermodynamic setup

Our thermodynamic setup is based on the PSI/Nagra TDB (https://www.psi.ch/les/database) in combination with CEMDATA 14 (https://www.empa.ch/web/s308/cemdata). For compatibility reasons, not all available mineral phases were included in the study. Clay and zeolite phases were generally removed from the setup to allow comparison with the Phreeqc results. For C-S-H the quaternary solid solution model CSHQ of Kulik (2011) was used. Alkali uptake for Na and K was modelled as an ideal solid solution (Ca-, K-, Na-endmembers) mimicking the cation exchanger approach of Phreeqc. Relative stabilities of the endmembers were calculated based on the log(k) values given in Idiart et al. (2017). The cation exchanger capacity was linked to the CSHQ phase by scaling the exchanger amount to the silica content of the CSHQ phase with additional conversion factors for tobermorite and jennite endmembers given in Idiart et al. (2017).

Dissolution/precipitation of several phases is kinetically controlled. The hydration kinetics of clinker phases follows the approach of Parrot and Killoh (1984) with the parameters used by Lothenbach (2011). The initial amount for clinker phases was taken from SKB (2014). All other cement constituents, mainly alkali hydroxides and sulphates (gypsum), were not kinetically controlled and therefore assumed to be immediately dissolved or reacted.

The dissolution of the quartz phase (which represents the quartz filler), silica fume and blast furnace slag are controlled with the pH dependent approach for quartz dissolution of Palandri and Kharaka (2004) with the values from Idiart et al. (2017). All three phases react based on the same kinetic parameters, but scaled by different reactive surface areas which were calculated based on average particle sizes.

Composition of reference mix

The modelling approaches of PSI and Amphos 21 are based on the same reference mix composition (Table 1). The detailed composition of cement, silica fume and blast furnace slag is listed in Idiart et al. (2017). Table 2 gives the simplified composition used for the PSI modelling study. Some

ingredients are combined in an inert component which does not participate in any reaction. The inert material has the density of quartz and is included in the volume and mass balance.

The main difference to the setup of Idiart et al. (2017) is the interpretation of Cl content of CEM I in SKB (2014). With the GEM method, it is not possible to equilibrate a system with an independent component set to a zero amount, therefore and as a conservative estimate the Cl content of the CEM I mix was set equal to the limit of detection given in SKB (2014) as "<0.1 wt%".

Table 24.2. *Mix design for CEBAMA reference mix (Vehmas et al., 2016; Idiart et al., 2016).*

Composition of reference mix	**Concrete (g/1000 cm^3)**	**Remarks**
CEM I	105	Composition see Table 2
Silica fume	110	Composition see Table 2
Blast furnace slag	65	Composition see Table 2
Quartz filler	116	SiO_2
Aggregate 0-1 mm	168	Inert phase (same properties as quartz)
Aggregate 1-8 mm	770	Inert phase (same properties as quartz)
Aggregate 8-16 mm	532	Inert phase (same properties as quartz)
Aggregate 16-32 mm	396	Inert phase (same properties as quartz)
Water	120	H_2O
Superplasticizer	16.8	Not considered in modelling study

24.3 RESULTS

The ingredients of the cement were added in the amounts given in Table 2. Initially, for time t = 0 the system was equilibrated without allowing to react clinker phases, quartz filler, blast furnace slag and silica fume. The nominal amounts of unreacted clinker from SKB (2014) had to be scaled with a factor 0.95, as otherwise the GEM algorithm would not converge. This resulted in a system with an initial volume of 971 ccm which is relatively close to the volume of 1000 ccm given in the recipe. The initial volumetric water content (porosity) is 0.121.

The results of the transient equilibration procedure are summarized in terms of temporal mineral phase evolution in Figure 1. Clinker phases are quickly consumed and hydrated cement phases are formed. These reactions consumed about half of the initial water. In addition, the blast furnace slag and part of the silica fume are consumed within the first year and mainly contribute to the formation of silica rich C-S-H. After about 1 month simulation time the phase assemblage stabilizes and C-S-H, hydrotalcite, ettringite and strätlingite remain as stable phases. The iron bearing phase is ferrihydrate. The pH in the system remains high (>12.5) for a few days. After dissolution of portlandite is complete, pH is linked to the C-S-H composition. Due to the dissolution of blast furnace slag and silica fume C-S-H with high silica to calcium ratio is formed and pH is decreasing with time. After about 1 year the evolution of the systems reaches a semi steady state, as the C-S-H composition stabilizes and pH approaches a value of 10.4 (Figure 2). Due to the pH dependent dissolution kinetics silica fume, quartz filler and potentially also aggregates react with strongly reduced rates. It should be noted that at this pH zeolite formation

is possible (Lothenbach et al., 2017). The pH is somewhat lower than for the calculations of Idiart et al. (2017). One reason is the addition of 0.1 wt% of Cl to the cement which counterbalances the influence of alkali in the pore water. Removing the Cl from the system will result in 0.2 units higher pH values after 1 year.

Table 24.3. *Definition of composition for reference mix ingredients in terms of independent components for modelling with GEM-Selektor V3.*

Composition in oxides	**Amount [g]**	**Composition in independent components**	**Mol amount for 100 g**
CEM I 42.5 MH/SR/LA			
CaO	64	Al	0.0687
SiO_2	21	C	0.0090
Al_2O_3	3.5	Ca	1.1503
Fe_2O_3	4.6	Cl	0.0028
MgO	0.7	Fe	0.0576
Na_2O	0.07	Inrt	0.0384
SO_3	2.2	K	0.0132
Cl	0.1	Mg	0.0174
$CaCO_3$	0.9	Na	0.0023
Inert materials	2.31	O	2.1642
K_2O	0.62	S	0.0275
Total amount	100	Si	0.3495
Blast furnace slag (Mol amount given for 99.27 g)			
CaO	41.5	Al	0.2079
SiO_2	32.8	Ca	0.7400
Al_2O_3	10.6	Fe	0.0101
Inert materials	2.63	Inrt	0.0438
Fe_2O_3	0.81	K	0.0132
MgO	8.29	Mg	0.2057
K2O	0.62	Na	0.0200
SO_3	1.4	O	2.4337
Na_2O	0.62	S	0.0175
Total amount	99.27	Si	0.5459
Silica fume			
CaO	1.46	Al	0.0282
SiO_2	93.1	Ca	0.0260
Al_2O_3	1.44	Fe	0.0114
Inert materials	0.01	Inrt	0.0002
Fe_2O_3	0.91	K	0.0368
MgO	0.88	Mg	0.0218
K_2O	1.73	O	3.2423
SO_3	0.47	S	0.0059
Total amount	100	Si	1.5495

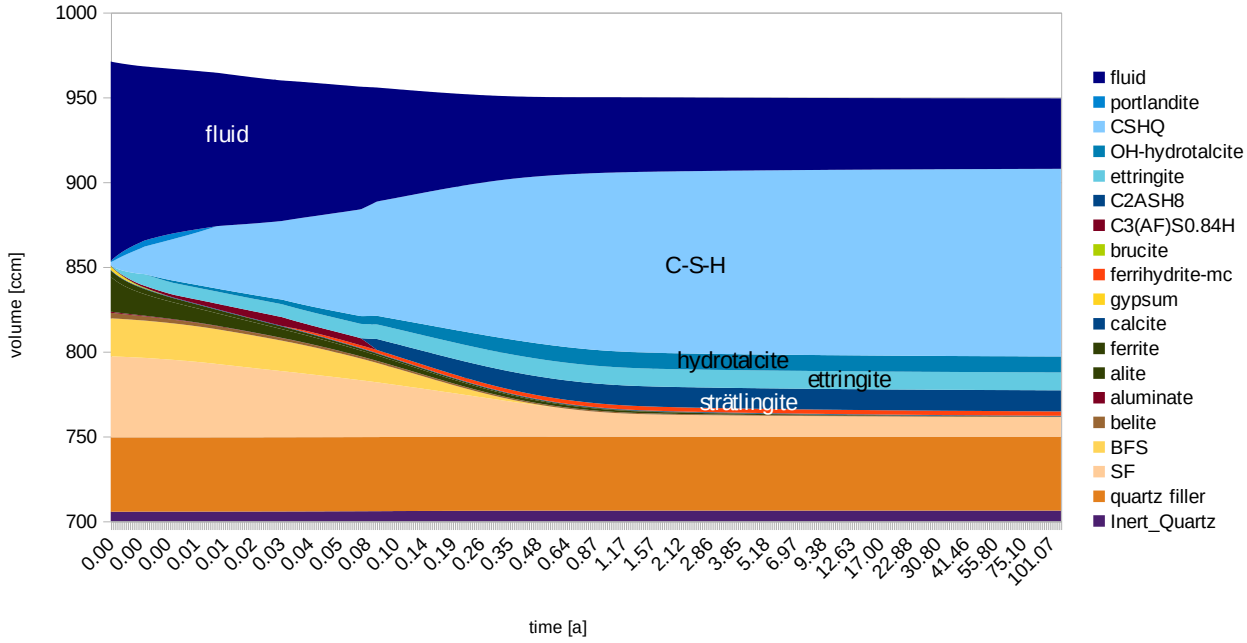

Figure 24.1. *Modelled temporal evolution of phase volumes during hydration of reference mix.*

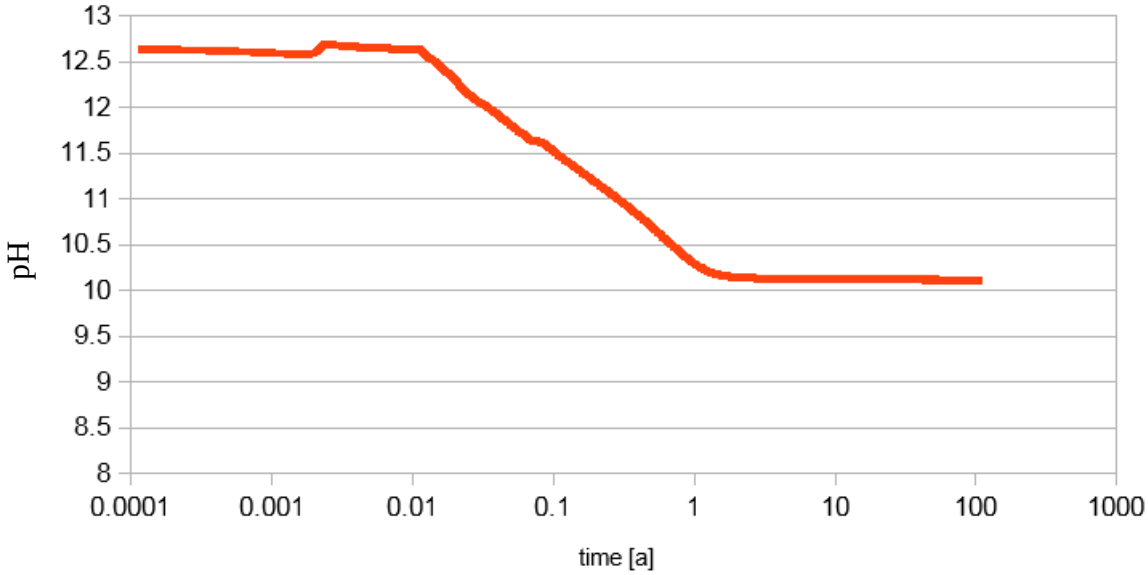

Figure 24.2. *Modelled temporal evolution of pH with time (years).*

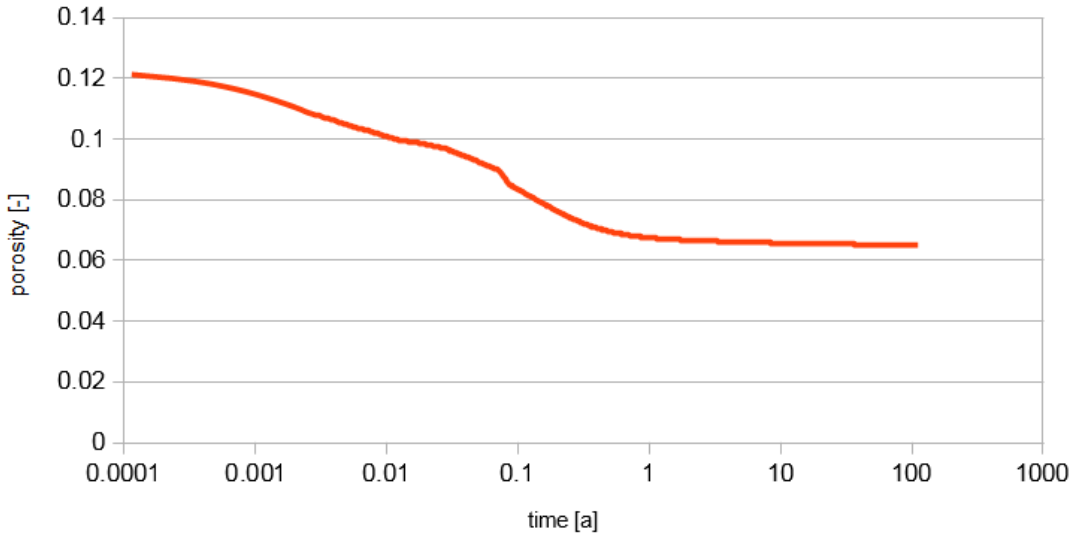

Figure 24.3. *Modelled temporal evolution of porosity (-) with time (years).*

The evolution of porosity with time is shown in Figure 24.3. The initial porosity of 0.121 drops to 0.068 after 1 year. It further changes slowly to 0.065 after 100 years due to the conversion of SiO_2 from silica fume and quartz filler to silica rich C-S-H.

Pore water compositions at different times in terms of total elemental concentrations are given in Table 24.3. Generally, the values are comparable to those calculated by Idiart et al. (2017). Differences in concentrations can be explained by differences in the stability of controlling phases in the thermodynamic data bases and the different approaches for modelling C-S-H. A major difference can be found in the redox of the system. In the calculations of Idiart et al. (2017) reducing conditions are set by the stability of magnetite/ferrihydrate. With GEMS-Selektor redox is calculated based on the total mass and charge balance. Our calculations result in strongly oxidizing conditions. In general, the exact representation of the real redox of the concrete system is not aim of this modelling exercise. This would require a much more complex system setup specific for modelling the redox.

Table 24.4. *Total elemental concentrations (mol/kg) in concrete pore water after different times.*

Element	**10 days**	**100 days**	**1 year**	**10 years**	**100 years**
Al	2.18E-05	1.16E-04	1.45E-04	1.54E-04	1.53E-04
C	9.47E-06	8.20E-06	8.27E-06	8.44E-06	8.40E-06
Ca	5.92E-03	1.05E-02	1.83E-02	2.23E-02	2.29E-02
Cl	3.60E-02	5.97E-02	7.00E-02	7.38E-02	7.54E-02
Fe	3.61E-08	3.45E-09	6.73E-10	4.61E-10	4.56E-10
K	2.89E-02	2.79E-02	3.24E-02	3.44E-02	3.48E-02
Mg	1.44E-08	1.11E-07	1.31E-06	2.52E-06	2.60E-06
Na	1.26E-02	1.58E-02	1.76E-02	1.84E-02	1.85E-02
S	3.61E-04	1.46E-03	7.76E-03	1.13E-02	1.13E-02
Si	1.32E-04	3.73E-04	6.29E-04	7.38E-04	7.37E-04

24.4 SUMMARY

We conducted a modelling study on the hydration of the CEBAMA reference mix. The study was part of the setup definition for the WP3 modelling task and calculated the initial state of the

hydrated reference mix based on an alternative thermodynamic set of data. The study helps to identify sensitivities related to the use of different thermodynamic data and allows to find a unified conceptual setup that can be calculated by all participating modelling teams.

The agreement between our calculations and the ones of Idiart et al. (2017) is excellent in terms of temporal evolution of the system. Phase assemblage, porosity values and pH also agree well in a quantitative way. The pore water composition shows some differences which can be related to the differences in (cement) phase stability between the utilized thermodynamic data bases and the use of different modelling approaches for C-S-H phase.

24.5 REFERENCES

Holt E., Claret F., Mäder U. (2016). Report on WP1 selected experimental materials to be used, including both new laboratory and aged in-situ samples. CEBAMA Report Deliverable D1.05.

Idiart A. Coene E., Laviña M. (2017). Detailed description and Setup of the Modelling Task. CEBAMA Report.

Kulik D.A. (2011). Improving the structural consistency of C-S-H solid solution thermodynamic models. Cement and Concrete Research, 41(5), 477–495.

Lothenbach, B. (2011). CI Experiment: Thermodynamic modelling of the hydration of ordinary Portland cement and low-pH cements. Technical note TN 2009-33. Dübendorf, Switzerland: Empa.

Lothenbach, B., Bernard, E., Mäder, U. (2017). Zeolite formation in the presence of cement hydrates and albite. Physics and Chemistry of the Earth, Parts A/B/C, 99, 77–94.

Parrot, L. J., Killoh, D. C. (1984). Prediction of Cement Hydration. British Ceramic Proceedings, 35, 41–51.

SKB (2014). Initial state report for the safety assessment SR-PSU. Technical Report SKB TR-14-02, Svensk Kärnbränslehantering AB.

Vehmas, T., Schnidler, A., Löija, M., Leivo, M., Holt, E. (2016). Reference mix design and castings for low-pH concrete for nuclear waste repositories. In Proc. 1st Annual Workshop CEBAMA, Barcelona, Spain, May 2016.